LEVERAGING A DEPTH-AVERAGED MODEL OF TURBIDITY CURRENTS TO DEVELOP A DIMENSIONLESS FRAMEWORK FOR PREDICTING SUBMARINE FAN MORPHOLOGY AND STRATIGRAPHIC ARCHITECTURE

AN ABSTRACT

SUBMITTED ON THE SIXTH OF OCTOBER 2023

TO THE DEPARTMENT OF EARTH AND ENVIRONMENTAL SCIENCES

IN PARTIAL FULLFILMENT OF THE REQUIREMENTS

OF THE SCHOOL OF SCIENCE AND ENGINEERING

OF TULANE UNIVERSITY

FOR THE DEGREE

OF

DOCTOR OF PHILOSOPHY

BY

____

Abdul Wahab

APPROVED: ________________________

Kyle M. Straub, PhD
Director

____

David C. Hoyal, PhD

____

Mrugesh Shringarpure, PhD

____

Nicole M. Gasparini, PhD

____

TorBjörn Törnqvist, PhD

ABSTRACT

Submarine fans are crafted by turbidity currents in deep water on continental slopes and abyssal plains. Turbidity currents are gravity flows that move downslope due to their excess density relative to ambient water from dilute suspension of sediments. Submarine fan morphology and their strata are complex and have motivated the development of classification schemes by stratigraphers. Prior classification schemes lack predictive capability because they do not establish a process-based link with turbidity currents. In this dissertation, I establish this link by leveraging a depth-average numerical model for turbidity currents that conserves fluids, sediments, momentum, and kinetic energy, in addition to modeling bedload transport and substrate cohesion. In the first chapter, I propose a classification scheme for fan morphology based on dimensionless parameters that describe the fluid and sediment transport fields. I quantify this by measuring rugosity as a proxy for morphological complexity. In the second chapter, I generated synthetic seismic surveys for select models and compared them to shallow seismic surveys of three modern submarine fans. Models are forced with turbidity currents with comparable flow parameters. I show similar stratigraphic organization between the model and modern examples of submarine fans. In the third chapter, I investigated conditions necessary for initiation, maintenance, and termination of submarine channels. I show that while erosion alone is sufficient to initiate channels, bedload transport is the most important parameter for channel maintenance. Further, the length of channelization in the distributary networks and the number of channel bifurcations increases as the densimetric Froude and Rouse numbers decrease. Results in this dissertation advances stratigraphic predictions from *a priori* knowledge of boundary conditions and the inversion of paleo-hydraulics from preserved deep-water stratigraphy.

LEVERAGING A DEPTH-AVERAGED MODEL OF TURBIDITY CURRENTS TO DEVELOP A DIMENSIONLESS FRAMEWORK FOR PREDICTING SUBMARINE FAN MORPHOLOGY AND STRATIGRAPHIC ARCHITECTURE

A DISSERTATION

SUBMITTED ON THE SIXTH OF OCTOBER 2023

TO THE DEPARTMENT OF EARTH AND ENVIRONMENTAL SCIENCES

IN PARTIAL FULLFILMENT OF THE REQUIREMENTS

OF THE SCHOOL OF SCIENCE AND ENGINEERING

OF TULANE UNIVERSITY

FOR THE DEGREE

OF

DOCTOR OF PHILOSOPHY

BY

____

Abdul Wahab

APPROVED: ____________________

Kyle M. Straub, PhD
Director

____

David C. Hoyal, PhD

____

Mrugesh Shringarpure, PhD

____

Nicole M. Gasparini, PhD

____

TorBjörn Törnqvist, PhD

ACKNOWLEDGEMENTS

I express my heartfelt gratitude to my Ph.D. advisor, Dr. Kyle M. Straub for accepting me as a graduate student in the Tulane Sediments Dynamics and Stratigraphy research group. I first met Dr. Straub during the annual Geological Society of America gathering in 2016. I am forever grateful to you for teaching me siliciclastic sediment-transport, treating me with kindness and respect, and encouraging me to form my own research ideas and external collaborations. Your dedicated and effective mentorship led me from being a novice in research on turbidity currents and submarine fans to having the opportunity to publish on this problem in Nature Communications. The time we spent crafting that manuscript was the highlight of time as a PhD student!

I would also like to take this opportunity to thank my thesis committee members. I am grateful to Dr. David C. Hoyal for conceiving the big picture idea for my Ph.D. research project, facilitating training and computational tools needed to undertake this study, and vetting the scientific integrity of all manuscripts/documents over the duration of my Ph.D. degree. I am very thankful to the effective mentorship and guidance of Dr. Mrugesh Shringarpure. In his mentorship, I learned how to run a complex computational model, understand the fundamentals of Computational Fluid Dynamics, and develop coding abilities to analyze the numerical data. I am also thankful to the continued support and encouragement I have received from Dr. Nicole Gasparini and Dr. Torbjorn Tornqvist in stressful times during my Ph.D. program.

I am thankful to ExxonMobil for funding my Ph.D. research. ExxonMobil provided access to their model (EMstrata), high performance computing, and provided technical training necessary for the success of my Ph.D. project. Without their financial and technical support, this project would not have been possible.

I would also like to thank the graduate students and staff at Tulane Earth and Environmental Sciences at Tulane University for providing a safe and a scientific atmosphere. I found engagements with fellow graduate students quite fruitful throughout my Ph.D. program. I want to specifically thank Tonya Durden whom’ s administrative support made my life easier at Tulane University. Graduate students cannot thank you enough for what you do for them.

I want to present my sincerest gratitude to the United State Education Foundation and the Fulbright program for bringing me to United States of America. I am grateful for that first trip to Grand Valley State University in Michigan, which set my path for higher education in United States of America.

Finally, I am eternally grateful to my parents Gul Nawab and Gul Ghotai for their continuous support and unwavering faith in me. Thank you for encouraging me to travel far from home in the pursuit of knowledge. I know this distance and separation has never been easy on you, yet you never withdrew your unconditional support and encouragement. It is this unconditional love and support from you both that has helped me come this far. I dedicate my Ph.D. degree and this dissertation to you both!

TABLE OF CONTENTS

LIST OF TABLES

CHAPTER 1

CHPATER 3

LIST OF FIGURES

CHAPTER 1

INTRODUCTION

Submarine fans are terminal sinks in sediment routing systems and are formed on continental slopes and abyssal plains in deepwater settings. They are predominantly crafted by a type of sediment gravity flow called turbidity currents, which arguably move more sediment than any other transport process and their deposits preserve the thickest sediment accumulations on Earth (Talling et al., 2015). These fans can vary in size from 10's to 1000's of km in the world's oceans. Submarine fans and the seascapes they produce have been studied for nearly a century (Kuenen and Migliotini, 1950; Bouma 1962; Normark 1970; Vail 1987; Mutti 1992; Hodgson et al., 2011; Hessler and Fildani, 2019; Wahab et al., 2022), as they host some of the world's largest geofluid reservoirs (Weimer and Pettingill, 2007). The stratigraphy preserved in submarine fans are of particular interest to climate scientists as their deposits hold clues to Earth's past episodes of climate change (Covault et al., 2010; Hessler and Fildani, 2019). Furthermore, the flows that construct these fans impact global climate change through the transport and storage of organic carbon (Galy et al., 2007; Hage et al., 2022). Researchers from outside the geoscience community study flows that form submarine fans to quantify the frequency and severity of geohazards that threaten subsea infrastructure, such as the vast network of seafloor cables that hosts the majority of the global data traffic (Heezen and Ewing, 1952; Carter et al., 2014; Stevenson et al., 2018). Recently, the importance of fan forming flows to subsea ecosystems, including threats to biodiversity from microplastics transported to deep sea communities, have also been identified (Kane et al., 2020; Pohl et al., 2020).

The stratigraphy of submarine fans is complex and differences in fan strata between basins have motivated geoscientists to propose several classification schemes and depositional models (Kuenen and Migliorini, 1950; Bouma 1962, Normark 1970; Mutti and Ricci, 1978; Vail 1991; Clark et al., 1992; Richards et al., 1998; Stow and Mayal, 2000; Posamentier and Walker, 2006; Shanmugam 2016). These models and classifications helped advance our understanding of submarine fan deposits in several basins, but they lack predictive capability and carry significant uncertainty from one basin fan example to another. This is because the aforementioned efforts did not establish a link between submarine fans and their deposits to the fluid and sediment transport physics of the turbidity currents that are responsible for crafting them.

Turbidity currents are dilute sediment gravity flows that move downslope due to their excess density relative to ambient lake or sea water from suspension of sediments (Bagnold 1962) and can travel up to 1000's of km on the ocean floor (Tailing et al., 2022). The depth at which turbidity currents traverse makes their direct monitoring challenging and measurements we do have sample a relatively limited scope and duration of possible field scale flow conditions (Azpiroz-Zabala et al., 2017; Hughes Clarke 2016; Simmons et al., 2020; Pope et al., 2022). Physical laboratory experiments have provided insight into interactions of turbidity currents with an antecedent bed topography (Imran et al., 2002; Parsons et al., 2002; Straub and Mohrig, 2008) over short timescales, but we still lack experimental methods that can produce self-formed channels by fully turbulent flows, and which display sufficient mobility to form a fully dynamic fan surface (De Leeuw et al., 2016; Ferguson et al., 2020).

In this thesis I propose methods to predict the shape and stratigraphic architecture of submarine fans. I overcome the direct observational and experimental limitations by leveraging a process based forward numerical model for turbidity currents called EMstrata (Halsey et al., 2017). The model is based on the depth-average approximation of flow parameters in 3D Navier-Stokes equations of fully turbulent flows (Parker et al., 1986; Imran et al., 1998; Pratson et al., 2001; Traer et al., 2018). In addition, the model solves for bedload fluxes (Peter and Müller, 1948), erosion rates (Garcia and Parker, 1991), deposition rates (Garcia 1994), flocculation of clay particles (Kuprenas et al., 2018, Winterwerp 1998), and the influence of cohesion on the underlying deposits (Winterwerp and Kesteren, 2004).

In the first chapter, I develop a unifying framework to predict submarine fan morphology by simplifying critical environmental forcings, like regional slopes and sediment properties, through a dimensionless framework defined by the densimetric Froude number (ratio of inertial to gravitational forces) and Rouse number (ratio of settling velocity of sediments to shear velocity) of turbidity currents. I explore this framework by leveraging EMStrata and measure fan rugosity as a proxy for their morphological complexity. I show a systematic increase in rugosity by either increasing the densimetric Froude number or decreasing the Rouse number of the simulated flows. These changes reflect observed gradients in the dynamics of channel migration and help discriminate submarine fans that have the potential to impact global climate through sequestration of organic carbon.

In the second chapter, I compare seismic surveys of three modern seafloor fan examples to end-member numerical experiments that are forced with similar forcing conditions. I used outputs of the numerical experiments, such as clay volumes and compacted porosities, to generate elastic responses such as Vp, Vs, and ρ, followed by a 1D wavelet convolution to generate high-resolution synthetic seismic surveys for comparison of stratigraphic architecture to their modern field counterparts through seismic facies analyses. I establish stratigraphic similarity between model-field examples and propose generalized and process-informed depositional models for endmember submarine fans. Results from this work aid subsurface stratigraphic architecture predictions and the interpretation of paleo-environmental conditions from low resolution seismic data of ancient fan deposits.

In the third and final chapter, I explore conditions that are necessary for inception, maintenance, and termination of submarine channels. These channels are a key component of submarine fan morphology and preserved channel bodies help define their stratigraphic architecture. Modern observations of seafloor bathymetry, seismic data, and outcrop images point to an array of submarine channel shapes including meandering, distributive, and low sinuosity channels. We test two hypotheses, 1) Froude and Rouse numbers of turbidity currents set conditions necessary for the inception of self-formed submarine channels, and 2) Parameters such as, grain size distributions, bedload transport, and influence of cohesive sediments, set thresholds for erosion and sedimentation within submarine channels that influence their mobility during fan formation. We quantify emergent channel behavior including their average total length and hierarchy of branching on the fan surface using a novel supervised machine learning approach. Results from this work will aid stratigraphic predictions from *a priori* knowledge of boundary conditions and the inversion of paleo-hydraulics from preserved deep-water stratigraphy, which will aid the reconstruction of environmental signals.

References cited

Azpiroz-Zabala, M., Cartigny, M. J., Talling, P. J., Parsons, D. R., Sumner, E. J., Clare, M. A., ... & Pope, E. L. (2017). Newly recognized turbidity current structure can explain prolonged flushing of submarine canyons. *Science advances*, *3*(10), e1700200.

Bouma, A. H. (1962). Sedimentology of some flysch deposits. *Agraphic approach to facies interpretation*, *168*.

Carter, L., Gavey, R., Talling, P. J., & Liu, J. T. (2014). Insights into submarine geohazards from breaks in subsea telecommunication cables. *Oceanography*, *27*(2), 58-67.

Clark, J. D., Kenyon, N. H., & Pickering, K. T. (1992). Quantitative analysis of the geometry of submarine channels: implications for the classification of submarine fans. *Geology*, *20*(7), 633-636.

Covault, J. A., & Graham, S. A. (2010). Submarine fans at all sea-level stands: Tectono-morphologic and climatic controls on terrigenous sediment delivery to the deep sea. *Geology*, *38*(10), 939-942.

De Leeuw, J., Eggenhuisen, J. T., & Cartigny, M. J. (2016). Morphodynamics of submarine channel inception revealed by new experimental approach. *Nature communications*, *7*(1), 10886.

Ferguson, R. A., Kane, I. A., Eggenhuisen, J. T., Pohl, F., Tilston, M., Spychala, Y. T., & Brunt, R. L. (2020). Entangled external and internal controls on submarine fan evolution: an experimental perspective. *The Depositional Record*, *6*(3), 605-624.

Galy, V., France-Lanord, C., Beyssac, O., Faure, P., Kudrass, H., & Palhol, F. (2007). Efficient organic carbon burial in the Bengal fan sustained by the Himalayan erosional system. *Nature*, *450*(7168), 407-410.

Garcia, M. H. (1994). Depositional turbidity currents laden with poorly sorted sediment. *Journal of hydraulic engineering*, *120*(11), 1240-1263.

Garcia, M., & Parker, G. (1991). Entrainment of bed sediment into suspension. *Journal of Hydraulic Engineering*, *117*(4), 414-435.

Hage, S., Galy, V. V., Cartigny, M. J. B., Heerema, C., Heijnen, M. S., Acikalin, S., ... & Talling, P. J. (2022). Turbidity currents can dictate organic carbon fluxes across river-fed fjords: An example from Bute Inlet (BC, Canada). *Journal of Geophysical Research: Biogeosciences*, *127*(6), e2022JG006824.

Halsey, T. C., Kumar, A., & Perillo, M. M. (2017). Sedimentological regimes for turbidity currents: Depth-averaged theory. *Journal of GEOPHYSICAL research: Oceans*, *122*(7), 5260-5285.

Heezen, B. C., & Ewing, W. M. (1952). Turbidity currents and submarine slumps, and the 1929 Grand Banks [Newfoundland] earthquake. *American journal of Science*, *250*(12), 849-873.

Hessler, A. M., & Fildani, A. (2019). Deep-sea fans: Tapping into Earth's changing landscapes. *Journal of Sedimentary Research*, *89*(11), 1171-1179.

Hughes Clarke, J. E. (2016). First wide-angle view of channelized turbidity currents links migrating cyclic steps to flow characteristics. *Nature communications*, *7*(1), 11896.

Imran, J., Parker, G., & Harff, P. (2002). Experiments on incipient channelization of submarine fans. *Journal of Hydraulic Research*, *40*(1), 21-32.

Imran, J., Parker, G., & Katopodes, N. (1998). A numerical model of channel inception on submarine fans. *Journal of Geophysical Research: Oceans*, *103*(C1), 1219-1238.

Kane, I. A., Clare, M. A., Miramontes, E., Wogelius, R., Rothwell, J. J., Garreau, P., & Pohl, F. (2020). Seafloor microplastic hotspots controlled by deep-sea circulation. Science, 368(6495), 1140-1145.

Kuenen, P. H., & Migliorini, C. I. (1950). Turbidity currents as a cause of graded bedding. *The Journal of Geology*, *58*(2), 91-127.

Kuprenas, R., Tran, D., & Strom, K. (2018). A shear-limited flocculation model for dynamically predicting average floc size. *Journal of Geophysical Research: Oceans*, *123*(9), 6736-6752.

Meyer-Peter, E., & Müller, R. (1948). Formulas for bed-load transport. In IAHSR 2nd meeting, Stockholm, appendix 2. IAHR.Aki, K. and Richards, P.G, 2002, Quantitative Seismology, University Science Books,

Mutti, E. (1992). Turbidite sandstones: AGIP. *Istituto di geologia, Università di Parma, Italy, Special Publication*.

Mutti, E., & Ricci Lucchi, F. (1978). Turbidites of the northern Apennines: introduction to facies analysis. *International geology review*, *20*(2), 125-166.

Normark, W. R. (1970). Growth patterns of deep-sea fans. *AAPG bulletin*, *54*(11), 2170-2195.

Parker, G., Fukushima, Y., & Pantin, H. M. (1986). Self-accelerating turbidity currents. *Journal of Fluid Mechanics*, *171*, 145-181.

Parsons, J. D., Schweller, W. J., Stelting, C. W., Southard, J. B., Lyons, W. J., & Grotzinger, J. P. (2002). A preliminary experimental study of turbidite fan deposits. *Journal of Sedimentary Research*, *72*(5), 619-628.

Pirmez, C., & Imran, J. (2003). Reconstruction of turbidity currents in Amazon Channel. *Marine and petroleum geology*, *20*(6-8), 823-849.

Pohl, F., Eggenhuisen, J. T., Kane, I. A., & Clare, M. A. (2020). Transport and burial of microplastics in deep-marine sediments by turbidity currents. Environmental science & technology, 54(7), 4180-4189.

Pope, E. L., Cartigny, M. J., Clare, M. A., Talling, P. J., Lintern, D. G., Vellinga, A., ... & Vendettuoli, D. (2022). First source-to-sink monitoring shows dense head controls sediment flux and runout in turbidity currents. Science Advances, 8(20), eabj3220.

Posamentier, H. W., & Walker, R. G. (2006). Deep-water turbidites and submarine fans.

Pratson, L. F., Imran, J., Hutton, E. W., Parker, G., & Syvitski, J. P. (2001). BANG1D:: a one-dimensional, Lagrangian model of subaqueous turbid surges. *Computers & geosciences*, *27*(6), 701-716.

Richards, M., Bowman, M., & Reading, H. (1998). Submarine-fan systems I: characterization and stratigraphic prediction. Marine and Petroleum Geology, 15(7), 689-717.

Shanmugam, G. (2016). Submarine fans: a critical retrospective (1950–2015). *Journal of Palaeogeography*, *5*(2), 110-184.

Simmons, S. M., Azpiroz-Zabala, M., Cartigny, M. J. B., Clare, M. A., Cooper, C., Parsons, D. R., ... & Talling, P. J. (2020). Novel acoustic method provides first detailed measurements of sediment concentration structure within submarine turbidity currents. *Journal of Geophysical Research: Oceans*, *125*(5), e2019JC015904.

Stevenson, C. J., Feldens, P., Georgiopoulou, A., Schönke, M., Krastel, S., Piper, D. J., ... & Mosher, D. (2018). Reconstructing the sediment concentration of a giant submarine gravity flow. *Nature communications*, *9*(1), 2616.

Stow, D. A., & Mayall, M. (2000). Deep-water sedimentary systems: New models for the 21st century. Marine and Petroleum Geology, 17(2), 125-135.

Straub, K. M., & Mohrig, D. (2008). Quantifying the morphology and growth of levees in aggrading submarine channels. *Journal of Geophysical Research: Earth Surface*, *113*(F3).

Talling, P. J., Allin, J., Armitage, D. A., Arnott, R. W., Cartigny, M. J., Clare, M. A., ... & Xu, J. (2015). Key Future Directions For Research On Turbidity Currents And Their Depositskey Future Directions For Research On Turbidity Currents And Their Deposits. *Journal of Sedimentary Research*, *85*(2), 153-169.

Talling, P. J., Baker, M. L., Pope, E. L., Ruffell, S. C., Jacinto, R. S., Heijnen, M. S., ... & Hilton, R. J. (2022). Longest sediment flows yet measured show how major rivers connect efficiently to deep sea. *Nature communications*, *13*(1), 4193.

Traer, M. M., Fildani, A., Fringer, O., McHargue, T., & Hilley, G. E. (2018). Turbidity current dynamics: 2. Simulating flow evolution toward equilibrium in idealized channels. *Journal of Geophysical Research: Earth Surface*, *123*(3), 520-534.

Vail, P. R. (1987). Seismic stratigraphy interpretation using sequence stratigraphy: Part 1: Seismic stratigraphy interpretation procedure.

Vail, P. R. (1991). The stratigraphic signatures of tectonics, eustasy and sedeimentology-An overview. *Cycles and events in stratigraphy.*, 617-659.

Wahab, A., Hoyal, D. C., Shringarpure, M., & Straub, K. M. (2022). A dimensionless framework for predicting submarine fan morphology. *Nature Communications*, *13*(1), 7563.

Weimer, P., & Pettingill, H. S. (2007). Global overview of deep-water exploration and production.

Winterwerp, J. C. (1998). A simple model for turbulence induced flocculation of cohesive sediment. *Journal of hydraulic research*, *36*(3), 309-326.

Winterwerp, J. C., & Van Kesteren, W. G. (2004). *Introduction to the physics of cohesive sediment dynamics in the marine environment*. Elsevier.

CHAPTER 1: A Dimensionless Framework for Predicting Submarine Fan Morphology

Abdul Wahab[1,2]*, David C. Hoyal[2], Mrugesh Shringarpure[2], & Kyle M. Straub[1]

[1]Department of Earth and Environmental Sciences, Tulane University, New Orleans, LA 70118, USA.

[2]ExxonMobil Technology and Engineering Company (EMTEC), Houston, TX, 77389

Published on 08/22/2022 in Nature Communications (https://doi.org/10.1038/s41467-022-34455-7)

Abstract

Observations of active turbidity currents at field scales offers a limited scope which challenges development of theory that links flow dynamics to the morphology of submarine fans. Here we offer a framework for predicting submarine fan morphologies by simplifying critical environmental forcings such as regional slopes and properties of sediments, through densimetric Froude (ratio of inertial to gravitational forces) and Rouse numbers (ratio of settling velocity of sediments to shear velocity) of turbidity currents. We leverage a depth-average process-based numerical model to simulate an array of submarine fans and measure rugosity as a proxy for their morphological complexity. We show a systematic increase in rugosity by either increasing the densimetric Froude number or decreasing the Rouse number of turbidity currents. These trends reflect gradients in the dynamics of channel migration on the fan surface and help discriminate submarine fans that effectively sequester organic carbon rich mud in deep ocean strata.

Introduction

Submarine fans form on continental slopes and abyssal plains in deepwater settings and are the ultimate sinks in sediment routing systems. They are crafted by turbidity currents, which arguably move more sediment on Earth than any other transport process and their deposits preserve the thickest accumulations of sediment on Earth[1]. Like deltas, the morphologies of submarine fans are quite variable[2-4] and largely result from the dynamics of the channels which move over their surfaces. Unlike deltas, where we have predictive theory for their morphology[5,6], we lack a quantitative and physics-informed theory that successfully predicts the array of observed submarine fan morphologies. This is critical as the surface dynamics that produce these morphologies influence the fidelity of climate change records housed in their strata[7], the frequency and severity of geohazards that threaten subsea infrastructures such as the network of seafloor cables that hosts the majority of global data traffic[8-10], and voluminous geofluid reservoirs[11]. In the last few decades, research has focused on the influence submarine fans have on global climate. Two avenues along this path are the management of marine litter, including the transport of microplastics into deep oceans[12], and burial of particulate organic carbon[13,14].

Turbidity currents are dilute sediment-gravity flows in which the driving gravitational force is supplied by turbulently suspended sediments[15]. These currents can travel for 10^2 hours and up to 10^3 kilometers in deepwater settings (bathymetry ~> 4000 m)[16,17], which makes direct monitoring of modern currents challenging. Further complicating the matter, our ability to infer paleo-hydraulic and sediment-transport regimes from the strata of ancient fans is limited. While physical experiments provided insight into interactions of turbidity currents with an antecedent bed topography[18-20] over short timescales, we still lack experimental methods that can produce self-formed channels by fully turbulent flows and which display sufficient mobility to form a fully dynamic fan surface[21,22].

These challenges influence the development of forward numerical models of turbidity currents and their resulting submarine fans. Some of these models carry large computational costs to solve Navier-Stokes equations for complex and fully turbulent turbidity currents. On the other side of the spectrum are rules based reduced complexity models, some of which have been around for decades but are being refined through field measurements and distillation of observations from the high fidelity models[23,24]. While these reduced complexity models generate realistic gross scale compensational stacking patterns and lobe-scale geometries over an antecedent surface, they do not account for erosion of the underlying deposits. The lack of spatial and temporal variations in deposition and erosion on the fan surface limit their applicability to unchannelized and purely depositional submarine fans.

We overcome the direct observational, experimental, and modeling limitations that prevent us from linking properties of turbidity currents to the complex morphologies of submarine fans by leveraging a previously developed, parallel process-based numerical model called EMstrata[25,26]. This model is based on the depth-average approximation of flow parameters in 3D Navier-Stokes equations of fully turbulent flows[27-30]. EMstrata solves continuity equations for fluid mass, sediment mass, linear momentum, and turbulent kinetic energy for turbidity currents: in addition to erosion and deposition of cohesive sediments[31] and flocculation of mud particles[32,33] (see methods). The depth-averaged approximations used in this model successfully simulate self-formed channels on fan surfaces that are laterally mobile and avulse through time to generate complex submarine fan morphologies.

However, the depth averaged approach means the model does not resolve evolution of surface morphologies tied to the vertical flow structure (e.g., ripples, dunes, and anti-dunes). Further, this modeling approach utilizes top hat functions for flow concentration and velocity to determine properties of flows that are stripped by partial confinement, which recent work highlights as limitations when modeling the morphodynamics of submarine fans. Specifically, it has been shown that use of self-similar shape functions that describe flow structure, and which vary as a function of the densimetric Froude Number (Fr_D) and Rouse Number (p), can aid estimation of mass and momentum fluxes[34]. These limitations noted, EMstrata captures rich dynamics of turbidity currents and their resulting deposits with reasonable computational costs, allowing investigation of hundreds of models.

Here, we posit that submarine fan morphology is largely controlled by the densimetric Froude ($Fr_D = \frac{U}{\sqrt{Rcgh}}$; where U is the down system current velocity, R is the submerged specific gravity of sediment, c is volumetric sediment concentration, g is gravitational acceleration, and h is the current thickness) and Rouse ($p = \frac{w_s}{ku_*}$; where w_s is the sediment fall velocity, k = von Kármán's constant, and u_* is the flow shear velocity) numbers of turbidity currents. More specifically, we hypothesize that flows with low Fr_D and p numbers transport most of their sediment in suspension through a growing network of branching channels and generate distributive fan morphologies. Whereas flows with high Fr_D and high p numbers transport sediment in both suspension and bedload through networks that are often defined by a single channel that avulses over time to generate a radial fan morphology.

We initiate simulations by introducing a depth-averaged turbidity current which traverses an inlet channel into a square domain that is scaled by the advection length of the median grain size in suspension (Fig. 1). The initial surface slope is a dependent parameter defined by a choice of Fr_D, clear water entrainment and drag (see methods). The range of Fr_D explored resulted in models with initial slopes between 0.065° to 3.63°, similar to slopes observed on continental margins[35]. Further, the setup of our numerical experiments is designed to explore net depositional submarine fans downstream of canyons or deposits that develop downslope of relatively immobile feeder channels. To isolate the influence of flow hydraulics and sediment-transport capacity on submarine fan shape and dynamics we neglect subsidence and changing climatic forcings (i.e. sea-level, water flux, and sediment supply) within model runs. Simulations are stopped after a defined volume of sediment is released into the model domain.

Results

The dimensionless regime

Classification systems exist for submarine fans based on characteristics of the terrestrial feeder system[36], preserved grain sizes[37,38], facies associations[39-41], and preserved morphology[42,43]. Other studies leverage observations that fans on high slopes (e.g. Squamish and Golo fans) are generally small (< 10's of km) and sandy[2,14], intermediate slope fans (e.g. Gulf of Cadiz and East Breaks) contain both sand and mud[3,44], and fans that form on low slopes (e.g. Zaire fan) are large (> 1000 km) and rich in mud content[4,45]. While the studies that underpin these classification systems report correlations for parameters that influence fan shape, they generally carry tremendous scatter, which limits their predictive power. Many of these classification systems assume links to the hydraulics and sediment-transport capacity of turbidity currents, but we currently lack a predictive framework that explicitly links fan shape to flow processes.

We propose a dimensionless regime where submarine fan dynamics and resulting morphology are defined by two dimensionless variables, Fr_D and p that weigh competing forces in turbidity currents (Fig. 2). The Fr_D quantifies the ratio of inertial to gravitational forces within a flow, while the p describes the ratio of settling velocity of sediments to shear velocity in the flow. To implement this regime, we solve for an antecedent slope, which we set as our initial bathymetric gradient, from a choice of Fr_D as function of bed friction and clear water entrainment[46]. We compute for the median grain diameter in suspension at the inlet from a choice of p as a function of settling velocity. While Fr_D and p dynamically change over the evolving fan surface, we classify fans based on their inlet Fr_D and p values. To capture a wide range of morphodynamic behaviors, we explore ranges in Fr_D and p for a depth-averaged turbidity current (Supplementary Table 1). To avoid either highly erosional or purely depositional flows, we performed sensitivity analyses that guided the range of conditions explored.

End member morphodynamics

The simulated submarine fans in our regime diagram have morphologies and surface dynamics that are defined by Fr_D and p and display striking similarity to both modern and preserved examples of submarine fans (Fig. 3-5). In this section, we focus on endmember submarine fans that are crafted by turbidity currents characterized by subcritical ($Fr_D < 1$), transcritical ($Fr_D \sim 1$) and supercritical ($Fr_D > 1$) flow and defined sediment-transport conditions through p. Each numerical submarine fan defined by the aforementioned conditions is then compared to a field counterpart with similar forcing conditions i.e., estimated Fr_D and p (see methods). We note that the absolute scales of some of our simulated fans are small relative to field scale systems, particularly the subcritical end members. This is purely a consequence of the input height of our currents and the model stopping condition, which was picked to limit computational costs for the hundreds of runs we perform. Thus, our goal is not to simulate any particular system, but rather to compare the general morphological complexity of field scale fans with modeled fans that share similar forcings as defined by Fr_D and p. To accomplish this, we will also use a dimensionless metric, rugosity, to quantify the morphological complexity of submarine fans.

Our model captures both large and small-scale geomorphic features of subcritical and low p fans that are preserved on low slopes (e.g., Zaire[4,45]) (Fig. 3a-c & supplementary movie 1). We observe multiple self-formed sinuous channels bound by prominent levees (Fig. 3b-c). These fans are crafted by channel networks that fluctuate between one-to-many active channels. The channels generate a distributive pattern by avulsing at a variety of distances from the inlet channel (Fig. 3b-c). While we force the simulations with inlet subcritical ($Fr_D < 1$) flow, the flow behavior over the emergent fan is not subcritical everywhere on the fan surface. For example, on the levees, flow tends to locally change criticality and induce formation of cyclic steps[47] (Fig. 3d). However, the average flow conditions in the inlet channel and the emergent self-formed channels maintain a mean subcritical ($Fr_D < 1$) state. We observe a hierarchy of bifurcations that help partition flux of sediment and water moving through the growing distributive network (Fig. 3b-c). This partitioning is variable and leads to the formation of asymmetric branching channels. In these fans, sand is mainly transported in channels, while silts and muds are deposited on levees, lobes, and distal parts of the outer fan (Fig. 3e).

Transcritical and intermediate p submarine fan surfaces (e.g., Gulf of Cadiz and East Breaks)[3,44] are characterized by self-formed low sinuosity channels that extend in the primary flow direction (Fig. 4a-c & supplementary movie 2). The channels are bound by well-formed levees that help maintain the bypass conditions for most of their simulated time (Fig. 4d). The channel avulses infrequently after increased aggradation rates within the channel causes a decrease in flow confinement. The newly formed channels extend in the major flow direction, which eventually leads to an ellipsoidal fan morphology. In this type of fan, sand is transported in the channels and deposited on lobes and proximal levees, whereas silt and mud are deposited on the distal parts of the fan surface (Fig. 4e).

Supercritical and high p submarine fans (e.g. Squamish fan)[2] are characterized by a self-formed single low-sinuosity channel (Fig. 5a-b & supplementary movie 3). At the channel-lobe transition the flow undergoes a hydraulic jump, where the increased flow height and loss of turbulence lead to deposition of sediments in the form of cyclic steps[48-50] (Fig. 5b-d). These cyclic steps migrate upstream in the channel until the flow confinement decreases and an avulsion is triggered. This type of fan is predominantly sandy because flow shear stresses inhibit deposition of silt and mud (Fig. 5e). The absence of flux partitioning at the channel-lobe transition and avulsions triggered in a single channel system that visits many locations through time induces an overall radial fan shape.

Submarine fan shape and texture

The shape of submarine fans and the size of the particles they house provide insight into the hydraulics and sediment-transport capacity of the flows that constructed them. Here we focus on the planform complexity of submarine fans and use regional bathymetric slopes (or slope estimates for paleo-fans) and deposit grain sizes to constrain the Fr_D and p responsible for constructing a given fan. First, we quantify the rugosity of submarine fans as a proxy for the complexity of their morphologies (Fig. 6a). Contrary to deltas, where the shoreline represents an important contour for delta front deposition[6], there is no established contour that reflects the influence of forcing conditions on submarine fan shape. We overcome this by utilizing a deposit thickness contour that delineates the depositional midpoint in submarine fans. Specifically, we use a mass-balance transformation[51], which measures downstream distance in terms of sediment mass lost to deposition in a basin. We define a dimensionless mass extraction parameter, �, as:

$$\chi(r) = \frac{1}{V_{s,b}} \int_0^L B(r) H_s(r) dr \qquad \text{(Eq. 1)}$$

Where $V_{s,b}$ is the total volume of sediment stored in the basin, L is the total downstream length of a basin, B is the basin width at a radial distance measured from the end of the entrance channel r, and H_s is the average thickness of preserved strata along a strike transect defined by r. The value of χ ranges between 0 and 1, for instance, a value of 0.5 implies that half of the sediment stored in a basin is upstream of that location. We compute for a semicircle with an origin at the end of the inlet channel and a radius equivalent to $\chi = 0.5$. We contour the fan based on the mean deposit thickness on this semi-circle and evaluate its rugosity as,

$$R(\chi = 0.5) = \frac{1}{N} \sum_{i=1}^{n} \frac{|r_c - r_{mid}|}{r_{mid}} \qquad \text{(Eq. 2)}$$

where N is the number of deposit thickness maps (see Supplementary Note 1), n is number of x-y locations on the semicircle, r_c is the radial distance between the origin of the semicircle and an x-y location on the mean thickness contour, and r_{mid} is the radius of the $\chi = 0.5$ semicircle (Fig. 6a). We exclude models that exhibit near complete sediment bypass.

The simulations show a systematic increase in planform roughness, quantified through rugosity, as one explores from the low Fr_D and high p corner of the regime diagram towards the high Fr_D and low p domain (Fig. 6b). We interpret the joint influence of Fr_D and p on fan rugosity as thus. Given fans of constant Fr_D, decreasing p results in longer transport distances for particles in suspension, allowing active and relatively stable channels to quickly prograde. In addition, decreasing p leads to more poorly sorted sediments, due to our inlet suspension criteria (see methods). Like prior research on deltaic channels[6], we propose that an increase in sorting promotes more frequent and asymmetric channel bifurcations, leading to multiple active channels. While this increase in active channels facilitates the delivery of sediment to more fan locations, the stable and asymmetric nature of these channels results in jagged contours with high rugosity values.

Traversing our regime along paths of constant p but increasing Fr_D corresponds to higher shear velocities for flows of equivalent thickness at the inlet, which inhibits deposition of silts and finer sands and promotes the maintenance of fewer active channels. These channels terminate in a single large mouth bar deposit covered with backstepping cyclic steps. This promotes channel mobility through infrequent avulsions caused by the loss of confinement due to the backstepping bedforms. As a result, fan rugosity increases due to the elongation of the relatively active few channels, contrary to the processes responsible for increasing rugosity through decreasing p. However, as Fr_D increases past criticality sediment bypass conditions are reached and further increases in Fr_D produce unfavorable conditions for channel initiation and maintenance.

Surface and subsurface predictions

While rugosity alone is not a unique indicator of Fr_D and p, fan rugosity coupled with knowledge of one of these parameters allows for the estimation of the other. For example, the rugosity of modern submarine fans can be estimated with high resolution bathymetric and shallow seismic surveys, whereas for ancient fan deposits it can be estimated with industry-grade 3-D seismic surveys. Fr_D can then be estimated with the regional (paleo)slopes and existing empirical functions for drag coefficients and clear water entrainment[46], as implemented in our model. Fan rugosity and Fr_D can then be used to invert for the p of the inlet flow to a fan. Furthermore, sediment sizes suspended in the inlet flow can be estimated from knowledge of the feeder channel depth. This would involve estimating the shear velocity of the inlet flow from channel depth and Fr_D, followed by use of the p to solve for sediment sizes in transport through a settling velocity.

Alternatively, estimates of flow p in a fan feeder channel coupled with fan rugosity allows for the inversion of Fr_D. Here, the challenge is to estimate a paleo-flow p of the feeder channel. This can be done with access to statistics of deposit grain sizes, for example from core measurements. This would entail using an assumption that the largest preserved particles met a Shield's criterion, which could be used to invert for a shear velocity. The p can then be calculated with a characteristic settling velocity of the median particle size in transport. To accomplish this, we found and utilized an empirical relationship (see methods) between fan rugosity and a ratio formed by the sizes of the median particles in transport to the median size in the deposit (Fig. 7a-b).

In the last decade measurements of active flow processes in submarine channels, which were once rare and largely limited to cable breaks, are becoming more common. This data is aiding our characterization of these important transport processes and parameterization of numerical models. However, data collection is still limited to systems that are active today and limited to several highly instrumented settings[16,52,53]. The regime space we propose allows formative flow conditions to be inferred in settings where we still lack active flow measurements, which could aid geohazards risk assessment and estimation of organic carbon fluxes and reservoirs in the deep ocean.

Discussion

Defining conditions that lead to the diversity of submarine fan morphologies found on the ocean floor opens the potential for inversion of fan form for paleo-environmental reconstructions and prediction of their future role in the global carbon cycle. We link the complexity of submarine fan form to critical dimensionless parameters that are proxies for the gradients of continental margins and the particle sizes in transport. However, we note these *dimensionless* variables are constructed with important *dimensional* parameters (e.g. current thickness, mean velocity, and diameter of particles in transport). Further, we note that many large fan systems, including the Zaire[4,45], Indus[54], and Bengal fans[13], are found on low gradient margins and house fine-grained deposits. In contrast, many steep margin and sandy systems are small in scale[2,53]. This dimensional correlation between fan size, margin gradient and preserved deposit texture might point to important contributions from the dimensional parameters housed in the Fr_D and p. To test the importance of scale on our results, namely the dimensionless regime, we ran sensitivity tests in which a suite of fans were generated (Fig. 8 a-c). These runs had different combinations of input flow thickness (Fig. 8 b), velocity (Fig. 8 c), and particle sizes, but shared equivalent Fr_D and p. The results of these tests support our hypothesis that submarine fan complexity is set by the Fr_D and p

of the turbidity currents that formed them. While gradient and particle sizes delivered to a fan are correlated to a fan's size, the complexity of its shape is set by flow and sediment-transport fields. Specifically, Fr_D influences the morphology of a submarine fan by setting thresholds in erosion and deposition in combination with a choice of p. A component of the correlation between fan size, gradient, and particle sizes can also be explained from our dimensionless parameters. For example, a flow that is characterized by low Fr_D and p generates a fan surface that is large in scale due to increased advection lengths of the median grain sizes in suspension, compared to a fan that is formed by flows that have a higher Fr_D and p. We show this scale difference in the simulated fans of our regime diagram (Fig. 2) where subcritical fans ($Fr_D < 1$) reach up to 40 kms of downstream length as compared to some supercritical fans ($Fr_D > 1$) that are less than 10 km in downstream length.

Turbidity currents are intermittent phenomena[16,17], with current heads that are often characterized by higher shear stresses than the body of the flows. We explore the sensitivity of submarine fan morphology to intermittent flows (see methods and Fig. 9 a-b). We find that flow intermittency does not significantly influence fan rugosity, with values changing due to flow intermittency by 2-10%. However, we note that intermittent flows built relatively deeper channels. Intermittent flows introduce relatively more frequent current heads that possess relatively higher shear velocities, which help maintain sediment in suspension. This phenomenon suppresses sedimentation rates within channels and could potentially impact the frequency or magnitude of avulsions on submarine fans and the resulting stratigraphic architecture. We show that flow intermittency appears to be a second order control on fan shape, when compared to the influence of Fr_D and p (Fig. 9 a-b & supplementary movie 4-6).

Our last sensitivity analysis centers on the role of cohesive sediment on fan shape. This is motivated by studies of other depositional forms, for example deltas, where sediment cohesion has been linked to the rugosity of shorelines[6] . We investigate this by varying the input mud content in the flow and examine how the percent of the total sediment concentration comprised of clay particles influences the absolute magnitude of the resulting morphology metrics (Fig. 10). We find that while changing mud content over a range of 5-60% of the input flux did change the specific placement of channels and lobes, it only produced modest changes in fan rugosity (at most 17% from our base case models). As such, a third axis defined by mud content could be generated for the regime diagram implemented here to account for erosion and deposition dynamics imparted by the cohesive fraction of the sediment concentration. However, this third axis is likely less significant for fan rugosity than the axes defined by Fr_D and p.

For turbidity currents to propagate any significant distance, they must generate enough turbulence to enable suspension of sediments[15,55]. We minimize deposition of sediment at the inlet-fan transition by enforcing a constraint on the largest sediment size (D_{99}) at the inlet, such that $w_{s,D99} <= u_*$. This constraint leads to emerging trends in sorting, which becomes a parameter dependent on choices of Fr_D and p at the inlet (Supplementary Fig. 1). We find that sorting influences the fraction of a fan surface covered by active channels and the style and rate of channel mobility. Submarine fans constructed by low Fr_D and p, coupled with poor sediment sorting, show a higher degree of channelization and development of distributary networks. The development of these complex networks can be linked to the wide range of settling velocities for the particles in transport, which leads to spatially variable deposition and erosion rates. This generates multiple nucleation sites for channel initiation and the formation of mouth bars that drive channel bifurcation (Fig. 3c). We note that both degree of channelization and the distributary nature of the emergent channels decreases when Fr_D and p increase, as flows become well sorted. In these fans, the incoming flows rapidly become purely depositional, suppressing the growth of complex channel patterns. We note that at extremely high Fr_D values channelization is lost as most sediment bypasses the domain, hindering levee development that confines flows (Fig. 2). Future investigations could explore different criteria to define input grain size distributions, for example, keeping sorting constant across a spectrum of Fr_D and p, which may possibly quantify further the influence of sorting on emergent patterns of channel networks on the fan surface.

While the Knapp-Bagnold criteria aids in reducing deposition downstream of the inlet channel, we note that in some models (Low Fr_D and high p) produce high initial deposits near the end of the inlet channel. This results in a steepening of the fan relative to the initial domain slope that was defined through a choice of Fr_D (Fig. 6a). Much of this steepening is associated with deposition that constructs topography necessary to confine flows early in the simulations. However, even after construction of confining topography, models had steeper slopes than defined with the Fr_D closure, which is independent of p. This highlights the need for development of relationships to predict bypass slopes that incorporate Fr_D, p, and sorting within turbidity currents and which could refine our regime diagram. While deposit slope does evolve over the course of the simulations, we note that Fr_D and p do not spatially evolve significantly within the entrance channel (Supplementary Fig. 2-6). This lends support to our argument that Fr_D and p conditions in canyons or relatively immobile channels control the morphology of submarine fans and the properties of the flows in their emergent channels.

Deepwater submarine fans are the ultimate sink in routing systems and their complex morphologies have been described through a hierarchy of landforms[56], which can be linked to a hierarchy of features preserved in their strata[57,58]. Further, recent work suggests that differences in migration rates of features across hierarchical levels controls the degree to which scales of stratigraphic features (i.e. preserved channel body thickness) resemble common scales of surface features (i.e. channel depth)[59]. This complex stratigraphic hierarchy can develop even under constant environmental forcing, as we show with our model, due to intricate feedback mechanisms between flow and antecedent bed surfaces (autogenics). These autogenic processes and their stratigraphic products makes restoration of signals of paleo-environmental significance challenging[60,61]. The model leveraged in this study produces intricate autogenic behavior and a hierarchy of landforms on the fan surface, all with different migration rates, which vary as a function of Fr_D and p of turbidity currents (supplementary movie 1-3). For instance, we show that low gradient fans with relatively low p promotes a distributive network of channels that delivers sediments to many locations on the surface of a fan. The complexity of these networks is not constant over a model run and varies as channels avulse and new channels evolve with different initial conditions. As such, networks can vary in number of active distributaries anywhere between one to many. This intricate and rather dynamic style of autogenic behavior challenges stratigraphers' ability to decipher signals of environmental significance from preserved fan strata, such as from outcrops and seismic volumes. We also show that high gradient fans crafted by high Fr_D tend to localize deposition in and at the terminus of a single channel network. This style of deposition at the channel-to-lobe transition facilitates choked flow conditions and triggers an avulsion, which results in a shift of locus of deposition on the fan surface. This autogenic configuration reduces the area on the fan surface that is active at any one time. The lack of compensational stacking over these meso-timescales likely imparts significant hiatuses in the fan strata, reducing the temporal completeness of preserved records. The flows that craft these single channel networks also efficiently bypass clay particles that carry sedimentary signals[7]. Combined, periods of depositional stasis on the fan surface and bypass of fines likely limits our ability to leverage high gradient strata for paleo-climatic inversions. The observed complexity in the migration dynamics of channels that emerges as a function of Fr_D and p also likely limits our ability to leverage some reduced complexity models for deciphering signals of climatic and tectonic significance from ordered submarine fan strata. This is due to the limited range of autogenic processes currently produced by some models, which often do not contain rules to describe threshold changes in autogenic processes as a function of flow and sediment-transport conditions[24] , as we highlighted in this study.

Results from our dimensionless regime diagram have implications beyond predicting the morphology of submarine fans and the inversion of fan form for paleo-environmental conditions. We show that submarine fans crafted by turbidity currents that are traversing relatively low gradients and transporting fine particles in suspension can efficiently trap more mud compared to fans crafted by turbidity currents traversing higher gradients with relatively coarse particles in suspension (Supplementary Fig. 7). We highlight that flows with subcritical Fr_D and low p favors higher settling rates for sediment that are less than 62.5 m in diameter, due to the relatively low shear velocities that characterizes these systems. A high fraction of sediment in the mud size range (< 62.5 m) consists of clays whose mineral surface properties[62] favors adsorption of particulate organic carbon, which can be preserved if rapidly buried to only several cms of depth. This suggest that subcritical fans on low slopes in deepwater settings are favorable spots for sequestering large volumes of organic carbon via increased burial rates of mud supplied by turbidity currents. The higher trapping potential and preservation rates of organic carbon in these fans[13] likely buffers long term atmospheric CO_2 levels and can significantly impact global climate change on geological timescales.

We conclude that the remarkable diversity of submarine fan morphology on the modern ocean floor can be generated solely by changing critical dimensionless variables that describe the flow and sediment-transport fields of turbidity currents. This unifying framework ties transport processes to fan form and is defined by the Fr_D and p of turbidity currents. Our results demonstrate the utility of leveraging a process-based forward model, which accounts for all important turbidity current forcing mechanisms, for simulation of complex and geologically realistic submarine fan morphology. Finally, the controls on fan complexity, highlighted in our regime space, will aid inversion of fan form for paleo-environmental conditions and help identify those fans that act as critical reservoirs in Earth’s carbon cycle.

Methods

Flow-forcing and sediment-transport parameters. In the interest of capturing a range of morphodynamic behaviors within submarine fans that are defined by different slopes and mean grain sizes, we propose a dimensionless regime space. This is achieved by defining the horizontal axis of the regime space as Fr_D, which quantifies the ratio of inertial to gravitational forces within a turbidity current. It is calculated as $Fr_D = u/\sqrt{Rgch}$, using depth-average values for important forcing variables within the flow, such as velocity (u), concentration (c), and height of the current (h). We set $c = 5\%$, $h = 5\ m$, $R = 1.65$, and $g = 9.8\ m/s^2$ at the inlet, and therefore, by varying Fr_D we only vary the velocity magnitude at the inlet. We compute for an antecedent slope $S = \left((e_w + cd) * Fr_D^2 + 0.5 * e_w\right)$, as a function of friction at the bed and clear water entrainment from a choice of Fr_D, where e_w is the clear water entrainment coefficient, calculated from the Fr_D[46], and cd is the coefficient of friction with a fixed value of 0.004. This initial slope is non-erodible. On the vertical axis, we define the $Ro = w_s/(k * u_*)$, which quantifies the ratio of settling velocity of sediments (w_s) to shear velocity (u_*) in the flow, where k is von Kármán's constant.

Input grain size distribution and criterion for suspension. We compute the mean settling velocity of sediments $< w_s >$ from a choice of p using the Dietrich[63] method, which then allows us to indirectly compute for the grain sizes in suspension (Supplementary Fig. 1a). We compute a lognormal distribution sampled by 10 quartz sediment sizes with 5 m clay particles (10% of the total sediment concertation) added to the final sediment mixture. We compute sorting (Supplementary Fig. 1b) for this log normal distribution by leveraging the Shields curve of suspension, such that D_{99} or finer sediment sizes will honor the Bagnold Criterion[15].

Scaling of the simulation domain. We scale the simulation domain by leveraging a modified version of the advection length, $la = < u > * h_c/w_s$, which describes the minimum horizontal distance over which the mean grain size within a flow can be transported before making contact with the bed[64]. In this formulation, $<u>$ is the depth-average velocity of the flow at the inlet, h_c describes the height of the center of mass within a turbidity current. This height is calculated as, $h_c = h * \left(0.5 * zc + 0.25(1 - zc)\right)$, where h is the height of the current at the inlet, and zc is the normalized distanced from the bed to the maximum volumetric concentration in the flow, and is set to 0.9 when $Fr_D < 0.5$ and $zc = 0.09 * {Fr_D}^{-2.8}$ when $Fr_D > 0.5$[65].

Boundary conditions. The evolution of topography is solved on a flat non-erodible surface with a triangular irregular network (TIN) grid of 50 m x 50 m and 1 m in vertical. For post-processing we interpolate the data onto a Cartesian grid. The entrance channel and upstream boundary walls are closed (and reflect flows), whereas the side and downstream boundaries are open and allow flows to exit the domain. We implement a model stopping condition by fixing the total volume of sediment released into the domain at 1.25×10^{11} cubic meters. As a result, subcritical cases require longer computation run-time due to relatively low velocity magnitudes, whereas supercritical simulations take relatively shorter times, given the rapid delivery of the set amount of total sediment volume.

Simulator. EMstrata uses a four equation model[27] that solves for bedload fluxes[66], erosion rates[67], deposition rates[68], flocculation of clay particles[32,33], and the influence of cohesion on the underlying deposit[31]. Models are solved using a finite volume method with a dynamic time step that is a function of grid spacing, flow velocity, and wave speed. The finite volume method captures discontinuities in the turbidity current flow such as the head of the turbidity current or a hydraulic jump. For our base case scenario of steady currents, once the current is released into the domain it contains a head that propagates through the model domain and eventually exits the simulation domain. This head develops due to sharp spatial gradients in hydrostatic pressure and shear stresses between cells that have near zero velocity or concentration, and those characterizing the current front. The model then simulates the body of the current until a new head originates from a node where the system undergoes an avulsion. The amount of morphodynamic work by the head and the body of the turbidity current is controlled by empirical closures[66-68] that are function of shear stresses within the flow. A more detailed description of the depth-averaged theory, governing equations and analyses of their approximate analytical solutions, and a choice of the numerical solver is published in prior studies[25,26].

Sensitivity of submarine fan shape to intermittent turbidity current flow. We explore the sensitivity of submarine fan morphology to intermittent flows. We choose four model runs that represented endmember behavior in the regime space (Figure 9 & supplementary movie 4-6). We set simulations by allowing 5 days of active flow discharge followed by 1 day of no flow discharge conditions to allow any remnant current or sediment load to bypass the domain before the next flow event. For these intermittent runs we did not vary any flow forcing conditions from our base case continuous flow simulations. The simulations with intermittent flows also had the same stopping conditions as the base case model runs, where a decided amount of sediment volume was released into the model domain.

Estimation of Froude and Rouse numbers for modern submarine fan examples. We estimated the Fr_D and p for flows delivered to the Zaire fan using published data of currents in the upstream canyon[52]. We approximate a Fr_D = 0.13 – 0.21 based on the measured average current velocities (U = 0.6 -1.0 m/s), the average sediment concentration (c = 0.020[16]), and the average height of the current (h = 64.8 m). We also estimated the p = 0.0035 - 0.0057 for the Zaire fan based on settling velocities (w_s = 8.62E-05 m/s) of median grain sizes (d50 = 12 um) coupled with estimates of shear velocity (u_* = 0.0379 – 0.0632 m/s) by assuming a uniform drag co-efficient (cd = 0.004) at the bed. We compare this field example to a modeled submarine fan that has a Fr_D = 0.45 at the inlet, which is slightly higher than what we estimated for the Zaire system, as this is the smallest Fr_D value modeled in our regime. We do acknowledge that our approximations of Fr_D and p for the Zaire system is an estimate base on limited active turbidity current data. For the intermediate gradient model-field comparison, we use the EastBreaks fan from basin IV of the Brazo-Trinity system offshore Texas. No direct measurements of flows exist for this locality. As such, we estimate Fr_D using Latent-Hyper cube sample of velocity, concentrations, and height of the current. We choose flow variables from this sample space that closely matched the seismic attributes of the EastBreaks fan. The estimates for height = 9m, velocity = 2.8 m/s, and a concentration of 0.05 yield Fr_D = 1.05. We estimate a p = 0.24 based on median grain sizes of 200 um from available sediment core data. For the high gradient model-field comparison, we use the Squamish fan system in British Columbia. We estimate the Fr_D (1.05 - 2.36) for this system based on active measurements of three flow events with sustain mean body speeds of 3.0 m/s[69] (personal communication with Juan J. Fedele), current height of 10 m (approximated from channel-cross profiles[53], and reasonable choices for concentration of sediments (1-

5%). We estimate p = 0.267 – 0.336 based on shear velocity (u_* = 0.150 - 0.1897 m/s) and settling velocity (w_s = 0.202 m/s) of D_{50} = 225 um from samples taken in the turbidity current during active flow[70].

Inversion to median grain sizes in transport. Our method to invert for fan forming flow Fr_D from p and fan rugosity takes advantage of deposit grain size statistics. We highlight a gradient in our regime diagram of a ratio between median particle sizes in transport to the median particle sizes preserved in the fan, GS_{Ratio}. This gradient is in the same direction as the observed gradient in fan rugosity as a function of Fr_D and p. An empirical relationship was then fit to allow for estimation of GS_{Ratio} from fan rugosity (Fig. 7).

Data availability

The entire raw dataset (100's of model runs) utilized in this campaign exceeds 100 terabytes. We therefore provide subsampled and processed thickness maps of four model runs that are used to compute for rugosity of simulated submarine fans are available on Figshare at (https://doi.org/10.6084/m9.figshare.21126169). The measured rugosity on this subsampled data may vary slightly from the values reported for the same models in the manuscript due to calculations performed on relatively fewer thickness maps (Supplementary Note 1). However, the authors confirmed that resulting gradients in rugosity across the regime diagram do not change. Therefore, this minimum dataset covers the different corners and gradients of the regime diagram and is sufficient to interpret, verify and extend the research in this manuscript. Additional model outputs could be made available upon reasonable request to the authors. The field data used for comparison to endmember model runs are third party datasets and are available upon request and permission from third party owners (see citations in the manuscript for identity of third-party owners)

Code availability

The code utilized to measure rugosity from thickness maps presented in this manuscript is available on Figshare (https://doi.org/10.6084/m9.figshare.21131260). The software (EMstrata) utilized in this study for simulating submarine fans is not available for public for propriety reasons. However, the software leverages an established numerical model that has been previously published on (see manuscript for specific citations). Important forcing parameters explored in this study are detailed in Supplementary Table 1.

References cited

1 Talling, P. J. *et al.* Key Future Directions For Research On Turbidity Currents And Their Depositskey Future Directions For Research On Turbidity Currents And Their Deposits. *Journal of Sedimentary Research* **85**, 153-169 (2015).

2 Sweet, M. L. *et al.* Sediment routing from shelf to basin floor in the Quaternary Golo System of Eastern Corsica, France, western Mediterranean Sea. *Bulletin* **132**, 1217-1234 (2020).

3 Habgood, E. L. *et al.* Deep-water sediment wave fields, bottom current sand channels and gravity flow channel-lobe systems: Gulf of Cadiz, NE Atlantic. *Sedimentology* **50**, 483-510 (2003).

4 Babonneau, N., Savoye, B., Cremer, M. & Bez, M. Sedimentary architecture in meanders of a submarine channel: detailed study of the present Congo turbidite channel (Zaiango project). *Journal of Sedimentary Research* **80**, 852-866 (2010).

5 Nienhuis, J. *et al.* Global-scale human impact on delta morphology has led to net land area gain. *Nature* **577**, 514-518 (2020).

6 Caldwell, R. L. & Edmonds, D. A. The effects of sediment properties on deltaic processes and morphologies: A numerical modeling study. *Journal of Geophysical Research: Earth Surface* **119**, 961-982 (2014).

7 Hessler, A. M. & Fildani, A. Deep-sea fans: tapping into Earth's changing landscapes. *Journal of Sedimentary Research* **89**, 1171-1179 (2019).

8 Heezen, B. C. & Ewing, W. M. Turbidity currents and submarine slumps, and the 1929 Grand Banks [Newfoundland] earthquake. *American journal of Science* **250**, 849-873 (1952).

9 Carter, L., Gavey, R., TALLING, P. J. & Liu, J. T. Insights into submarine geohazards from breaks in subsea telecommunication cables. *Oceanography* **27**, 58-67 (2014).

10 Stevenson, C. J. *et al.* Reconstructing the sediment concentration of a giant submarine gravity flow. *Nature communications* **9**, 1-7 (2018).

11 Weimer, P. & Pettingill, H. S. Global overview of deep-water exploration and production. (2007).

12 Waldschläger, K. *et al.* Learning from natural sediments to tackle microplastics challenges: A multidisciplinary perspective. *Earth-Science Reviews*, 104021 (2022).

13 Galy, V. *et al.* Efficient organic carbon burial in the Bengal fan sustained by the Himalayan erosional system. *Nature* **450**, 407-410 (2007).

14 Hage, S. *et al.* Efficient preservation of young terrestrial organic carbon in sandy turbidity-current deposits. *Geology* **48**, 882-887 (2020).

15 Bagnold, R. A. Auto-suspension of transported sediment; turbidity currents. *Proceedings of the Royal Society of London. Series A. Mathematical and Physical Sciences* **265**, 315-319 (1962).

16 Azpiroz-Zabala, M. *et al.* Newly recognized turbidity current structure can explain prolonged flushing of submarine canyons. *Science advances* **3**, e1700200 (2017).

17 Pirmez, C. & Imran, J. Reconstruction of turbidity currents in Amazon Channel. *Marine and petroleum geology* **20**, 823-849 (2003).

18 Imran, J., Parker, G. & Harff, P. Experiments on incipient channelization of submarine fans. *Journal of Hydraulic Research* **40**, 21-32 (2002).

19 Parsons, J. D. *et al.* A preliminary experimental study of turbidite fan deposits. *Journal of Sedimentary Research* **72**, 619-628 (2002).

20 Straub, K. M. & Mohrig, D. Quantifying the morphology and growth of levees in aggrading submarine channels. *Journal of Geophysical Research: Earth Surface* **113** (2008).

21 Ferguson, R. A. *et al.* Entangled external and internal controls on submarine fan evolution: an experimental perspective. *The Depositional Record* **6**, 605-624 (2020).

22 De Leeuw, J., Eggenhuisen, J. T. & Cartigny, M. J. Morphodynamics of submarine channel inception revealed by new experimental approach. *Nature communications* **7**, 1-7 (2016).

23 Teles, V., Chauveau, B., Joseph, P., Weill, P. & Maktouf, F. CATS–A process-based model for turbulent turbidite systems at the reservoir scale. *Comptes Rendus Geoscience* **348**, 489-498 (2016).

24 Burgess, P. M., Masiero, I., Toby, S. C. & Duller, R. A. A big fan of signals? Exploring autogenic and allogenic process and product in a numerical stratigraphic forward model of submarine-fan development. *Journal of Sedimentary Research* **89**, 1-12 (2019).

25 Halsey, T. C., Kumar, A. & Perillo, M. M. Sedimentological regimes for turbidity currents: Depth-averaged theory. *Journal of Geophysical Research: Oceans* **122**, 5260-5285 (2017).

26 Halsey, T. C. & Kumar, A. Levees Formed by Turbidity Currents: A Depth-Averaged Modeling Treatment. *Journal of Geophysical Research: Oceans* **124**, 4389-4415 (2019).

27 Parker, G., Fukushima, Y. & Pantin, H. M. Self-accelerating turbidity currents. *Journal of Fluid Mechanics* **171**, 145-181 (1986).

28 Traer, M., Fildani, A., Fringer, O., McHargue, T. & Hilley, G. Turbidity current dynamics: 2. Simulating flow evolution toward equilibrium in idealized channels. *Journal of Geophysical Research: Earth Surface* **123**, 520-534 (2018).

29 Imran, J., Parker, G. & Katopodes, N. A numerical model of channel inception on submarine fans. *Journal of Geophysical Research: Oceans* **103**, 1219-1238 (1998).

30 Pratson, L. F., Imran, J., Hutton, E. W., Parker, G. & Syvitski, J. P. BANG1D:: a one-dimensional, Lagrangian model of subaqueous turbid surges. *Computers & geosciences* **27**, 701-716 (2001).

31 Winterwerp, J. C. & Van Kesteren, W. G. *Introduction to the physics of cohesive sediment dynamics in the marine environment*. (Elsevier, 2004).

32 Kuprenas, R., Tran, D. & Strom, K. A shear-limited flocculation model for dynamically predicting average floc size. *Journal of Geophysical Research: Oceans* **123**, 6736-6752 (2018).

33 Winterwerp, J. C. A simple model for turbulence induced flocculation of cohesive sediment. *Journal of hydraulic research* **36**, 309-326 (1998).

34 Dorrell, R. *et al.* The critical role of stratification in submarine channels: implications for channelization and long runout of flows. *Journal of Geophysical Research: Oceans* **119**, 2620-2641 (2014).

35 Pratson, L. F. & Haxby, W. F. What is the slope of the US continental slope? *Geology* **24**, 3-6 (1996).

36 Clark, J., Kenyon, N. & Pickering, K. Quantitative analysis of the geometry of submarine channels: implications for the classification of submarine fans. *Geology* **20**, 633-636 (1992).

37 Richards, M., Bowman, M. & Reading, H. Submarine-fan systems I: characterization and stratigraphic prediction. *Marine and Petroleum Geology* **15**, 689-717 (1998).

38 Stow, D. A. & Mayall, M. Deep-water sedimentary systems: new models for the 21st century. *Marine and Petroleum Geology* **17**, 125-135 (2000).

39 Bouma, A. H. Sedimentology of some flysch deposits. *Agraphic approach to facies interpretation* **168** (1962).

40 Lowe, D. R. Sediment gravity flows; II, Depositional models with special reference to the deposits of high-density turbidity currents. *Journal of sedimentary research* **52**, 279-297 (1982).

41 Mutti, E. & Ricci Lucchi, F. Turbidites of the northern Apennines: introduction to facies analysis. *International geology review* **20**, 125-166 (1978).

42 Vail, P. The stratigraphic signatures of tectonics, eustacy and sedimentology-an overview. *Cycles and events in stratigraphy*, 617-659 (1991).

43 Shanmugam, G. Glossary: A supplement to "Submarine fans: A critical retrospective (1950–2015)" in the Journal of Palaeogeography (2016, 5 [2]). *Journal of Palaeogeography* **5**, 258-277 (2016).

44 Prather, B. E. *et al.* Stratigraphy of linked intraslope basins: Brazos-Trinity system western Gulf of Mexico. *Application of the principles of seismic geomorphology to continental-slope and base-of-slope systems: Case studies from seafloor and near-seafloor analogues: SEPM, Special Publication* **99**, 83-109 (2012).

45 Picot, M., Droz, L., Marsset, T., Dennielou, B. & Bez, M. Controls on turbidite sedimentation: insights from a quantitative approach of submarine channel and lobe architecture (Late Quaternary Congo Fan). *Marine and Petroleum Geology* **72**, 423-446 (2016).

46 Parker, G., Garcia, M., Fukushima, Y. & Yu, W. Experiments on turbidity currents over an erodible bed. *Journal of Hydraulic Research* **25**, 123-147 (1987).

47 Fildani, A., Normark, W. R., Kostic, S. & Parker, G. Channel formation by flow stripping: Large-scale scour features along the Monterey East Channel and their relation to sediment waves. *Sedimentology* **53**, 1265-1287 (2006).

48 Mutti, E. & Normark, W. R. in *Marine clastic sedimentology* 1-38 (Springer, 1987).

49 Garcia, M. & Parker, G. Experiments on hydraulic jumps in turbidity currents near a canyon-fan transition. *Science* **245**, 393-396 (1989).

50 Hamilton, P. B., Strom, K. B. & Hoyal, D. C. Hydraulic and sediment transport properties of autogenic avulsion cycles on submarine fans with supercritical distributaries. *Journal of Geophysical Research: Earth Surface* **120**, 1369-1389 (2015).

51 Strong, N., Sheets, B., Hickson, T. & Paola, C. in *Fluvial sedimentology VII* Vol. 35 243-253 (International Association of Sedimentologists Special Publication 35, 2005).

52 Simmons, S. *et al.* Novel acoustic method provides first detailed measurements of sediment concentration structure within submarine turbidity currents. *Journal of Geophysical Research: Oceans* **125**, e2019JC015904 (2020).

53 Vendettuoli, D. *et al.* Daily bathymetric surveys document how stratigraphy is built and its extreme incompleteness in submarine channels. *Earth and Planetary Science Letters* **515**, 231-247 (2019).

54 Bourget, J. *et al.* Late Quaternary megaturbidites of the Indus Fan: Origin and stratigraphic significance. *Marine Geology* **336**, 10-23 (2013).

55 Knapp, R. T. Energy-balance in stream-flows carrying suspended load. *Eos, Transactions American Geophysical Union* **19**, 501-505 (1938).

56 Deptuck, M. E., Piper, D. J., Savoye, B. & Gervais, A. Dimensions and architecture of late Pleistocene submarine lobes off the northern margin of East Corsica. *Sedimentology* **55**, 869-898 (2008).

57 Prelat, A., Covault, J., Hodgson, D., Fildani, A. & Flint, S. Intrinsic controls on the range of volumes, morphologies, and dimensions of submarine lobes. *Sedimentary Geology* **232**, 66-76 (2010).

58 Straub, K. M. & Pyles, D. R. Quantifying the hierarchical organization of compensation in submarine fans using surface statistics. *Journal of Sedimentary Research* **82**, 889-898 (2012).

59 Ganti, V., Hajek, E. A., Leary, K., Straub, K. M. & Paola, C. Morphodynamic hierarchy and the fabric of the sedimentary record. *Geophysical Research Letters* **47**, e2020GL087921 (2020).

60 Hajek, E. A. & Straub, K. M. Autogenic sedimentation in clastic stratigraphy. *Annual Review of Earth and Planetary Sciences* **45**, 681-709 (2017).

61 Paola, C. A mind of their own: recent advances in autogenic dynamics in rivers and deltas. *Autogenic Dynamics and Self-Organization in Sedimentary Systems: Society for Sedimentary Geology Special Publication* **106**, 5-17 (2016).

62 Mayer, L. M. Surface area control of organic carbon accumulation in continental shelf sediments. *Geochimica et Cosmochimica Acta* **58**, 1271-1284 (1994).

63 Dietrich, W. E. Settling velocity of natural particles. *Water resources research* **18**, 1615-1626 (1982).

64 Ganti, V., Lamb, M. P. & McElroy, B. Quantitative bounds on morphodynamics and implications for reading the sedimentary record. *Nature communications* **5**, 1-7 (2014).

65 Sequeiros, O. E. Estimating turbidity current conditions from channel morphology: A Froude number approach. *Journal of Geophysical Research: Oceans* **117** (2012).

66 Meyer-Peter, E. & Müller, R. in *IAHSR 2nd meeting, Stockholm, appendix 2.* (IAHR).

67 Garcia, M. & Parker, G. Entrainment of bed sediment into suspension. *Journal of Hydraulic Engineering* **117**, 414-435 (1991).

68 Garcia, M. H. Depositional turbidity currents laden with poorly sorted sediment. *Journal of hydraulic engineering* **120**, 1240-1263 (1994).

69 Hughes Clarke, J. & Fedele, J. in *AGU Fall Meeting Abstracts.* OS31A-08.

70 Hage, S. *et al.* Direct monitoring reveals initiation of turbidity currents from extremely dilute river plumes. *Geophysical Research Letters* **46**, 11310-11320 (2019).

Acknowledgements

This study is funded by ExxonMobil Upstream Research Company. We greatly acknowledge members of Process Stratigraphy at ExxonMobil Upstream Research Company, for providing training and access to high performance computing tools to the lead author for generating the dataset utilized in this campaign.

Author contributions

The authors contributed to this manuscript as follows, D.C.H, K.M.S, M.S and A.W conceived of this study and developed the theoretical framework; A.W carried out the numerical work with assistance and guidance from M.S; A.W processed and interpreted the data; D.C.H, M.S, and K.M.S reviewed the interpretations; A.W and K.M.S wrote the manuscript with feedback from D.C.H and M.S.

Competing Interests

The authors declare no competing interests.

Additional Information

Correspondence and requests for materials should be addressed to A.W.

Figures

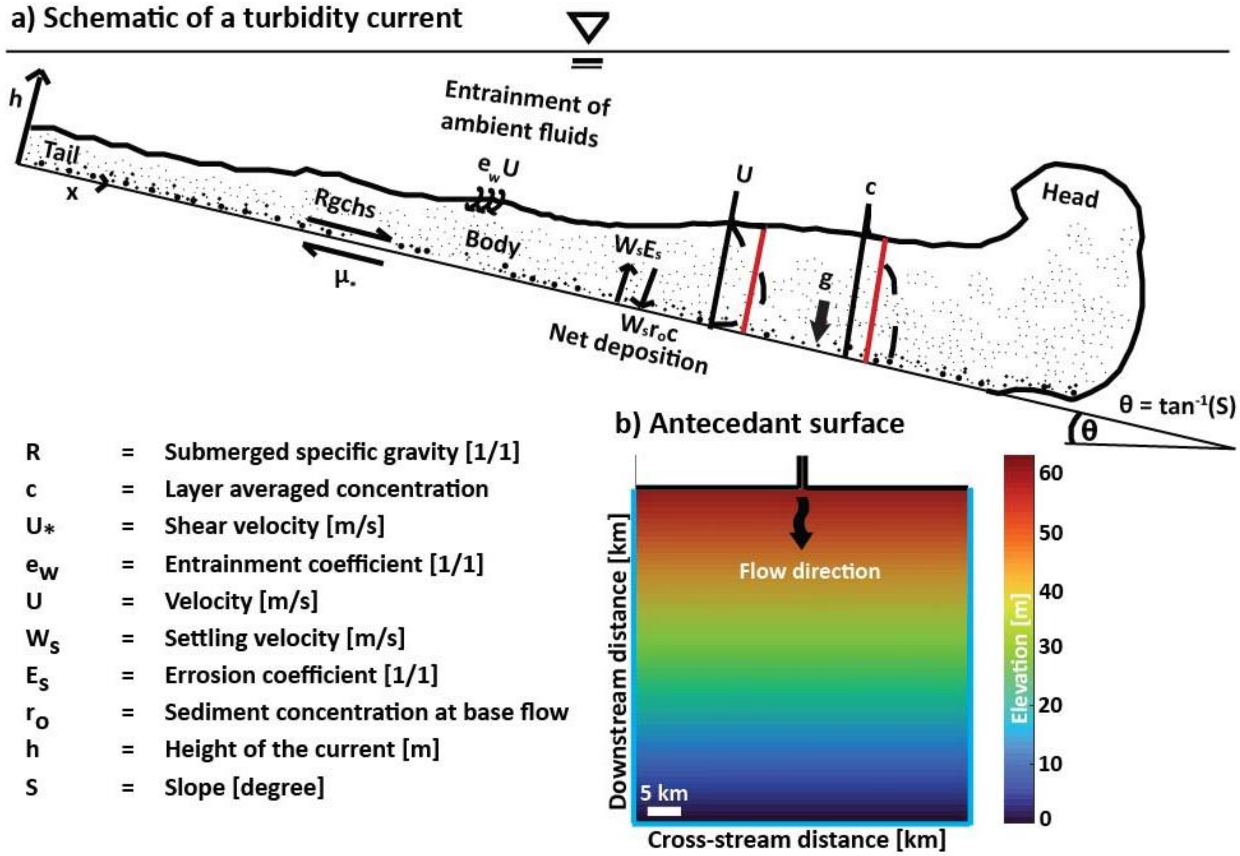

Figure 1 | Numerical setup. a, Schematic cross-section of a turbidity current with important depth-averaged terms highlighted in red. b, Example of a model domain [50 x 50 km] with a flat non-erodible slope. Black lines trace upstream boundaries of domain that are closed and reflect flow, whereas blue lines trace boundaries that are open and allow the flow to exit the domain.

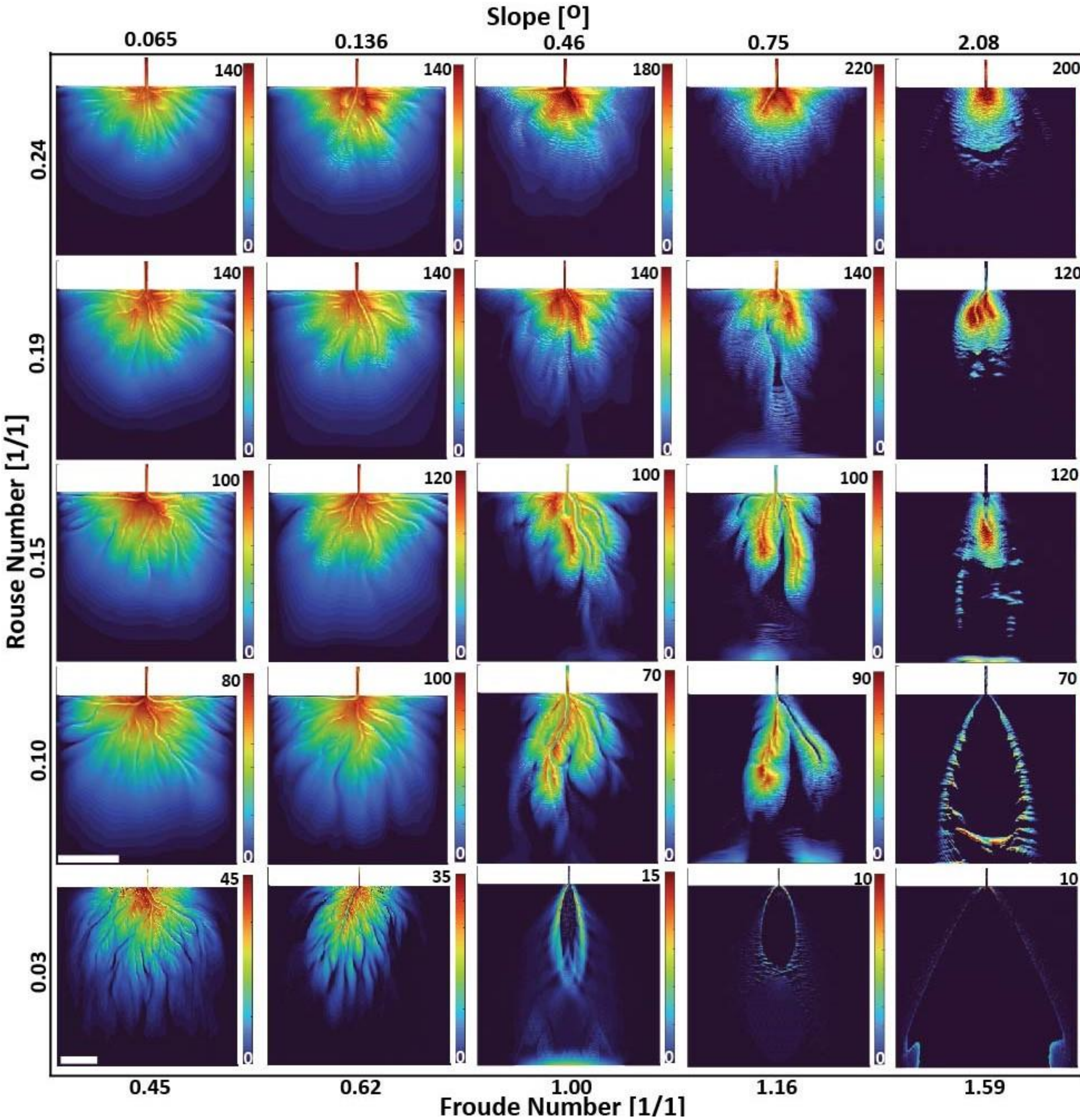

Figure 2 | Dimensionless regime diagram. A subset of simulated fans displays different planform morphologies that result from defined combinations of FrD and p. Note that range of fan thicknesses displayed in color and the horizontal scale vary between models. White bars denote 10 km of length and colored bars represents deposit thickness in meters. Models in the last row have domain size of 55 x 50 km whereas the remaining models have a domain size of 35 x 30 km. Additional variables are listed in Supplementary Table 1.

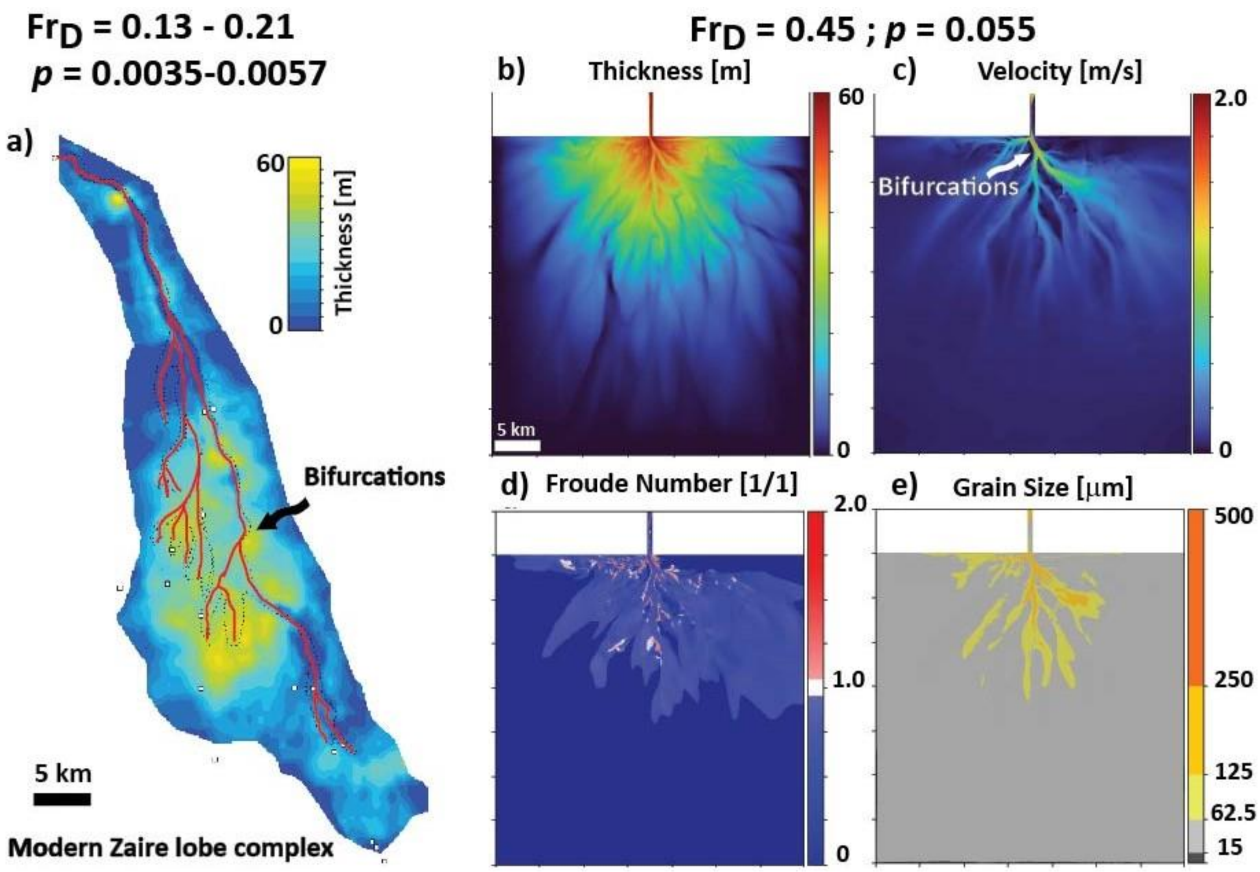

Figure 3 | Comparison of a simulated subcritical fan to the modern Zaire fan system, offshore Congo. a, Deposit thickness map of the modern Zaire fan system generated using ZaiAngo surveys[4]. b, Deposit thickness (m). c, Velocity field on the active fan surface. d, FrD state on the active fan surface. e, Grain sizes on the active fan surface. The subcritical fan simulation is characterized by a distributive transport pattern, multiple active and sinuous channels, a hierarchy of bifurcations, and overall mud rich deposit that resembles the Zaire fan[4] (a). For the evolution of this modeled subcritical submarine fan see supplementary movie 1.

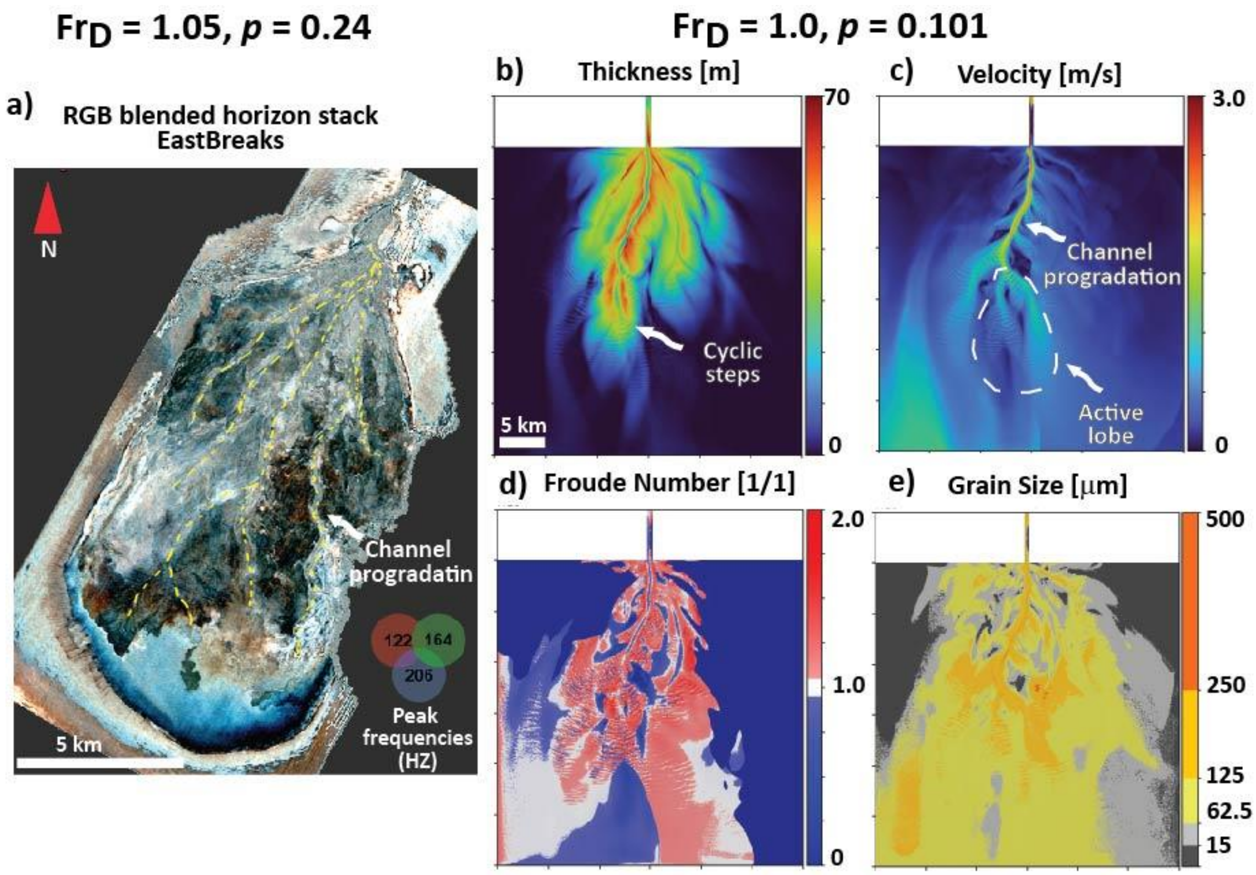

Figure 4 | Comparison of a simulated transcritical fan to the Quaternary East Breaks Basin-IV submarine fan, offshore Gulf of Mexico. a, spectrally decomposed seismic horizon of the East Breaks Basin-IV submarine fan. The yellow dotted lines highlight channelized bodies that prograded into Basin-IV. b, Deposit thickness (m). c, Velocity field on the active fan surface. d, Fr_D state on the active fan surface. e, Grain sizes on the active fan surface. The transcritical fan simulation (b-e) shows a sinuous channel that progrades into the basin (b-c), formation of cyclic steps on the active lobe surface (b), and distribution of grain sizes on the active fan surface (e). For the evolution of this modeled transcritical submarine fan see supplementary movie 2.

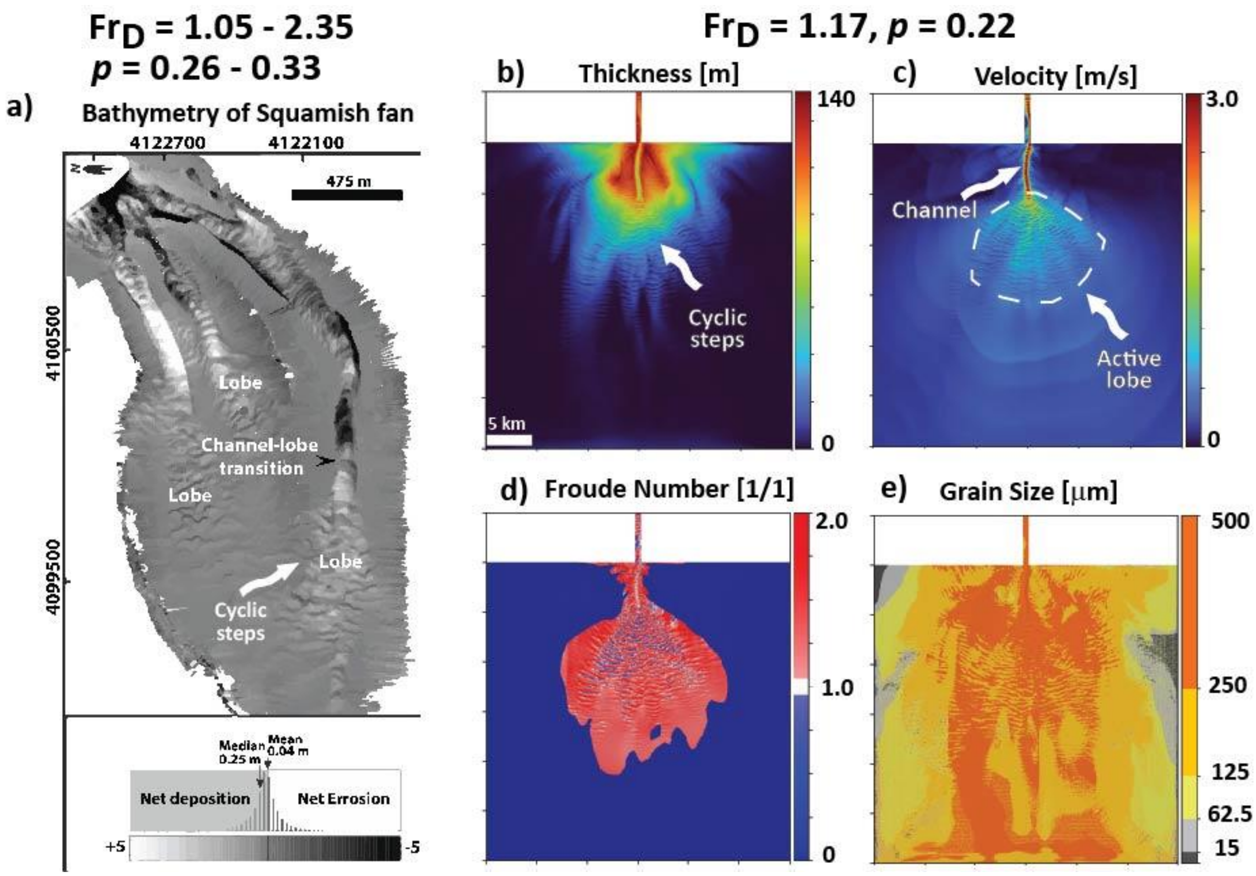

Figure 5 | Comparison of a simulated supercritical fan to the modern Squamish fan, offshore British Colombia. a, Bathymetry map of the modern Squamish fan[53]. b, Deposit thickness (m). c, velocity field on the active fan surface. d, FrD state on the active fan surface. e, Grain sizes on the active fan surface. The supercritical fan simulation (b-e) shows characteristic cyclic bedforms (a) formed due to hydraulic jumps, a single active and low-sinuosity channel (c), and sand rich deposit (e) that resembles a high slope modern fan[53] (a). For the evolution of this modeled supercritical submarine fan see supplementary movie 3.

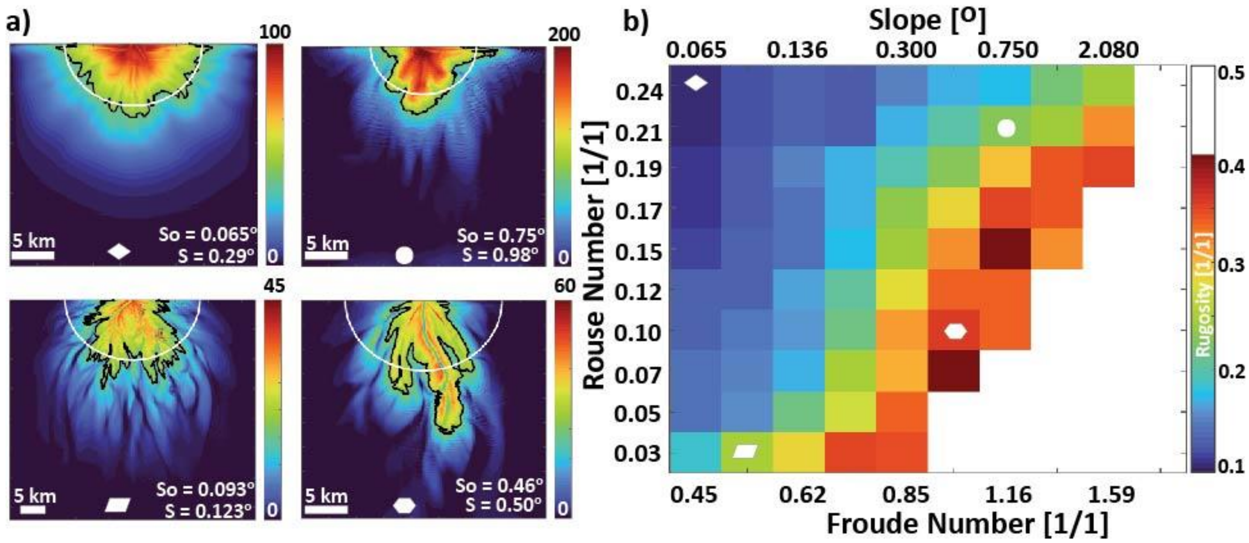

Figure 6 | Morphology of simulated fans. a, Deposit thickness maps for select submarine fans show contour used to measure rugosity. The white semicircle defines a distance from the inlet upstream of which half of the sediments in the model domain are stored. The black contour is computed for a mean elevation along the semicircle. Color bars denote thickness [m]. Slopes reported were measured from the entrance channel to the end of the deposit on down system transects. So is the antecedent slope (o) and S(o) is measured at the end of the model run. b, Matrix shows computed rugosity for all models. White area represents models in which input sediment largely bypassed model domains. Symbol correspond to rugosity measurements for fans displayed in Fig. 6a.

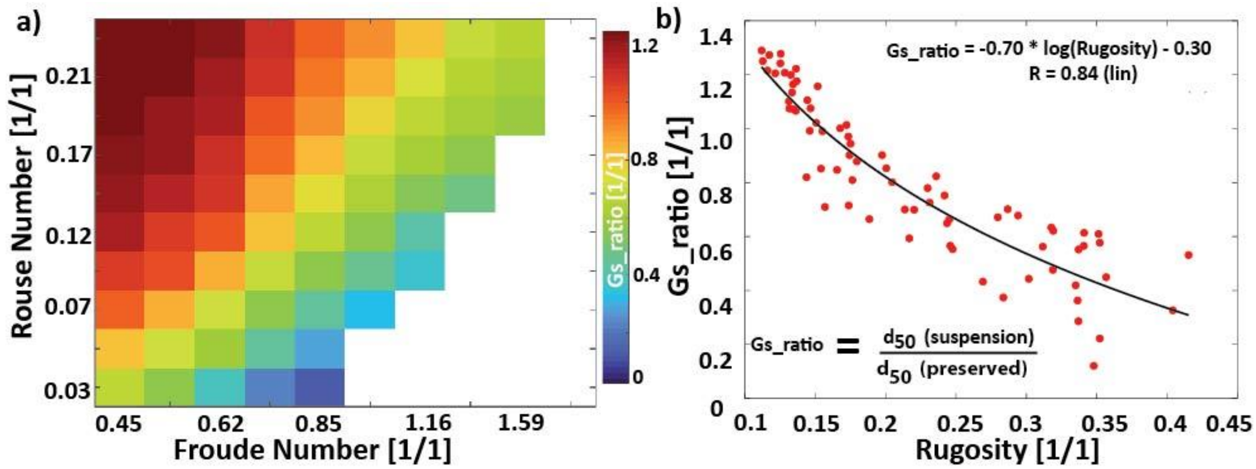

Figure 7 | Empirical relationship between ratio of median (d_{50}) grain size in transport at the inlet to median grain size preserved in the deposit and fan rugosity. a, Matrix shows grain size ratio (Gs_ratio) computed for all models with a significant deposit. b, A logarithmic trend is fit to the scatter plot of Gs_ratio and fan rugosity. This trend line allows for estimation of mean grain sizes in suspension for a given Fr_D and p value.

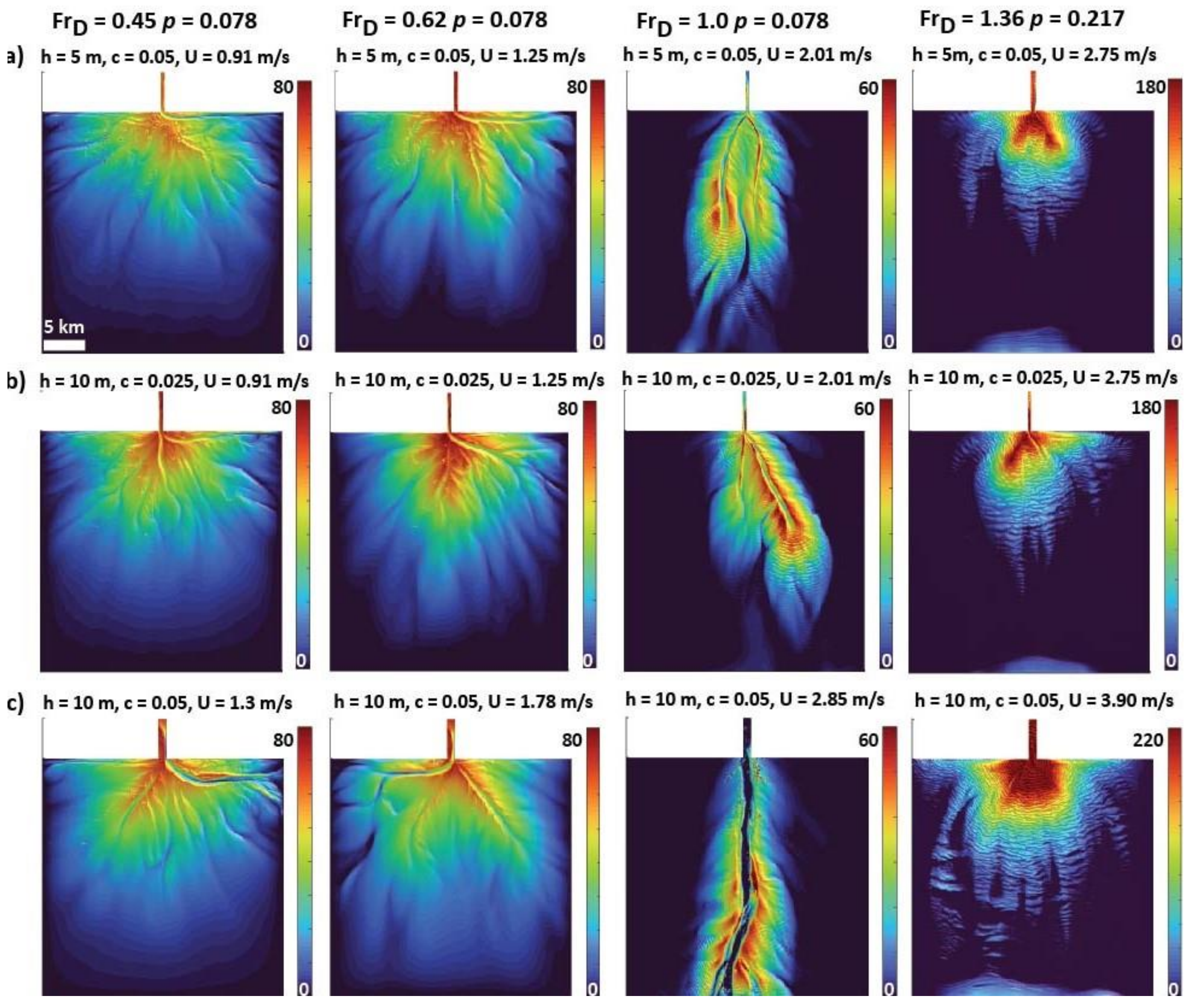

Figure 8 | Sensitivity of submarine fan shape to dimensional scales in Froude number (FrD) of the flow at the inlet. a, Simulated submarine fans in this row display our base case scenario where at the inlet we fix the height of the current (h) and volumetric concentration of suspended sediments (c). So by varying Froude number of the flow, we only vary the mean velocity (u) at the inlet. b, In this row, we show the resulting submarine fan morphology by doubling the height of the current (h) and reducing the concentration (c) by half to keep equivalent dimensionless value for FrD c, In this row, we increase the mean velocity (U) of the current at the inlet by proportionally increasing the height of the current (h) and concentration of suspended sediments (c). We show that while the precise morphology of the simulated fans changes as a result of the variation in the dimensional scales, the overall shape remains similar and shows strong dependence to unique dimensionless values of FrD and p of turbidity current at the inlet. All models have identical grid dimensions [35x30 km] and color bars denote thickness [m].

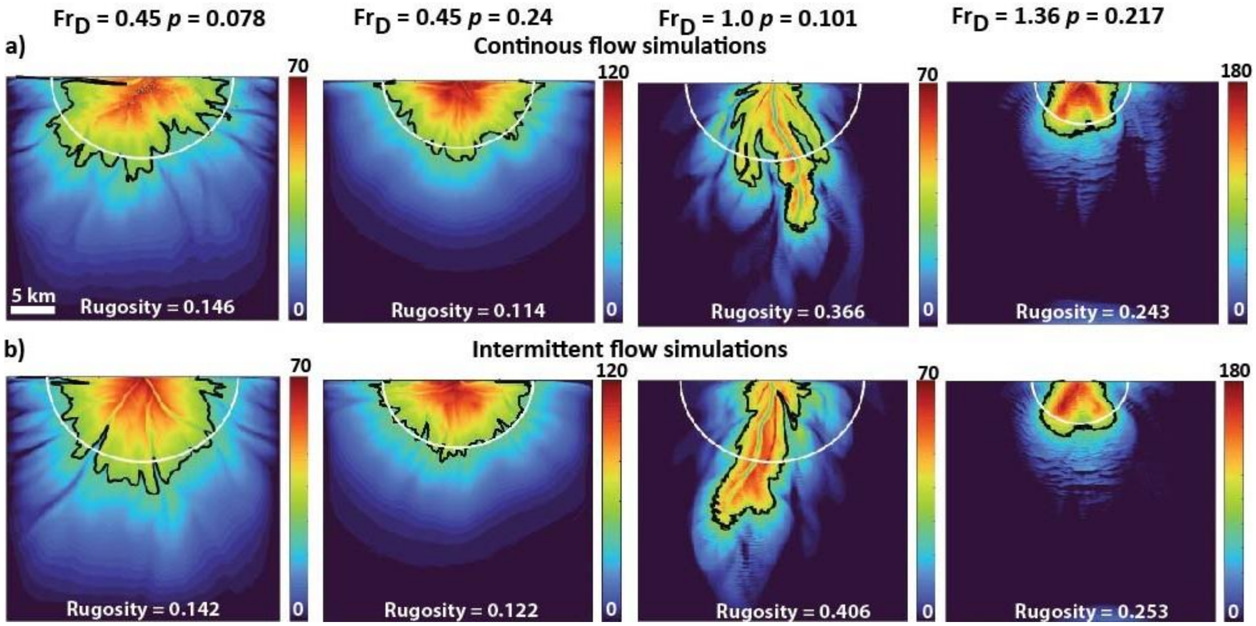

Figure 9 | Sensitivity of submarine shape to intermittent turbidity current flow. a, Simulated submarine fan morphologies from base case continuous flow conditions as a function of unique combinations of FrD and p. b, this row shows simulated submarine fans with intermittent flow conditions. The white semicircle defines a distance from the inlet upstream of which half of the sediments in the model domain are stored. The black contour is computed for a mean elevation along the semicircle. Color bars denote thickness [m]. Note that the relative to the base case simulation the absolute difference in measured rugosity ranges from 2% to at most 10%. Simulation domain is 30x30 km.

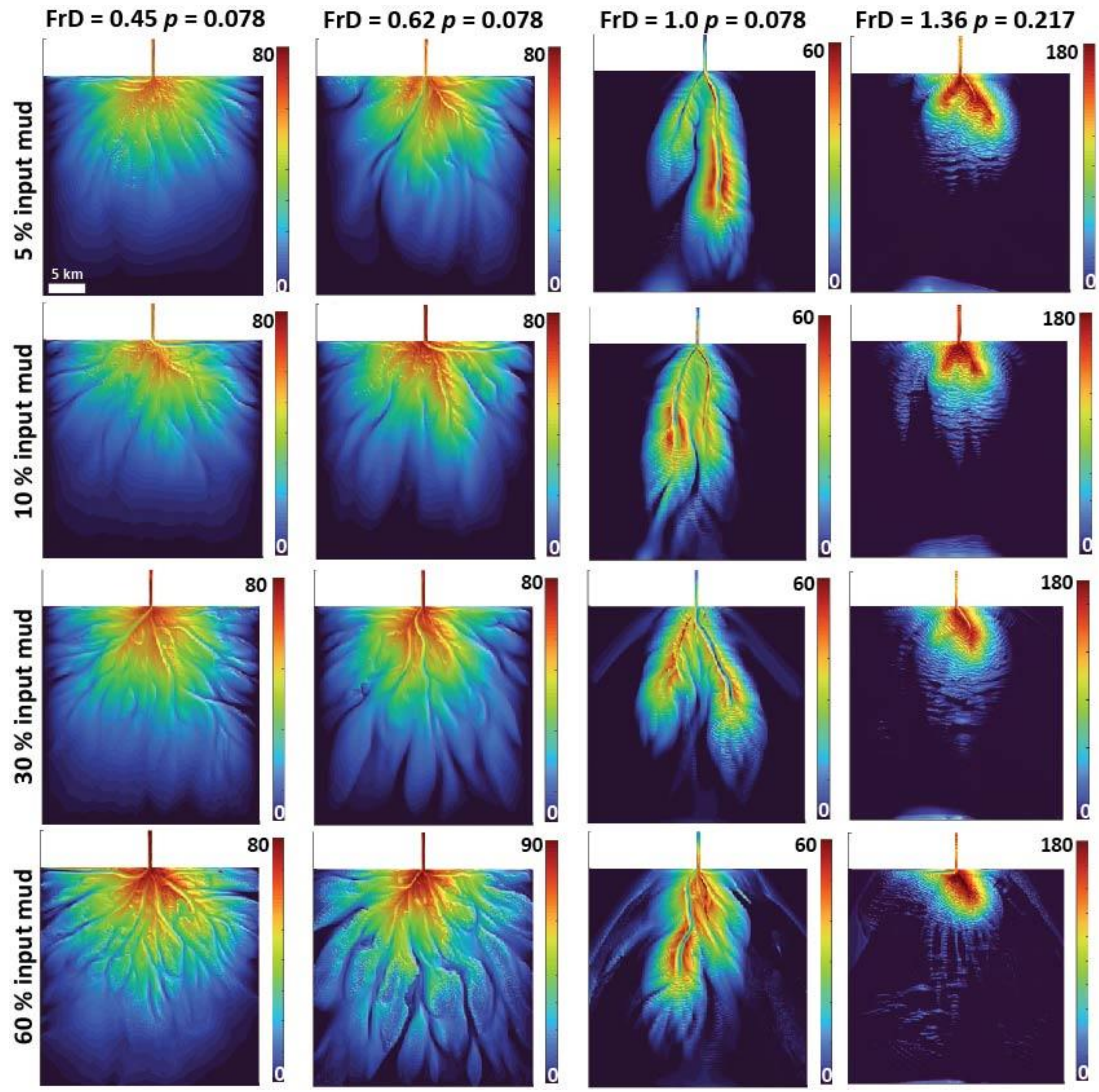

Figure 10 | Sensitivity of submarine shape to ranges in mud content. Matrix shows the influence of cohesion on the resulting fan morphology by increasing input mud content from 5 to 60% at the inlet for subset fans from the regime diagram. Note the final morphology in these models might be different i.e., placement of channels and lobes on the fan surface, however the overall shape remains similar. Color bar denotes the thickness of the fan at the end of the simulation.

Supplementary Materials

Case ID	Fr_D[1] [1/1]	p[2] [1/1]	Slope [degree]	U[3] [m/s]	u_*[4] [m/s]	D_{50}[5] [um]	Dmax[6] [um]	Sorting [1/1]	Ws[7] [m/s]	Duration[8] [hour]
1	0.46	0.032	0.065	0.9	0.06	24	463	1.8	0.0019	30210
3	0.63	0.032	0.136	1.3	0.08	25	645	2.0	0.0025	22088
6	1.00	0.032	0.460	2.0	0.13	23	1178	2.4	0.0041	13809
7	1.17	0.032	0.750	2.4	0.15	22	1497	2.6	0.0048	11807
9	1.60	0.032	2.080	3.2	0.20	17	2632	3.1	0.0065	8633
11	0.46	0.055	0.065	0.9	0.06	45	463	1.4	0.0032	30210
21	0.46	0.078	0.065	0.9	0.06	65	463	1.2	0.0050	30210
26	1.00	0.078	0.460	2.0	0.13	81	1178	1.7	0.0100	13809
31	0.46	0.101	0.065	0.9	0.06	83	463	1.1	0.0059	30210
33	0.63	0.101	0.136	1.3	0.08	94	645	1.2	0.0081	22088
36	1.00	0.101	0.460	2.0	0.13	109	1178	1.5	0.0129	13809
37	1.17	0.101	0.750	2.4	0.15	113	1497	1.6	0.0151	11807
39	1.60	0.101	2.080	3.2	0.20	114	2632	1.9	0.0206	8633
51	0.46	0.148	0.065	0.9	0.06	115	463	0.9	0.0086	30210
53	0.63	0.148	0.136	1.3	0.08	135	645	1.0	0.0117	22088
56	1.00	0.148	0.460	2.0	0.13	165	1178	1.2	0.0188	13809
57	1.17	0.148	0.750	2.4	0.15	175	1497	1.3	0.0220	11807
59	1.60	0.148	2.080	3.2	0.20	188	2632	1.6	0.0300	8633
71	0.46	0.194	0.065	0.9	0.06	145	463	0.7	0.0113	30210
73	0.63	0.194	0.136	1.3	0.08	172	645	0.8	0.0154	22088
76	1.00	0.194	0.460	2.0	0.13	219	1178	1.0	0.0247	13809
77	1.17	0.194	0.750	2.4	0.15	235	1497	1.1	0.0288	11807
79	1.60	0.194	2.080	3.2	0.20	265	2632	1.4	0.0394	8633
87	1.17	0.21	0.750	2.4	0.15	265	1497	1.1	0.0323	11807
88	1.37	0.21	1.232	2.75	0.17	284	1953	1.2	0.0377	12096
91	0.46	0.240	0.065	0.9	0.06	173	463	0.6	0.0140	30210
93	0.63	0.240	0.136	1.3	0.08	207	645	0.7	0.0191	22088
96	1.00	0.240	0.460	2.0	0.13	270	1178	0.9	0.0305	13809
97	1.17	0.240	0.750	2.4	0.15	294	1497	1.0	0.0357	11807
99	1.60	0.240	2.080	3.2	0.20	341	2632	1.3	0.0488	8633

[1]Densimetric Froude number; [2]Rouse number; [3]Mean inlet velocity; [4]Mean inlet shear velocity; [5]Mean sand diameter; [6]Maximum sand diameter; [7]Mean inlet settling velocity of suspended material; [8]Total simulation time on a super computer

Supplementary Table 1| Select model variables used in this study.

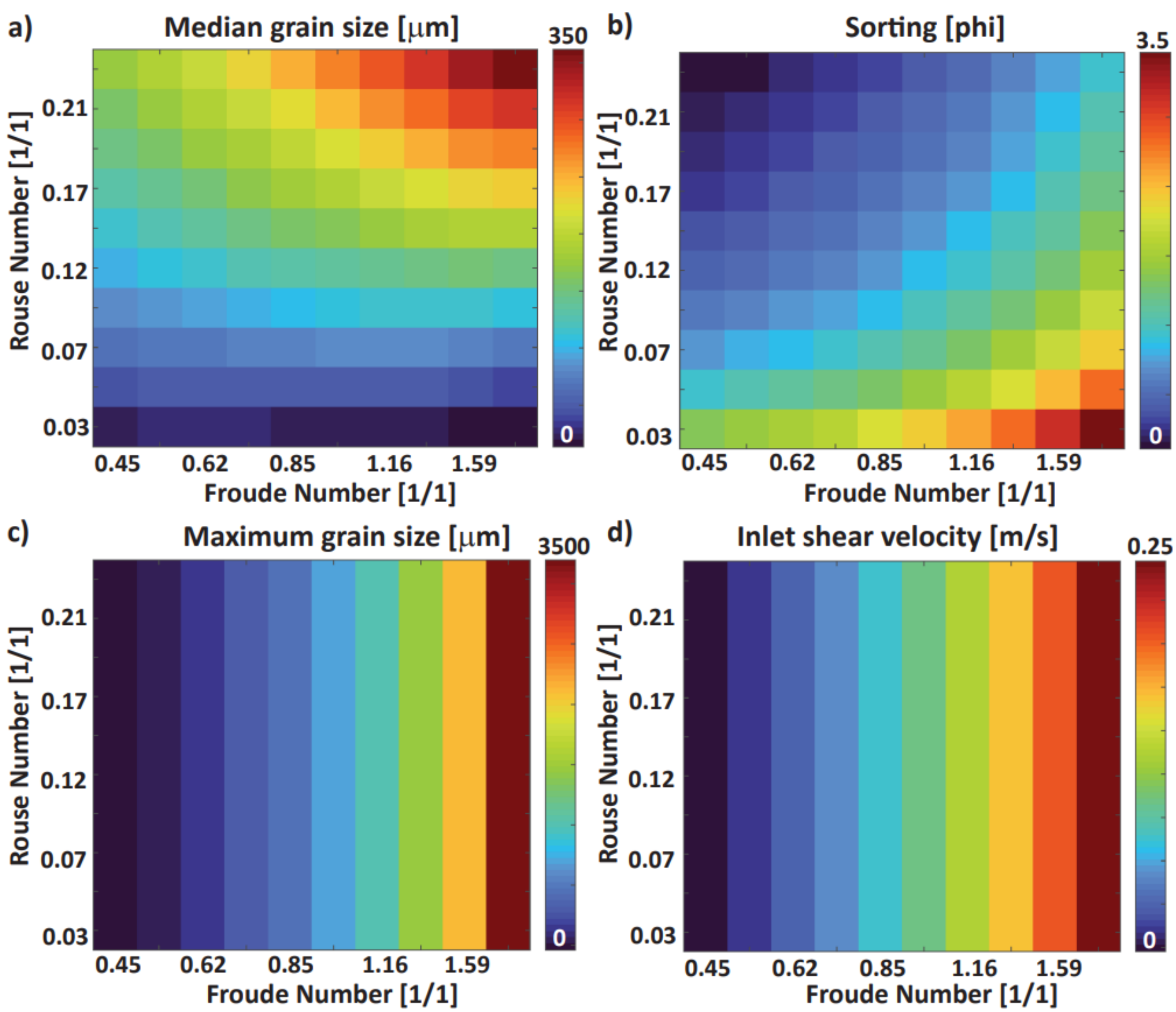

Supplementary Figure 1| Select parameters design for the dimensionless regime. a, Median grain sizes, b. Sorting, c, Maximum grain size, d, Inlet shear velocity.

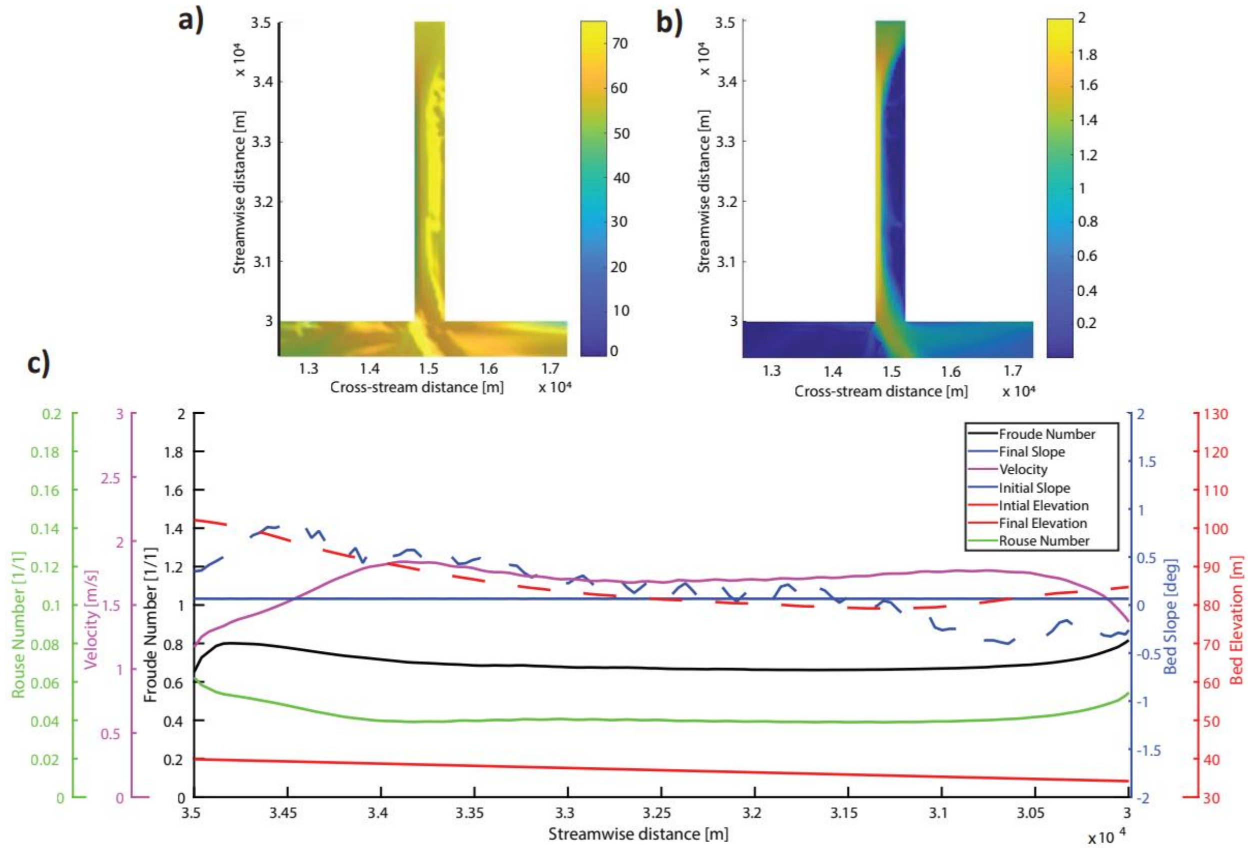

Supplementary Figure 2| Streamwise trends in flow hydraulics and bed surface properties within the inlet channel at the end of a Subcritical (Fr_D < 1) and low p simulation. a-b, Maps show deposit thickness and velocity magnitude within the active inlet channel. The inlet channel is 5km in streamwise and 500 m in cross-stream length. Flow starts at the inlet at 3.5 x 10^4 m. c, 1D plots of bed surface elevations, bed slopes, velocity magnitude, Rouse and Froude numbers are extracted from the active inlet channel shown in a&b. Further information on boundary conditions for this simulation are displayed adjacent to case ID 21 in supplementary Table 1.

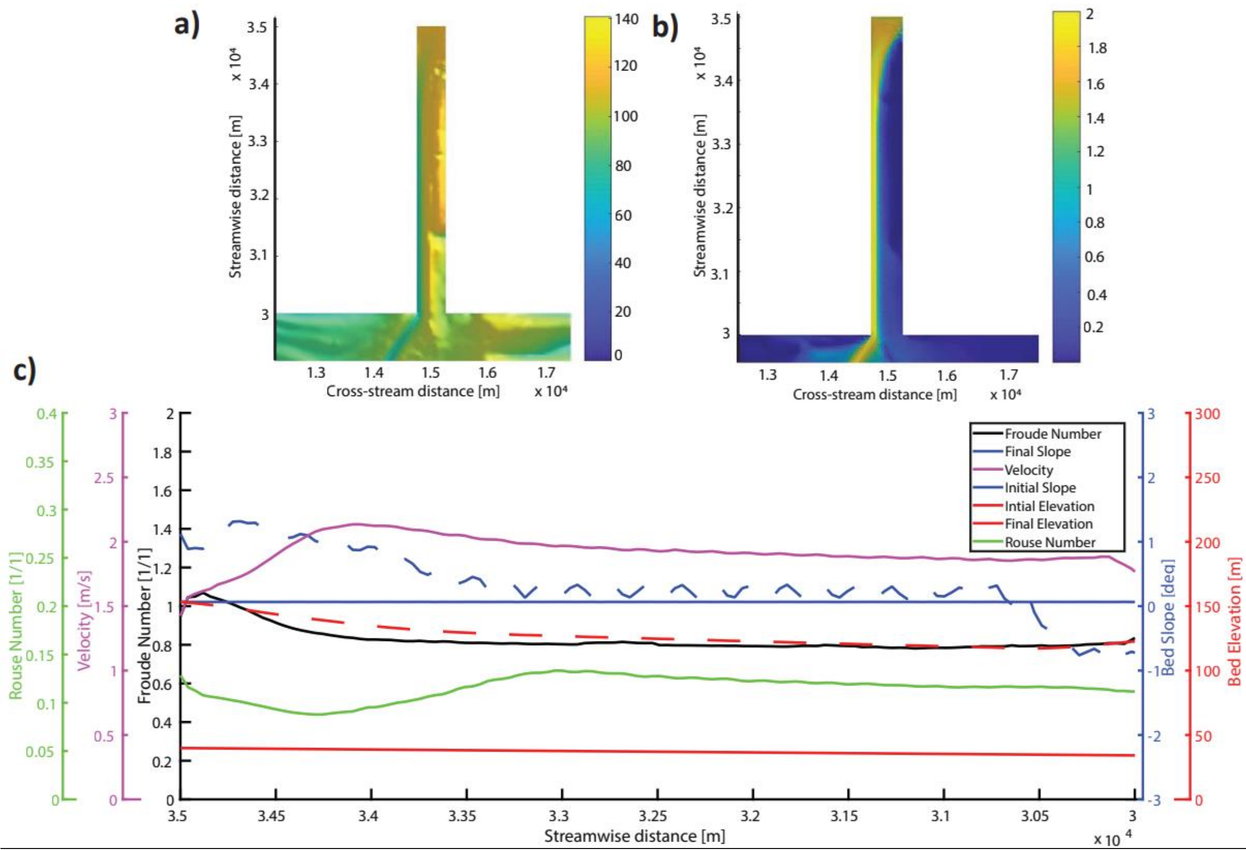

Supplementary Figure 3| Streamwise trends in flow hydraulics and bed surface properties within the inlet channel at the end of a Subcritical ($Fr_D < 1$) and high p simulation. a-b, Maps show deposit thickness and velocity magnitude within the active inlet channel. The inlet channel is 5km in streamwise and 500 m in cross-stream length. Flow starts at the inlet at 3.5 x 10^4 m. c, 1D plots of bed surface elevations, bed slopes, velocity magnitude, Rouse and Froude numbers are extracted from the active inlet channel shown in a&b. Further information on boundary conditions for this simulation are displayed adjacent to case ID 71 in supplementary Table 1.

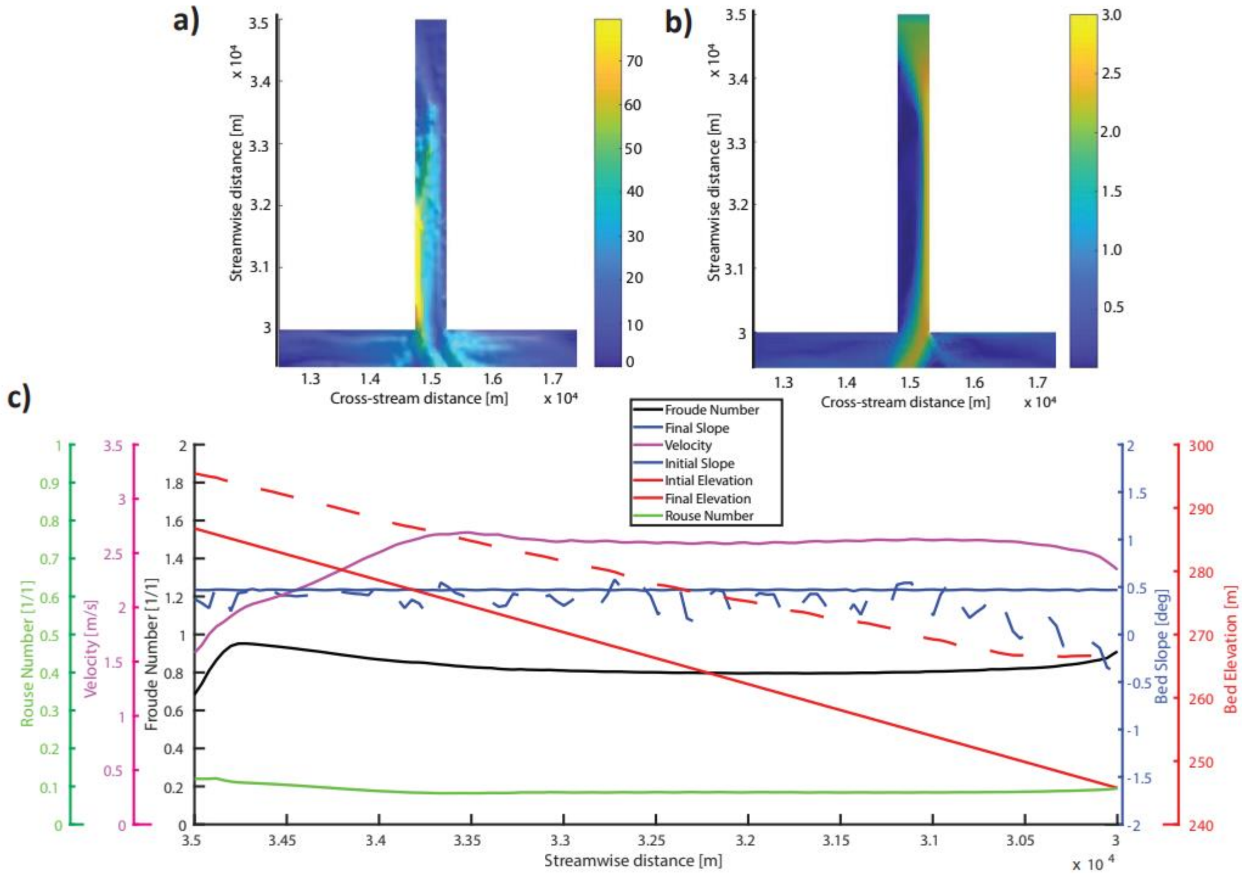

Supplementary Figure 4| Streamwise trends in flow hydraulics and bed surface properties within the inlet channel at the end of a Transcritical ($Fr_D \sim 1$) and low p simulation. a-b, Maps show deposit thickness and velocity magnitude within the active inlet channel. The inlet channel is 5km in streamwise and 500 m in cross-stream length. Flow starts at the inlet at 3.5 x 10^4 m. c, 1D plots of bed surface elevations, bed slopes, velocity magnitude, Rouse and Froude numbers are extracted from the active inlet channel shown in a&b. Further information on boundary conditions for this simulation are displayed adjacent to case ID 26 in supplementary Table 1.

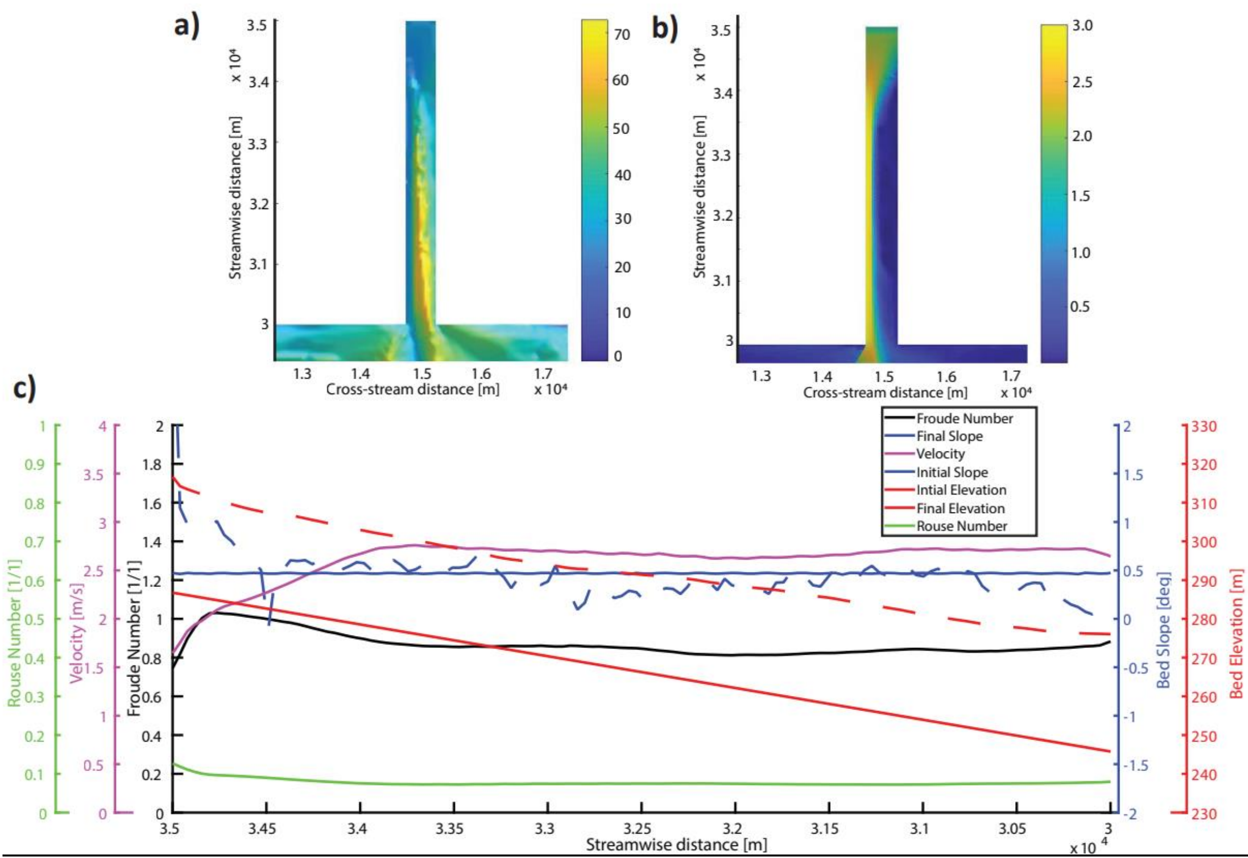

Supplementary Figure 5| Streamwise trends in flow hydraulics and bed surface properties within the inlet channel at the end of a Transcritical ($Fr_D \sim 1$) and relatively high p simulation. a-b, Maps show deposit thickness and velocity magnitude within the active inlet channel. The inlet channel is 5km in streamwise and 500 m in cross-stream length. Flow starts at the inlet at 3.5 x 10^4 m. c, 1D plots of bed surface elevations, bed slopes, velocity magnitude, Rouse and Froude numbers are extracted from the active inlet channel shown in a&b. Further information on boundary conditions for this simulation are displayed adjacent to case ID 36 in supplementary Table 1.

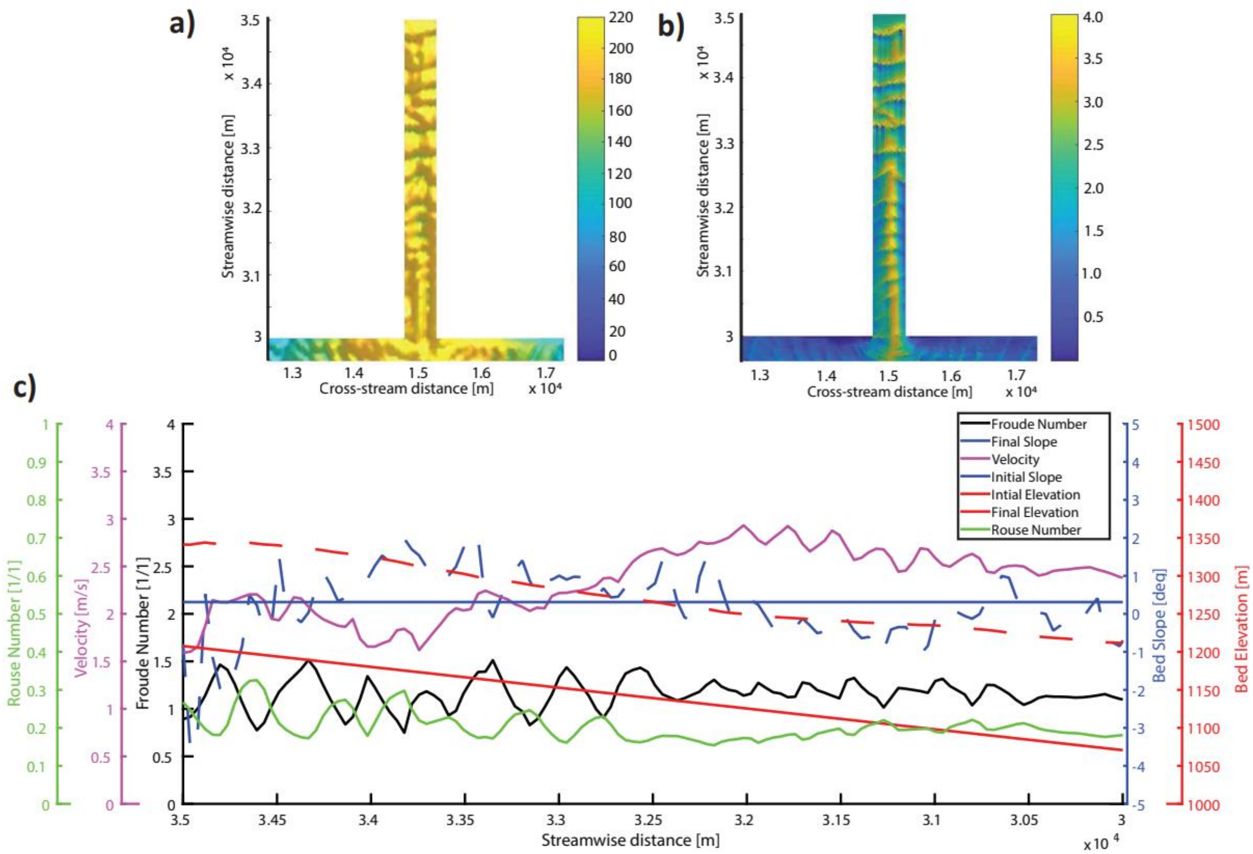

Supplementary Figure 6| Streamwise trends in flow hydraulics and bed surface properties within the inlet channel at the end of a Supercritical ($Fr_D > 1$) simulation. a-b, Maps show deposit thickness and velocity magnitude within the active inlet channel. The inlet channel is 5km in streamwise and 500 m in cross-stream length. Flow starts at the inlet at 3.5 x 10^4 m. c, 1D plots of bed surface elevations, bed slopes, velocity magnitude, Rouse and Froude numbers are extracted from the active inlet channel shown in a&b. Further information on boundary conditions for this simulation are displayed adjacent to case ID 99 in supplementary Table 1.

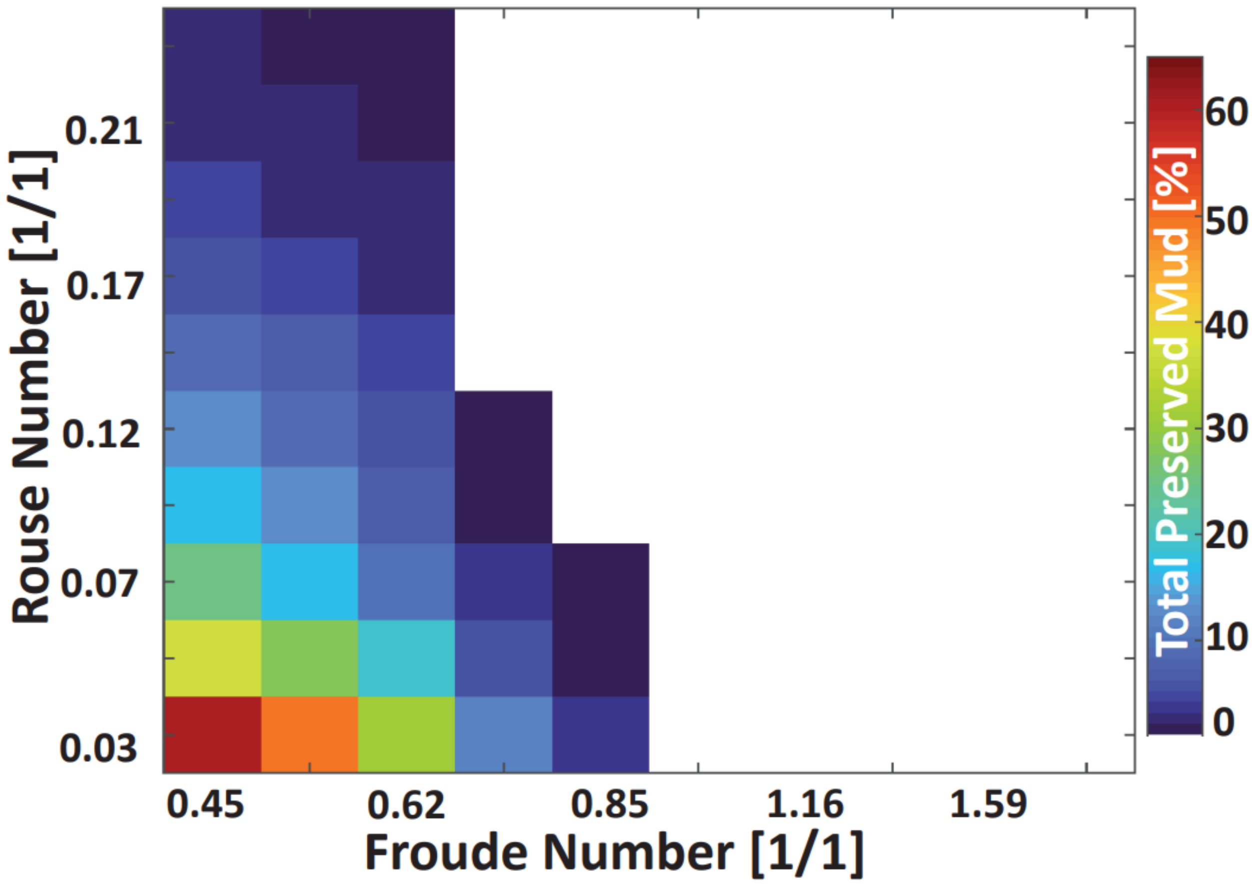

Supplementary Figure 7| Preservation of mud across the dimensionless regime. Matrix shows preservation of total mud content in all simulated submarine fans. The white region denotes models that are predominantly sandy and did not deposit any significant mud content.

CHAPTER 2: Leveraging a Process Based Numerical Model for Turbidity Currents and a Forward Seismic Workflow for Interpretation of Basin-Scale Stratigraphic Architecture in Submarine Fans.

Abdul Wahab[1]*, Gwladys Galliot[2*], Enru Liu[3], Mrugesh Shringarpure[3], David C. Hoyal[3], & Kyle M. Straub[1]

[1]Department of Earth and Environmental Science, Tulane University, New Orleans, LA 70118, USA.

[2]APA Corporation, Houston TX 77056-4400

[3]ExxonMobil Upstream Research Company, Houston, TX, 77389

Correspondence to: Abdul Wahab (**awahab@tulane.edu**)

Abstract

Outcrops, cores, well-logs, and seismic data generally provide a limited scope or vertical resolution for interpretation of submarine fan stratigraphic architecture. We leverage a depth-averaged numerical model for turbidity currents that generates realistic and plausible stratigraphic realizations for several modern submarine fans. We use modeled outcomes such as clay volumes and compacted porosities to generate elastic responses such as Vp, Vs, and ρ, followed by a 1D wavelet convolution to generate high-resolution synthetic seismic surveys for comparison of stratigraphic architecture to modern field counterparts through seismic facies analyses. We establish stratigraphic similarity between model-field examples and propose generalized and process-informed depositional models for endmember submarine fans. Results from this work aid subsurface stratigraphic architecture predictions and the interpretation of paleo-environmental conditions from low resolution seismic data of ancient fan deposits.

Introduction

Submarine fans are crafted by turbidity currents on continental slopes and abyssal plains in deepwater settings. The complex stratigraphic architecture of their deposits has motivated geoscientists for nearly a century to develop predictive techniques and depositional models for their preserved grain sizes, facies associations, and fan morphology (Kuenen and Migliorini 1950; Bouma 1962, Normark 1970; Mutti and Ricci 1978; Vail 1991; Clark et al., 1992; Richards et al., 1998; Stow and Mayal 2000; Posamentier and Walker 2006; Shanmugam 2016). These models and classification schemes help explain the character of submarine fan deposits in several basins but carry significant uncertainty. This is because prior efforts did not fully establish a link between submarine fans and their deposits to the fluid and sediment transport properties of the turbidity currents responsible for crafting these fans.

Turbidity currents move downslope due to their excess density relative to ambient lake or sea water from suspension of sediments (Bagnold 1962) and can travel 100's of km on the ocean floor (Talling et al., 2022). The fans constructed by these flows impact global climate through the transport and storage of organic carbon (Galy et al., 2007; Hage et al., 2022). Recently, the importance of these flows to subsea ecosystems, including threats to biodiversity from microplastics delivered to fans in deep oceans, were also identified (Kane et al., 2020; Pohl et al., 2020). Further, the stratigraphic architecture of their deposits hold clues to Earth's response to past episodes of climate change (Covault et al., 2010; Hessler and Fildani, 2019) and set the quality of massive geofluid reservoirs (Weimer and Pettingill, 2007). The prediction of submarine fan subsurface architecture remains a challenge to stratigraphers because we have relatively few measurements of the active flow processes that craft them and measurements we do have samples a relatively limited scope and duration of possible field scale flow conditions (Azpiroz-Zabala et al., 2017; Hughes Clarke 2016; Simmons et al., 2020; Pope et al., 2022;).

The best datasets available to explore the three-dimensional architecture of submarine fans come from reflection seismic surveys. While use of seismic surveys coupled to observations from cores and wireline logs have improved our understanding of fan architecture in several basins (Richard et al., 1998; Pirmez et al., 2000; Babonneau et al., 2010; Straub and Pyles, 2012; Jobe et al., 2017; Sweet et al., 2020), it is still challenging to link stratigraphic measurables to the processes that generated them. Even more challenging is using these attributes to guide development of theory that would allow us to predict stratigraphic attributes at sites lacking seismic surveys. This uncertainty is partially linked to the resolution of most seismic profiles (30-75 Hz), which is often tuned to aid visualization of targets at depths greater than 1 km (Prather et al., 2000; Stright et al., 2014; Nielson et al., 2017; Pimberton et al., 2018). These frequencies and common seismic velocities through deepwater strata result in relatively coarse vertical resolutions compared to scales of hierarchical stacking patterns (McHargue et al., 2011, Straub and Pyles, 2012). Coupled to this is a relative lack of physics-based numerical models that can generate stratigraphic architecture like what we observe in seismic surveys. Such models, if properly validated, would allow us to link forcing conditions to surface dynamics to stratigraphic architecture. Here, we demonstrate the use of a physics-based numerical model, EMstrata (Halsey et al., 2017; Wahab et al., 2022), with forcing conditions motivated by field observables. This model generates strata with similar architecture as observed in high resolution seismic surveys from end-member continental slope environments. The model stratigraphy is compared to field scale seismic surveys through use of the stratigraphic model outputs, such as porosity and shale volume, as inputs to a rock-physics and forward seismic workflow. Similar seismic architecture observed in our model-field comparisons then allows us to infer the turbidity current dynamics and surface processes likely responsible for crafting submarine fans.

We build on the work of Wahab et al. (2022) that linked submarine fan planform shape to dimensionless numbers that describe the fluid and sediment transport fields of turbidity currents. Here we link the surface processes that result from specific pairs of the dimensionless numbers to their resulting stratigraphic stacking patterns. This guides the development of generalized process-based depositional models that aid the prediction of stratigraphic architecture at sites that lack high resolution seismic profiles and improve our ability to invert stratigraphic architecture for paleo-environmental forcings.

A depth-average model for turbidity currents

Recent advances in computer processing speeds allow for the complex physics of turbidity currents to be solved in reasonable computational time with numerical models that produce strata from evolving surface processes. These models can now generate multiple realizations of stratigraphy from geological processes (Miller et al., 2008; Hawie et al., 2018; Wahab et al., 2022). Such forward models help bridge the gap between datasets that vary in dimensionality and resolution, as models store at high resolution the variables necessary to characterize lithostratigraphy. We leverage a forward and physics-based stratigraphic model, EMstrata, to produce stratigraphic realizations of submarine fans. Numerical experiments are forced with inlet flows whose fluid and sediment transport fields produce pairs of dimensionless parameters that are similar to a set of key modern field examples.

EMStrata is based on depth-average approximations of flow parameters in the Navier-Stokes equations of fully turbulent flows (Parker et al., 1986). The model's finite volume method solves governing equations for continuity of fluid mass, sediment mass, linear momentum, and turbulent kinetic energy. Further, any emerging discontinuity in turbidity currents, such as the dynamics found in the head of a current or due to hydraulic jumps are accounted for. In addition, the model solves for important sediment-transport parameters such as erosion and deposition of sediment, flocculation of mud particles, bedload fluxes, and influence of cohesion on the underlying deposits (see methods for additional details).

Prior work with EMstrata documents how the model produces realistic and fully dynamic submarine fan surfaces. Specifically, Wahab et al. (2022) simplified critical forcing parameters such as regional slopes and properties of sediments to show that two dimensionless parameters (densimetric Froude (Fr_D) and Rouse (p) numbers) critically influence the morphology of submarine fans. Fr_D measures the ratio of inertial to gravitational forces and p weighs the ratio of sediment settling velocity to shear velocity of the flow. This dimensionless framework highlighted endmember modern submarine fans that were likely constructed by subcritical ($Fr_D < 1$), transcritical ($Fr_D \sim 1$), and supercritical ($Fr_D > 1$) flows. Here, we compare seismic facies of three modern field examples to synthetic seismic facies obtained via forward seismic models of strata produced by EMStrata experiments that are forced with comparable flow conditions as their field counterparts.

Synthetic seismic surveys for end-member model runs

Synthetic seismic surveys from endmember models are constructed in several steps. First, a compaction model (Yang and Aplin, 2004) is used to compute porosity from clay volumes preserved in the synthetic strata. Next, a shale volume is computed from preserved grain sizes that are less than 62.5 um. We leverage a rock physics model to estimate elastic properties including compressional velocity (Vp), shear velocity (Vs), and density (ρ) from porosity and shale volumes in the synthetic strata (Xu and White, 1995; Xu and Payne, 2009). The elastic responses for the layered synthetic strata are then used to compute for reflection-coefficients. In the second step, an input wavelet is convolved with the reflection co-efficient series to generate synthetic seismic traces for the layered strata (Fig. 1) (see methods for further details) with frequency similar to their field counterpart mean peak frequency values. We then compare the seismic responses of our modeled fans to seismic surveys of three modern fans that sample endmember forcing conditions. Comparable seismic stratigraphy in field-model pairs gives confidence in linking observed stratigraphic stacking patterns to the surface dynamics responsible for constructing them.

Examples of modern submarine fans for comparisons to endmember models

There is an established relationship between the size and texture of submarine fans with their antecedent gradients (Haughton 2007). For example, in high gradient (slope >1^{o}) systems fans are generally small (< 10's of km), proximally thick, and predominantly sandy (i.e., Squamish (Vendettuoli et al., 2019) and Golo (Gervais et al., 2004; Sømme et al., 2011; Sweet et al., 2020) fans) (Fig. 2a). Fans that are formed on intermediate gradients (slope 0.5^{o}-1^{o}) are of intermediate size (up to 10's of km) and generally preserve a mixed fabric (i.e., Basin-IV of the Brazos trinity system (Prather et al., 2012) and Speculobe in Gulf of Cadiz (Habgood et al., 2003)) (fig. 2b). Finally, on low gradients (slopes < 0.5^{o}), fans are often quite large (~100's of km) and are predominantly composed of fine grain sizes (i.e., Zaire (Babonneau et al., 2010), Bengal (Galy et al., 2007), and Indus (McHargue and Webb, 1986) submarine fans) (Fig. 2c).

Due to uncertainties resulting from inversion of the fluid and sediment transport conditions of the field scale systems, we do not generate new models forced with the inverted turbidity current properties. Rather, we leverage existing model runs from the study of Wahab et al. (2022) that have similar pairs of Fr_D and p as measured and/or estimated dimensionless numbers from the field scale systems. Specifically, we make sure to compare Froude sub, trans, and super critical field fans to sub, trans, and super critical model fans, respectively. Inversion for Fr_D and p for field scale systems utilize data from available cores, regional slopes, and when possible measurements from active flows. We note from the study of Wahab et al. (2022) that small differences in Fr_D do not drive large differences in fan shape, so long as fans are correctly identified as either Froude sub, trans, or super critical.

<u>Golo Submarine Fan:</u>

For a high gradient system (Fig. 3), we explore the Golo submarine fan. This fan is a relatively small (~15 kms of streamwise length) and sandy deposit along the eastern Corsica margin in the Mediterranean Sea (Sweet at al., 2020). The shelf up-dip of this fan is narrow (~12 km wide) and its fluvio-deltaic plains are traversed by rivers that transport relatively coarse sand and gravel. The sediments are directly fed to short canyon heads and shelf-edge gullies during episodes of relative sea level fall that exceed ~40 meters (Somme et al., 2011). The most recent terminal lobe complexes were deposited on high gradients (~1°) (Deptuck et al., 2008; Somme et al., 2011; Sweet et al., 2020; Hamilton et al., 2017). The stratigraphic architecture of this lobe complex was imaged by a dense network of high resolution (mean peak frequency of ~300 HZ) 2D seismic surveys (spaced every 5-800 meters) and was directly sampled by sediment cores to depths below the seafloor up to 126 m. These cores were collected during the Sigolo surveys (Bruno, 2008).

We estimate a supercritical Fr_D of 1.75 for the Golo fan based on channel slopes and normal flow assumptions (Hamilton et al., 2017). From published core data, we estimated *p* to be ~0.110 based on a preserved median grain size of 178 um and estimates of shear velocity from knowledge of Fr_D. The model fan selected for comparison to the modern Golo fan has an inlet Fr_D equal to 1.17 and *p* equal to 0.21. The dimensional variables that result in these values include mean velocity (u = 2.4 m/s), current height (h = 5 m), concentration (c = 5%), and median grain size (D_{50} = 265 um). The slope (S = 0.75^{o}) is computed for the antecedent surface from the choice of Fr_D at the inlet. The simulation domain is scaled by a modified version of the advection length of median grain sizes in suspension (Wahab et al., 2022). The evolution of topography is solved on a triangular irregular grid with a median node spacing of 50 m. We neglect external boundary conditions such as sea-level fluctuations, subsidence, and tectonic forcings to explore the influence of flow forcing conditions and their emergent behaviors on the resulting submarine fan deposits.

Basin-IV Submarine Fan of the Brazos-Trinity System:

For an intermediate gradient field-model comparison, we select the upper Basin-IV fan of the Brazos-Trinity system (Fig. 4). This fan was deposited during the Quaternary in a Gulf of Mexico salt-withdraw minibasin, offshore of the Brazos and Trinity Rivers (Winker 1996; Badalini et al., 2000; Prather et al., 2012; Pirmez et al., 2012). The upper fan deposit in the terminal Basin-IV is 75 meters thick and measures 16 km in streamwise length and 8 km in strike. This system is imaged by a high resolution 3D seismic survey (mean peak frequency of ~200 HZ) and was sampled by a dense network of gravity piston cores (Prather et al., 2012). Bathymetric surveys show relatively steep gradients (~1^{o}) in the proximal part of the basin that transition to lower gradients (~< 0.5^{o}) in the basin center, followed by a gradient reversal resulting from subsurface salt dynamics. The stratigraphic architecture is characterized by submarine channel bodies bound by prominent levee deposits that extend into the basin before transitioning to lobes with several small distributary channel bodies (Fig. 4a).

Due to lack of modern turbidity current measurements in Basin-IV, we leverage a latent-hyper cube sample (Mckay et al., 1979) for important parameters such as flow velocity and current height and ran sensitivity analyses to match maps of fan thickness. We estimated input flows that had transcritical Fr_D of approximately 1.04, calculated with estimated flow mean velocity (u = 2.8 m/s), current height current (h = 9 m), and a reasonable concentration (c = 5%) of suspended sediments. From this choice of Fr_D we compute an antecedent slope, $S = \left((e_w + cd) * Fr_D^2 + 0.5 * e_w\right)$, as a function of clear water entrainment e_w (Parker and Garcia, 1987) and an estimate of the coefficient of friction of the bed, cd. The estimated slope for this model is 0.46^0. Similarly, we estimate p as 0.24 based on measurements of preserved grain sizes (D_{50} = 200 um) from core data and estimation of shear velocity from the estimated Fr_D and an estimate of Cd.

Modern Zaire Submarine Fan:

For a low gradient system, we select the modern Zaire fan (Fig. 5), which is mature and large (>1000 km in streamwise direction) in scale. The fan developed on the continental slope and the basin floor of the West African passive margin with perennial sediment input from the Congo River. A modern deepwater sinuous channel that is hundreds of kilometers long feeds terminal lobes and is directly linked to the Congo River via a deeply incised submarine canyon (Savoye et al., 2009; Babonneau et al., 2010). Numerous abandoned channels on this fan system indicate a long history of progradational growth from the slope to the abyssal plain. The most recent and distal terminal lobe complexes developed on a low gradient (about 0.05°) basin floor (Babonneau et al., 2010). The stratigraphic architecture of the modern Zaire lobe complex is imaged by a high resolution (mean peak frequency of ~120 HZ) seismic survey comprised of tightly spaced 2D lines and accompanying piston cores which were acquired during the ZaiAngo surveys in the early 2000s (Babonneau et al., 2010). This architecture is characterized by lobes and lobe complexes that prograde into the basin (Bonnel 2005). The central portion of these lobe complexes are dominated by distributary channel bodies filled with sands, while silt and muddy sediments are preserved on distal parts of the lobes (Fig. 5a).

We estimate Fr_D for flows that crafted the Zaire fan to be 0.13-0.21 from published measurements of modern flows (Azpiroz-Zabala et al., 2017; Simmons et al., 2020). Similarly, we estimated p to be 0.0035-0.0057 based on published grain size data and estimation of shear velocity from the estimated Fr_D and an estimate of Cd (see methods). We compare the seismic facies from the modern Zaire fan to a subcritical model (Fr_D = 0.45) with p = 0.078. This initial surface is non-erodible and has a slope of 0.065°, which is estimated Fr_D as function of e_w and cd. Dimensional variables such as height of the current (h = 5 m), average current velocity (u=0.91 m/s), concentration of suspended sediments (c = 5%), specific gravity (R = 1.65), and gravitational acceleration (g = 9.8 m/s^2) set the Fr_D value at the inlet of the simulation domain. Similarly, p is set by median grain sizes (D_{50} = 200 um) in suspension via the sediment settling velocity and shear velocity (u_* = 0.06 m/s^2) of the flow. The resulting fan shape and texture of the deposit share similarities with the modern Zaire lobe complex (Fig, 5b).

Results

Seismic stratigraphy, including derivative measurements such as reflection termination patterns and geometries aid interpretation of subsurface lithology. We analyze seismic facies, which are reflection groups resulting from distinct rock properties relative to adjacent strata (Mitchum 1977) from three modern submarine fans. We compare these seismic facies to synthetic seismograms generated from model runs that are forced with comparable dimensionless parameters (i.e., Fr_D and p, see methods) and modeled with similar mean peak frequencies. We use this comparison to establish stratigraphic similarity between field examples and counterpart numerical experiments. This allows us to use the temporal evolution of the models to describe likely flow processes and depositional mechanisms responsible for crafting the observed stratigraphic patterns.

High gradient field-model comparison

In dip, seismic reflectors from the Golo fan show abundant lobe shaped (convex up) geometries that compensationally stack in the proximal fan (Fig. 6a). In strike, we observe seismic reflectors that are parallel to subparallel and display onlapping geometries against the antecedent slope (Fig. 6c). These geometries are overlain by seismic reflectors that downlap against the antecedent slope. These seismic facies suggest an early retrogradation phase that is followed by fan progradation. We observe a similar stacking pattern in the synthetic seismic data for the counterpart submarine fan model (Fig. 6b, 6d).

The evolution of the flow field and morphology of the supercritical fan is characterized by flow in low sinuosity channels. At the channel to lobe transition the flow frequently undergoes a hydraulic jump, were cyclic steps form as result of increased flow height and turbulence loss. Bedforms migrate upstream on the fan surface and within the channel which results in loss of flow confinement, which eventually triggers an avulsion. We note that the fan is predominantly sandy because of high shear stresses on the fan surface and within the channels that prohibits deposition of silt and mud (Fig.3b). There is no flux partitioning at the channel to lobe transition and the channel network at the time of avulsion is commonly characterized by a single channel. These morphodynamics limit channel extension and progradation of the fan, resulting in short, but thick submarine fans that are sandy.

Intermediate gradient field-model comparison

In dip sections, the Basin-IV fan has distinct seismic facies that onlap the antecedent depositional surface (Fig. 7a). Onlap geometry suggests an early stage of retrogradation, before progradation commenced. The seismic reflectors above the backstepping units show parallel to subparallel reflectors that downlap on the antecedent surface with a geometry that indicates fan progradation (Fig. 7a). In contrast to the field example, we note that our model fan only contains evidence of progradation via downlapping seismic facies in the dip direction (Fig. 7b). This difference might be due to the initial surface on which the numerical experimental fan grew, which had a constant down-basin slope, in contrast to the bowl like geometry of the basin IV antecedent slope. In strike, the Basin-IV seismic stratigraphy has several reflection terminations with concave up geometries and erosional bases that indicate channel bodies (Fig. 7c). The reflectors adjacent to interpreted channel bodies are concave up and divergent on both sides indicating the preservation of well-developed levees. Maps of deposit thickness and net-to-gross (1- fraction of grains that are less than 62.5 um) in Basin-IV fan indicate that channel bodies mainly preserve sand, whereas silt and mud are deposited on distal levees and lobes (Fig. 4). We observe similar concave-up geometries and adjacent downlapping reflectors from strata constructed by well-developed channel-levee complexes in strike sections of the submarine fan numerical experiment (Fig. 7d).

The evolution of the transcritical submarine fan model is characterized by self-formed low sinuosity channels that extend in the primary flow direction (Fig. 4b). The channels develop prominent levees, which help maintain bypass conditions for most of the flow simulation. Channels avulse infrequently, but at a variety of locations on the fan surface. This results in proximal stratigraphy with clusters of channel bodies.

Low gradient field-model comparison

Proximal portions of a seismic dip line from the modern Zaire fan have reflection terminations that are subparallel to discontinuous (Fig. 8a). Several reflectors have concave up geometries, where the base of the reflectors truncate underlying reflectors. These types of concave up reflection packages that truncate other reflectors indicate an erosional surface at the base of a channel body (Fig. 8a). Further downstream on the dip line, concave up reflectors decrease in number and the seismic facies transition into sigmoidal and downlapping seismic geometries. These geometries generally indicate paleo-progradation of a sedimentary package into the basin (Fig. 8a). Here the lack of concave up reflectors, compared to proximal regions, indicate a channel to lobe transition. Further downstream on the dip line the reflectors become sub-parallel, suggesting relatively uniform sedimentation from suspension fallout. This type of seismic facies implies an overall progradation of the submarine fan into the basin with downstream grain size fining. A similar facies trend is observed in a series of strike transects. Here we highlight a proximal transect, where more clustered concave up geometries indicate frequent channelization of the proximal fan (Fig. 8c). The concave up geometries are adjacent to relatively diverging and downward thinning reflectors that downlap, indicative of prominent levees. The synthetic seismic facies from the modeled submarine fan shows similar seismic facies along dip and strike directions (Fig. 8b, 8d), suggesting that the Zaire modern fan was crafted by a similar set of processes.

The stratigraphy of the low gradient submarine fan model was built by several channel-levee networks that fluctuated between one to several active channels. This generated a distributive network due to channels that avulsed at a variety of downstream locations (Fig. 5b). This distributive pattern is hierarchical and partitions the flux of sediments and water moving over the fan surface. This flux partitioning is variable and leads to a complex growth of the fan. Sand is mainly transported and preserved in the channels, while silt and muds are deposited on levees, distal lobes and outer parts of the fan. Overall, this type of fan grows through several episodes of basin-ward progradation.

Discussion

Numerical models of submarine fans that produce comparable stratigraphic architecture as imaged in the shallow subsurface of modern fans, when forced with comparable input flows, lends credibility for their use in examination of the processes that build fan strata. These models help bridge the gap between the scales and dimensions of data typically available for interpretation of submarine fan strata. Upon establishing stratigraphic similarity via high-resolution seismic surveys, the knowledge of the temporal model evolution allows one to link stratigraphic architecture to the suite of flow dynamics and surface processes that construct fans. This linked framework opens a potential for improving our generalized and process-informed depositional models for endmember submarine fans (Fig. 9). Ultimately, this will aid in prediction of subsurface architecture and inversion of submarine fan strata for paleo-surface processes and environmental forcings.

Depositional model for a high gradient fan system

We develop a process-informed depositional model for submarine fans that form on high gradients with the temporal evolution of our high gradient numerical model. This depositional model is characterized by a fixed feeder channel that evolves from a gully-type erosional feature on a continental margin (Deptuck and Sylvester 2018) (Fig. 9a). The resulting fan is constructed by single-channel networks that are relatively short, have low-sinuosity, and rapidly loses confinement near their terminus. The fan grows through a series of progradational and retrogradational events (Fig. 9 a). Channels undergo frequent avulsions, which delivers sediments to many proximal locations on the fan surface. This morphodynamic behavior generates a thick sandy fan with an overall radial morphology that does not prograde far into a basin (Fig. 9a). This system also produces characteristic bedforms, including cyclic steps and antidunes near the channel-lobe transition and on levees (Fildani et al., 2006). The high gradients facilitate transport and deposition of coarse particles, resulting in a fan that is predominantly sandy.

Depositional model for an intermediate gradient fan system

The process-informed depositional model for an intermediate gradient submarine fan includes low-sinuosity channels that can prograde into basins (Fig. 9b). The channels are bound by prominent levees that help maintain bypass conditions. The channels avulse infrequently, and newly formed channels continue to prograde in the primary downstream flow direction, which produces an elliptical fan morphology. The well-formed channel-levee system facilitates fan growth through several phases of progradation (Baldani et al., 2000). As a result, the fan deposit undergoes frequent erosion and reworking by channels that are bypassing during these progradational phases. This type of fan preserves sand in channels and lobes whereas silt and mud are deposited on distal levees and lobes.

Depositional model for a low gradient fan system

The process-informed depositional model for submarine fans that form on low gradients include feeder channels linked to long-established terrestrial drainage systems that are connected to oceanic basins by a point source. An example might be a river that delivers sediment directly to a submarine canyon incised into the shelf (Bonnel 2005; Savoye et al., 2009; Babonneau et al., 2010; Jobe et al., 2011; Paul et al., 2013; Fildani 2017; Fisher et al., 2021) (Fig. 9c). The fan is constructed by multiple long-lived high-sinuosity and meandering channels. Channel networks fluctuate between one-to-many channel networks throughout the fan growth. The channels bifurcate at a range of distances downstream of the main feeder channel (Flood et al., 1991), which partitions the flux of sediment and water moving through the growing distributive network. This portioning of fluxes is variable and leads to the formation of asymmetric channel branches and spatial variability to the supply of sediment to the fan surface. The multi-channel network facilitates fan progradation along many axes, producing a more radial fan. However, while the number of active channels on the fan surface increases with a drop in slope gradient, channels are stable resulting in relatively jagged contours along the front of these fans (Wahab et al., 2022). The low gradient of these systems does not facilitate easy transport of sand, except where flows are relatively thick along the thalweg of channels. As a result, sand is mainly transported in channels, whereas silt and mud size particles are deposited on the levees, lobes, and distal fringes of the fan.

Gradient control over submarine fan growth

Turbidity currents move large volumes of sediment on Earth, especially when they are linked to well established and large continental drainage systems (Galy et al., 2007; Talling et al., 2022). In general, observations suggest that deposition from turbidity currents reduces the gradient of continental slopes over geological time (Prather 2003; Pyles et al. 2011). For example, the longest-lived submarine fans are also the lowest gradient fans (i.e., Zaire fan, Indus, and Bengal fan (Babonneau et al., 2010; Kolla and Coumes 1987; Spie 2009). Fan forming flows adjust to the emergent depositional gradient of the slope, resulting in deposits that have measurable gradients in grain size or stratigraphic architecture moving up section. This suggests that mature and large-scale submarine fans can be explained by combining the proposed fan models over several phases of fan growth (Fig. 10).

The evolution of a large-scale submarine fan, like the Zaire fan, likely starts with the inception of channels from erosional gullies on high continental gradients (Deptuck and Sylvester 2018). These channels are fed by linked fluvio-deltaic systems where supercritical flows develop and transport sediments. The end of channels has small mouth bar deposits or small lobes where characteristic supercritical bedforms form, including antidunes and cyclic steps due to hydraulic jump conditions. The mud is deposited further downslope as sediment blankets on the distal fringes of mouth bars or lobes, where flow velocity significantly drops aiding settling of silt and mud size sediments. Larger channel-levee systems develop as the fan growth continues. Deposition resulting from these larger channel-levee systems further reduces the depositional gradient and results in development of highly sinuous submarine channels (Peakall et al., 2000; Wynn et al., 2007). Processes that drive fan growth during this phase shift towards those linked to low gradients, with a key result being the development of numerous distributary channels. With time, a mature submarine canyon develops through continuous incision of the upper shelf (Ferry et al., 2004; Babonneau et al., 2010). The submarine canyon feeds large distributive channel-levee networks, delivering sediment to the abyssal plains. Sand accumulates mostly in channels and on proximal levees, whereas silts and muds are deposited on distal levees, distal lobes, and outer parts of the fan front. Here big levees will aggrade as meandering channels grow on top of earlier terminal lobes deposits, and occasionally a nodal avulsion locally increases the gradient, which can for a short time alter the morphodynamics to those characteristics of steeper (and older) systems (Kolla 2007).

The above growth trajectory characterizes a passive margin system. However, tectonic uplift or subsidence can accelerate or reverse the temporal evolution of submarine fans by altering bathymetric gradients. For example, the Golo fan has not transitioned into a largescale distributive system with time due to high bathymetric gradients sustained by active tectonics and a relatively smaller sediment routing system (Sømme et al., 2011; Sweet et al., 2020). Similarly, in the case of Golo, external factors such as enhanced sediment supply through a single and fixed-point source can also accelerate this fan growth (Covault and Graham 2010; Ferguson et al., 2020).

Our approach can be used to aid prediction of stratigraphic architecture for deep time deposits located at great depths, including those that house hydrocarbon reservoirs or that might be used for CO_2 sequestration. To accomplish this, several optimization steps are needed. These include high confidence estimates of flow conditions that feed submarine fans, use of appropriate antecedent surfaces extracted from seismic data, a rock physics model that is calibrated with depth for compaction and fluid saturations, and a more realistic wavelet scaler to match target seismic amplitudes. Additionally, a model that can account for deposition of hemipelagic fallouts during punctuated flow events is needed. Hemiplegic fallouts generally drape the sandy deposits (Figure 6 a&c) and provides a change in impedance contrast, which we are not able to achieve in this study. High resolution synthetic seismic surveys from this approach could help the interpretation of stratigraphic architecture that is below seismic tunning at these depths.

Summary and wider implications

Submarine fans are the ultimate sink in sediment routing systems and their complex growth and stratigraphic architecture have been rigorously studied for nearly a century. We show that synthetic seismograms generated from stratigraphy that is an output of a process based numerical model contain similar seismic facies as observed in modern submarine fans. This supports use of the numerical model for exploration of likely surface processes responsible for their growth. This information is used to develop process-based models for the growth of submarine fans, which distill key characteristic observations from the numerical models. The primary variable that controls the stratigraphic architecture of our numerical experiments, and thus our process-based models, is the depositional slope. This linked framework has implications beyond the interpretation of stratigraphic architecture on seismic data. For example, this framework aids inversion of ancient submarine fan deposits for paleo-environmental conditions, which will aid the interpretation of climatic change signals housed in their strata across geological time.

Materials and methods

Seismic data analyses

We leverage cores, well logs, and 2D and 3D seismic surveys for grain sizes, paleo-channel depths, detailed mapping of stratigraphic surfaces, seismic facies, and stacking patterns. This data was imported to a Petrel® digital workspace to compute for and produce maps of fan thickness and net-to-gross (fraction of strata in a deposit with median grain size equal to or larger than sand, 62 mm). We used standard interpolation (kriging) methods in Petrel to produce deposit thickness and net-to-gross estimates in areas where well log and cores were sparse.

Selection criterion of comparison of field examples to numerical models of submarine fans

We estimated the Fr_D and p for field examples using published data on turbidity current flow properties and sediment-transport parameters. We then compared these field examples to numerical models of submarine fans that are forced with similar Fr_D and p at the inlet to model domains. For the Zaire fan example, we estimated the Fr_D to be between 0.13 – 0.21 based on average sediment concentrations of 2% (Azpiroz-Zabala et al., 2017), an average flow height of 64 m in the proximal canyon-fan transition area, and measurements of mean flow velocities of 0.6-1.0 m/s (Simmons et al 2020). We estimate p to be 0.0035-0.0057 by computing a settling velocity of 8.62×10^{-5} m/s using the Dietrich formulation (Dietrich, 1982) and median grain size of 12 um. The shear velocity is estimated as between 0.037-0.063 m/s by assuming a drag co-efficient of 0.004 (Parker et al., 1986). These Fr_D and p guided our selection of a numerical model that is similarly forced with a subcritical Fr_D = 0.45 and p= 0.078. We acknowledge that our approximations of Fr_D and p for the Zaire system are estimates based on limited active turbidity current flow data.

We estimated the Fr_D to be 1.05 for the upper fan in Basin IV of the Brazos-Trinity system. Here, we highlight that there are no measurements of active flows for this system. So, we leverage a latent-hyper cube sampling technique (McKay et al., 2000) to estimate flow velocity and ran several sensitivity analyses to reasonably match Basin IV stratigraphic attributes such as thickness. From this we estimate a velocity of 2.8 m/s, current height of 9 m, and a reasonable sediment concentration choice of 5% (Simmons et al., 2020). We estimate a p = 0.24 based on median grain sizes of 200 um from propriety sediment core data (ExxonMobil internal report). We compare this to a submarine fan model with a Fr_D = 1.0 and p = 0.124.

For the sandy Golo submarine fan, we estimate an average Fr_D = 1.75 based on data of channel slopes and normal flow assumptions (Hamilton et al., 2017). From published core data, we estimated p to be 0.110 based on a preserved median grain size of 178 um and estimates of shear velocity from knowledge of Fr_D (ExxonMobil Internal report). The model selected for comparison to the modern Golo fan has an inlet Fr_D of 1.36 and p equal to 0.170. We acknowledge that the Fr_D and p of our model are not an exact match to the field counterparts. Here our goal was to explore general stratigraphic attributes resulting from a super critical fan, rather than aiming for a simulation of the exact conditions at each site (Wahab et al., 2022).

Numerical model

We leverage a depth-average model for turbidity currents that solves for four conservation equations (Parker et al., 1986), bedload fluxes (Peter and Müller, 1948), erosion rates (Garcia and Parker, 1991), deposition rates (Garcia 1994), flocculation of clay particles (Kuprenas et al., 2018, Winterwerp 1998), and the influence of cohesion on the underlying deposits

(Winterwerp and Kesteren 2004). A more detailed description of the depth-averaged theory, governing equations and analyses of their approximate analytical solutions, choice of the numerical solver, experimental design and boundary conditions is published in prior studies (Halsey et al., 2017, Halsey and Kumar 2019, Wahab et al., 2022).

Forward seismic modeling

We generated synthetic seismograms of strata from select submarine fan models and compare these to modern field counterparts. First, we compute for porosity from volume of clay particles using a compaction model (Yang and Aplin 2004) and shale volumes from the preserved grain size distributions in the synthetic stratigraphy. Next, we use a rock physics model to compute for elastic responses, such as bulk density (rho), compressional velocities (vp), shear wave velocities (Vs) from the above-mentioned inputs. The rock physics model utilized here is based on the published Xu-White formulations (Xu and White, 1995; Xu and Payne, 2009), which computes the elastic parameters, including P- (V_p), S- (V_s) velocities and density. The Xu-White model is implemented in three main steps (see Figure 1): (1) mixing minerals using the average of the Hashin-Shtrikman or Voig-Ruess bounds (Mavko et al., 2009); (2) adding porosity using the differential effective medium theory (Kuster and Toksoz 1974); and (3) adding fluids using the Gassmann theory (Gassmann 1951). Elastic parameters are dependent on outputs that characterize the modeled geological strata, including compacted porosity, net to gross, and volume of clay (Vclay). Next, a 1D convolution model is used to compute synthetic seismograms by convolving reflection coefficients and a zero-phase Ricker wavelet with mean peak frequencies of the targeted examples. For near or normal incidence, the reflection coefficient is calculated as the ratio of the difference of the product of velocity and bulk density to the sum of the product of velocity and bulk density across interfaces. For non-zero incidence, approximate expressions for the reflection coefficients are used (Aki and Richards, 2002).

References cited

Azpiroz-Zabala, M., Cartigny, M. J., Talling, P. J., Parsons, D. R., Sumner, E. J., Clare, M. A., ... & Pope, E. L. (2017). Newly recognized turbidity current structure can explain prolonged flushing of submarine canyons. *Science advances*, *3*(10), e1700200.

Babonneau, N., Savoye, B., Cremer, M., & Bez, M. (2010). Sedimentary architecture in meanders of a submarine channel: detailed study of the present Congo turbidite channel (Zaiango project). *Journal of Sedimentary Research*, *80*(10), 852-866.

Babonneau, N., Savoye, B., Cremer, M., & Klein, B. (2002). Morphology and architecture of the present canyon and channel system of the Zaire deep-sea fan. Marine and Petroleum Geology, 19(4), 445-467.

Badalini, G., Kneller, B., & Winker, C. D. (2000). Architecture and processes in the late Pleistocene Brazos-Trinity turbidite system, Gulf of Mexico continental slope.

Bagnold, R. A. (1962). Auto-suspension of transported sediment; turbidity currents. *Proceedings of the Royal Society of London. Series A. Mathematical and Physical Sciences*, *265*(1322), 315-319.

Bonnel, C. (2005). Mise en place des lobes distaux dans les systèmes turbiditiques actuels: Analyse comparée des systèmes du Zaïre, Var et Rhône., Settings of distal turbiditic lobes: comparison of Zaire (Congo), Var and Rhone systems (Doctoral dissertation, Université Bordeaux 1).

Bouma, A. (1964). Turbidites. In Developments in sedimentology (Vol. 3, pp. 247-256). Elsevier.

Bouma, A. H. (1962). Sedimentology of some flysch deposits. *Agraphic approach to facies interpretation*, *168*.

Bouma, A. H. (1985). Introduction to submarine fans and related turbidite systems. In Submarine fans and related turbidite systems (pp. 3-5). Springer, New York, NY.

Carter, L., Gavey, R., Talling, P. J., & Liu, J. T. (2014). Insights into submarine geohazards from breaks in subsea telecommunication cables. *Oceanography*, *27*(2), 58-67.

Clark, J. D., Kenyon, N. H., & Pickering, K. T. (1992). Quantitative analysis of the geometry of submarine channels: implications for the classification of submarine fans. *Geology*, *20*(7), 633-636.

Covault, J. A., & Graham, S. A. (2010). Submarine fans at all sea-level stands: Tectono-morphologic and climatic controls on terrigenous sediment delivery to the deep sea. *Geology*, *38*(10), 939-942.

Covault, J. A., Romans, B. W., Fildani, A., McGann, M., & Graham, S. A. (2010). Rapid climatic signal propagation from source to sink in a southern California sediment-routing system. The Journal of Geology, 118(3), 247-259.

Deptuck, M. E., & Sylvester, Z. (2018). Submarine fans and their channels, levees, and lobes. *Submarine geomorphology*, 273-299.

Deptuck, M. E., Piper, D. J., Savoye, B., & Gervais, A. (2008). Dimensions and architecture of late Pleistocene submarine lobes off the northern margin of East Corsica. *Sedimentology*, *55*(4), 869-898.

Dietrich, W. E. (1982). Settling velocity of natural particles. *Water resources research*, *18*(6), 1615-1626.

Ferguson, R. A., Kane, I. A., Eggenhuisen, J. T., Pohl, F., Tilston, M., Spychala, Y. T., & Brunt, R. L. (2020). Entangled external and internal controls on submarine fan evolution: an experimental perspective. *The Depositional Record*, *6*(3), 605-624.

Ferry, J. N., Babonneau, N., Mulder, T., Parize, O., & Raillard, S. (2004). Morphogenesis of Congo submarine canyon and valley: implications about the theories of the canyons formation. *Geodinamica Acta*, *17*(4), 241-251.

Fildani, A. (2017). Submarine Canyons: A brief review looking forward. *Geology*, *45*(4), 383-384.

Fildani, A., Normark, W. R., Kostic, S., & Parker, G. (2006). Channel formation by flow stripping: Large-scale scour features along the Monterey East Channel and their relation to sediment waves. *Sedimentology*, *53*(6), 1265-1287.

Fisher, W. L., Galloway, W. E., Steel, R. J., Olariu, C., Kerans, C., & Mohrig, D. (2021). Deep-water depositional systems supplied by shelf-incising submarine canyons: Recognition and significance in the geologic record. *Earth-Science Reviews*, *214*, 103531.

Flood, R. D., Manley, P. L., Kowsmann, R. O., Appi, C. J., & Pirmez, C. (1991). Seismic facies and late Quaternary growth of Amazon submarine fan. *Seismic facies and sedimentary processes of submarine fans and turbidite systems*, 415-433

Galy, V., France-Lanord, C., Beyssac, O., Faure, P., Kudrass, H., & Palhol, F. (2007). Efficient organic carbon burial in the Bengal fan sustained by the Himalayan erosional system. *Nature*, *450*(7168), 407-410.

Ganti, V., Hajek, E. A., Leary, K., Straub, K. M., & Paola, C. (2020). Morphodynamic hierarchy and the fabric of the sedimentary record. *Geophysical Research Letters*, *47*(14), e2020GL087921.

Garcia, M., & Parker, G. (1989). Experiments on hydraulic jumps in turbidity currents near a canyon-fan transition. *Science*, *245*(4916), 393-396.

Garcia, M., & Parker, G. (1991). Entrainment of bed sediment into suspension. *Journal of Hydraulic Engineering*, *117*(4), 414-435.

Gervais, A., Savoye, B., Piper, D. J., Mulder, T., Cremer, M., & Pichevin, L. (2004). Present morphology and depositional architecture of a sandy confined submarine system: the Golo turbidite system (eastern margin of Corsica). *Geological Society, London, Special Publications*, *222*(1), 59-89.

Habgood, E. L., Kenyon, N. H., Masson, D. G., Akhmetzhanov, A., Weaver, P. P., Gardner, J., & Mulder, T. (2003). Deep‐water sediment wave fields, bottom current sand channels and gravity flow channel‐lobe systems: Gulf of Cadiz, NE Atlantic. Sedimentology, 50(3), 483-510.

Hage, S., Galy, V. V., Cartigny, M. J. B., Acikalin, S., Clare, M. A., Gröcke, D. R., ... & Talling, P. J. (2020). Efficient preservation of young terrestrial organic carbon in sandy turbidity-current deposits. *Geology*, *48*(9), 882-887.

Halsey, T. C., & Kumar, A. (2019). Levees Formed by Turbidity Currents: A Depth-Averaged Modeling Treatment. *Journal of Geophysical Research: Oceans*, *124*(7), 4389-4415.

Halsey, T. C., Kumar, A., & Perillo, M. M. (2017). Sedimentological regimes for turbidity currents: Depth-averaged theory. *Journal of GEOPHYSICAL research: Oceans*, *122*(7), 5260-5285.

Hamilton, P. B., Strom, K. B., & Hoyal, D. C. (2015). Hydraulic and sediment transport properties of autogenic avulsion cycles on submarine fans with supercritical distributaries. *Journal of Geophysical Research: Earth Surface*, *120*(7), 1369-1389.

Hamilton, P., Gaillot, G., Strom, K., Fedele, J., & Hoyal, D. (2017). Linking hydraulic properties in supercritical submarine distributary channels to depositional-lobe geometry. Journal of Sedimentary Research, 87(9), 935-950.

Hawie, N., Covault, J. A., Dunlap, D., & Sylvester, Z. (2018). Slope-fan depositional architecture from high-resolution forward stratigraphic models. Marine and Petroleum Geology, 91, 576-585.

Heezen, B. C., & Ewing, W. M. (1952). Turbidity currents and submarine slumps, and the 1929 Grand Banks [Newfoundland] earthquake. *American journal of Science*, *250*(12), 849-873.

Hessler, A. M., & Fildani, A. (2019). Deep-sea fans: Tapping into Earth's changing landscapes. *Journal of Sedimentary Research*, *89*(11), 1171-1179.

Hughes Clarke, J. E., Mayer, L. A., & Wells, D. E. (1996). Shallow-water imaging multibeam sonars: A new tool for investigating seafloor processes in the coastal zone and on the continental shelf. Marine Geophysical Researches, 18(6), 607-629.

Jackson, A., Stright, L., Hubbard, S. M., & Romans, B. W. (2019). Static connectivity of stacked deep-water channel elements constrained by high-resolution digital outcrop models. AAPG Bulletin, 103(12), 2943-2973.

Jobe, Z. R., Lowe, D. R., & Uchytil, S. J. (2011). Two fundamentally different types of submarine canyons along the continental margin of Equatorial Guinea. *Marine and Petroleum Geology*, *28*(3), 843-860.

Jobe, Z. R., Sylvester, Z., Howes, N., Pirmez, C., Parker, A., Cantelli, A., ... & Prather, B. (2017). High-resolution, millennial-scale patterns of bed compensation on a sand-rich intraslope submarine fan, western Niger Delta slope. *Bulletin*, *129*(1-2), 23-37.

Kane, I. A., Clare, M. A., Miramontes, E., Wogelius, R., Rothwell, J. J., Garreau, P., & Pohl, F. (2020). Seafloor microplastic hotspots controlled by deep-sea circulation. Science, 368(6495), 1140-1145.

Kolla, V. (2007). A review of sinuous channel avulsion patterns in some major deep-sea fans and factors controlling them. *Marine and Petroleum Geology*, *24*(6-9), 450-469.

Kolla, V., & Coumes, F. (1987). Morphology, internal structure, seismic stratigraphy, and sedimentation of Indus Fan. *AAPG Bulletin*, *71*(6), 650-677.

Kuenen, P. H., & Migliorini, C. I. (1950). Turbidity currents as a cause of graded bedding. *The Journal of Geology*, *58*(2), 91-127.

Kuprenas, R., Tran, D., & Strom, K. (2018). A shear-limited flocculation model for dynamically predicting average floc size. *Journal of Geophysical Research: Oceans*, *123*(9), 6736-6752.

Kuster, G. T., & Toksöz, M. N. (1974). Velocity and attenuation of seismic waves in two-phase media: Part I. Theoretical formulations. *Geophysics*, *39*(5), 587-606.

Lowe, D. R. (1982). Sediment gravity flows; II, Depositional models with special reference to the deposits of high-density turbidity currents. *Journal of sedimentary research*, *52*(1), 279-297.

Mavko, G., Mukerji, T. and Dvorkin, J., 2009, The Rock Physics Handbook, Cambridge University Press.

McHargue, T. R., & Webb, J. E. (1986). Internal geometry, seismic facies, and petroleum potential of canyons and inner fan channels of the Indus submarine fan. AAPG bulletin, 70(2), 161-180.

McHargue, T., Pyrcz, M. J., Sullivan, M. D., Clark, J. D., Fildani, A., Romans, B. W., ... & Drinkwater, N. J. (2011). Architecture of turbidite channel systems on the continental slope: patterns and predictions. Marine and petroleum geology, 28(3), 728-743.

McKay, M. D., Beckman, R. J., & Conover, W. J. (2000). A comparison of three methods for selecting values of input variables in the analysis of output from a computer code. *Technometrics*, *42*(1), 55-6McKay, M. D., Beckman, R. J., & Conover, W. J.

(1979). Comparison of Three Methods for Selecting Values of Input Variables in the Analysis of Output from a Computer Code. *Technometrics*, *21*(2), 239-245.1.

Meirovitz, C. D., Stright, L., Hubbard, S. M., & Romans, B. W. (2021). The influence of inter- and intra-channel architecture on deep-water turbidite reservoir performance. Petroleum Geoscience, 27(2), petgeo2020-005.

Meyer-Peter, E., & Müller, R. (1948). Formulas for bed-load transport. In IAHSR 2nd meeting, Stockholm, appendix 2. IAHR.Aki, K. and Richards, P.G, 2002, Quantitative Seismology, University Science Books,

Miller, J. K., Sun, T., Li, H., Stewart, J., Genty, C., Li, D., & Lyttle, C. (2008, December). Direct modeling of reservoirs through forward process-based models: Can we get there?. In International petroleum technology conference. OnePetro.

Mitchum Jr, R. M., Vail, P. R., & Thompson III, S. (1977). Seismic stratigraphy and global changes of sea level: Part 2. The depositional sequence as a basic unit for stratigraphic analysis: Section 2. Application of seismic reflection configuration to stratigraphic interpretation.

Mutti, E., & Ricci Lucchi, F. (1978). Turbidites of the northern Apennines: introduction to facies analysis. *International geology review*, *20*(2), 125-166.

Nielson, A. (2018). Using RMS Amplitudes from Forward Seismic-Reflectivity Modeling of Channelized Deep-Water Slope Deposits to Inform Stratigraphic Interpretation and Sub-Seismic Scale Architecture, Tres Pasos Formation, Magallanes Basin, Patagonia, Chile (Doctoral dissertation, Colorado State University).

Normark, W. R. (1970). Growth patterns of deep-sea fans. *AAPG bulletin*, *54*(11), 2170-2195.

Othman, A. A., Fathy, M., & Maher, A. (2016). Use of spectral decomposition technique for delineation of channels at Solar gas discovery, offshore West Nile Delta, Egypt. *Egyptian Journal of Petroleum*, *25*(1), 45-51.

Parker, G., Fukushima, Y., & Pantin, H. M. (1986). Self-accelerating turbidity currents. *Journal of Fluid Mechanics*, *171*, 145-181.

Paull, C. K., Caress, D. W., Lundsten, E., Gwiazda, R., Anderson, K., McGann, M., ... & Sumner, E. J. (2013). Anatomy of the La Jolla submarine canyon system; offshore Southern California. *Marine Geology*, *335*, 16-34.

Peakall, J., McCaffrey, B., & Kneller, B. (2000). A process model for the evolution, morphology, and architecture of sinuous submarine channels. *Journal of Sedimentary Research*, *70*(3), 434-448.

Pemberton, E. A., Stright, L., Fletcher, S., & Hubbard, S. M. (2018). The influence of stratigraphic architecture on seismic response: Reflectivity modeling of outcropping deepwater channel units. Interpretation, 6(3), T783-T808.

Pemberton, E. A., Stright, L., Fletcher, S., & Hubbard, S. M. (2018). The influence of stratigraphic architecture on seismic response: Reflectivity modeling of outcropping deepwater channel units. Interpretation, 6(3), T783-T808.Garcia, M. H. Depositional turbidity currents laden with poorly sorted sediment. Journal of hydraulic engineering **120**, 1240-1263 (1994).

Picot, M., Droz, L., Marsset, T., Dennielou, B., & Bez, M. (2016). Controls on turbidite sedimentation: Insights from a quantitative approach of submarine channel and lobe architecture (Late Quaternary Congo Fan). *Marine and Petroleum Geology*, *72*, 423-446.

Pirmez, C., Beaubouef, R. T., Friedmann, S. J., & Mohrig, D. C. (2000). Equilibrium profile and baselevel in submarine channels: examples from Late Pleistocene systems and implications for the architecture of deepwater reservoirs.

Pirmez, C., Prather, B. E., Mallarino, G., O'hayer, W. W., Droxler, A. W., & Winker, C. D. (2012). Chronostratigraphy of the Brazos–Trinity depositional system, western Gulf of Mexico: implications for deepwater depositional models.

Pohl, F., Eggenhuisen, J. T., Kane, I. A., & Clare, M. A. (2020). Transport and burial of microplastics in deep-marine sediments by turbidity currents. Environmental science & technology, 54(7), 4180-4189.

Pope, E. L., Cartigny, M. J., Clare, M. A., Talling, P. J., Lintern, D. G., Vellinga, A., ... & Vendettuoli, D. (2022). First source-to-sink monitoring shows dense head controls sediment flux and runout in turbidity currents. Science Advances, 8(20), eabj3220.

Posamentier, H. W., & Walker, R. G. (2006). Deep-water turbidites and submarine fans.

Prather, B. E., Keller, F. B., & Chapin, M. A. (2000). Hierarchy of deep-water architectural elements with reference to seismic resolution: implications for reservoir prediction and modeling.

Prather, B. E., Pirmez, C. A. R. L. O. S., & Winker, C. D. (2012). Stratigraphy of linked intraslope basins: Brazos–Trinity system western Gulf of Mexico. SEPM, Special Publication **99**, 83-109 (2012).

Richards, M., Bowman, M., & Reading, H. (1998). Submarine-fan systems I: characterization and stratigraphic prediction. Marine and Petroleum Geology, 15(7), 689-717.

Savoye, B., Babonneau, N., Dennielou, B., & Bez, M. (2009). Geological overview of the Angola–Congo margin, the Congo deep-sea fan and its submarine valleys. *Deep Sea Research Part II: Topical Studies in Oceanography*, *56*(23), 2169-2182.

Schwenk, T., & Spieß, V. (2009). Architecture and stratigraphy of the Bengal Fan as response to tectonic and climate revealed from high-resolution seismic data.

Shanmugam, G. (2016). Submarine fans: a critical retrospective (1950–2015). *Journal of Palaeogeography*, *5*(2), 110-184.

Simmons, S. M., Azpiroz-Zabala, M., Cartigny, M. J. B., Clare, M. A., Cooper, C., Parsons, D. R., ... & Talling, P. J. (2020). Novel acoustic method provides first detailed measurements of sediment concentration structure within submarine turbidity currents. *Journal of Geophysical Research: Oceans*, *125*(5), e2019JC015904.

Sømme, T. O., Piper, D. J., Deptuck, M. E., & Helland-Hansen, W. (2011). Linking onshore–offshore sediment dispersal in the Golo source-to-sink system (Corsica, France) during the late Quaternary. *Journal of Sedimentary Research*, *81*(2), 118-137.

Stow, D. A., & Mayall, M. (2000). Deep-water sedimentary systems: New models for the 21st century. Marine and Petroleum Geology, 17(2), 125-135.

Straub, K. M., & Pyles, D. R. (2012). Quantifying the hierarchical organization of compensation in submarine fans using surface statistics. *Journal of Sedimentary Research*, *82*(11), 889-898.

Stright, L., Stewart, J., Campion, K., & Graham, S. (2014). Geologic and seismic modeling of a coarse-grained deep-water channel reservoir analog (Black's Beach, La Jolla, California) Seismic Modeling of a Deep-Water Reservoir Outcrop Analog, California. AAPG bulletin, 98(4), 695-728.

Sweet, M. L., Gaillot, G. T., Jouet, G., Rittenour, T. M., Toucanne, S., Marsset, T., & Blum, M. D. (2020). Sediment routing from shelf to basin floor in the Quaternary Golo System of Eastern Corsica, France, western Mediterranean Sea. *GSA bulletin*, *132*(5-6), 1217-1234.

Sweet, M. L., Gaillot, G. T., Jouet, G., Rittenour, T. M., Toucanne, S., Marsset, T., & Blum, M. D. (2020). Sediment routing from shelf to basin floor in the Quaternary Golo System of Eastern Corsica, France, western Mediterranean Sea. GSA bulletin, 132(5-6), 1217-1234.

Talling, P. J., Allin, J., Armitage, D. A., Arnott, R. W., Cartigny, M. J., Clare, M. A., ... & Xu, J. (2015). Key Future Directions For Research On Turbidity Currents And Their Depositskey Future Directions For Research On Turbidity Currents And Their Deposits. *Journal of Sedimentary Research*, *85*(2), 153-169.

Talling, P. J., Baker, M. L., Pope, E. L., Ruffell, S. C., Jacinto, R. S., Heijnen, M. S., ... & Hilton, R. J. (2022). Longest sediment flows yet measured show how major rivers connect efficiently to deep sea. *Nature communications*, *13*(1), 4193.

Vail, P. R. (1991). The stratigraphic signatures of tectonics, eustasy and sedeimentology-An overview. *Cycles and events in stratigraphy.*, 617-659.

Vendettuoli, D., Clare, M. A., Clarke, J. H., Vellinga, A., Hizzet, J., Hage, S., ... & Lintern, D. G. (2019). Daily bathymetric surveys document how stratigraphy is built and its extreme incompleteness in submarine channels. *Earth and Planetary Science Letters*, *515*, 231-247.

Wahab, A., Shringarpure, M., Hoyal, D., & Straub, K. (2022). A dimensionless framework for predicting submarine fan morphology.

Weimer, P., & Pettingill, H. S. (2007). Global overview of deep-water exploration and production.

Winker, C. D. (1996, May). High-resolution seismic stratigraphy of a late Pleistocene submarine fan ponded by salt-withdrawal mini-basins on the Gulf of Mexico continental slope. In *Offshore Technology Conference*. OnePetro.

Winterwerp, J. C. (1998). A simple model for turbulence induced flocculation of cohesive sediment. *Journal of hydraulic research*, *36*(3), 309-326.

Winterwerp, J. C., & Van Kesteren, W. G. (2004). *Introduction to the physics of cohesive sediment dynamics in the marine environment*. Elsevier.

Xu, S and White, R.E., 1995, A new velocity model for clay-sand mixtures, Geophysical Prospecting, **43**,91-118, https://doi.org/10.1111/j.1365-2478.1995.tb00126.x

Xu, S. and Payne, M.A., 2009, Modeling elastic properties in carbonate rocks, The Leading Edge, 28, 66-74, https://doi.org/10.1190/1.3064148

Yang, Y., & Aplin, A. C. (2004). Definition and practical application of mudstone porosity–effective stress relationships. *Petroleum Geoscience*, *10*(2), 153-162.

Figures

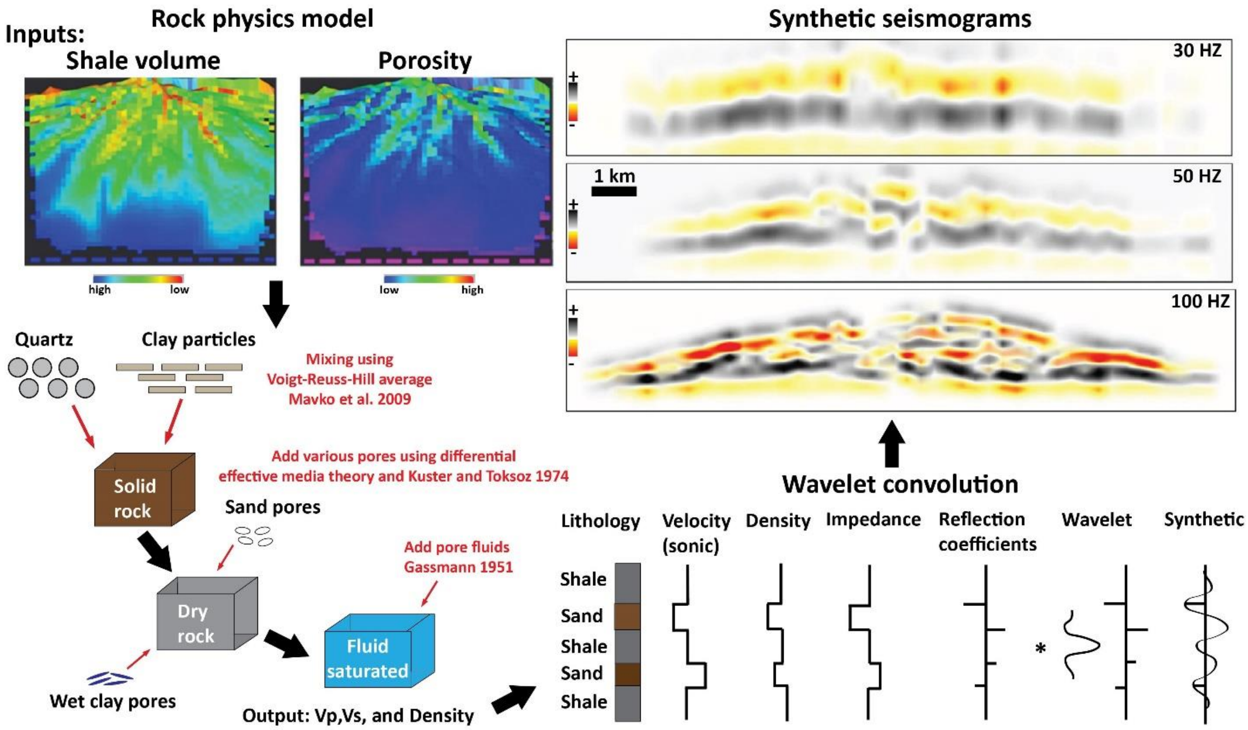

Figure 1. Workflow for forward seismic modeling. This workflow generates synthetic seismic surveys in several steps. First, synthetic stratigraphy from a select model is used to generate shale volume and porosity volume using a compaction algorithm (Yang and Aplin 2004). These volumes are used as input to a rock physics model that provides elastic outputs such as Vp, Vs, and Density (Xu and White, 1995; Xu and Payne, 2009). The elastic properties are used to compute the reflectivity series which are then convolved with a zero-phase Ricker wavelet to generate the final synthetic seismic survey of a desired frequency.

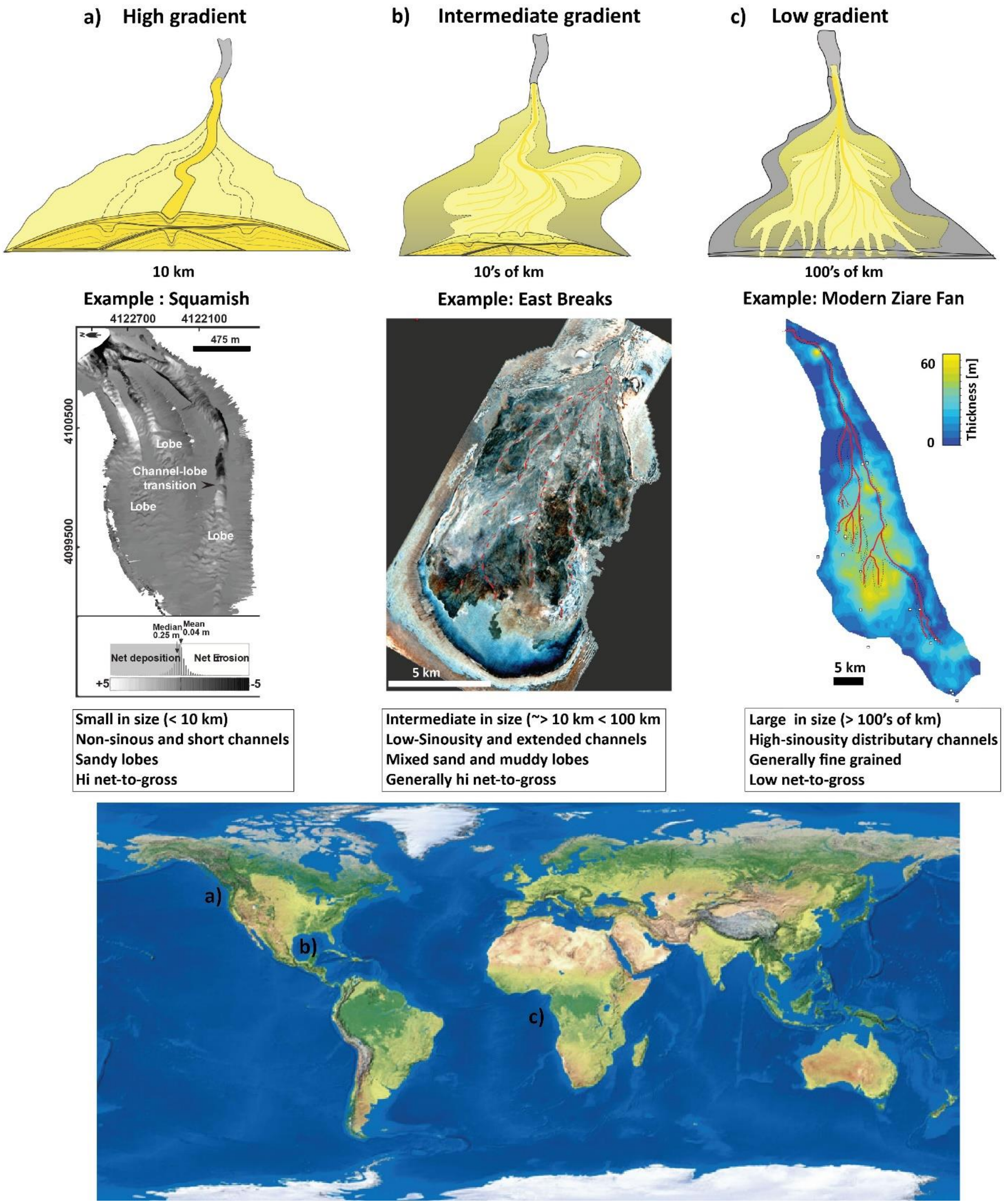

Figure 2. Relationship between antecedent gradient and submarine fan size and texture. a) A coupled schematic diagram and a map of deposition rate (generated from repeat bathymetric survey of the modern seafloor) of the Squamish example indicates that

submarine fans formed on high gradients (slope >1o) are generally small and sandy (from sediment samples) (Vendettuoli et al. 2019). b) A schematic map is coupled with an RGB blending horizon map (Othman et al. 2016) of the Basin-IV upper fan to highlight that a fan that is formed on intermediate gradients (slope 0.5o - 1.0o) can grow up to 10's of km and their deposits preserve both sand and mud (Pirmez et al. 2012; Prather et al. 2012). c) A schematic is coupled with a thickness map of a submarine fan that is formed on low gradients (slope <0.5o) that can grow up to a larger size and preserve mud rich deposits (Bobanneau et al. 2010).

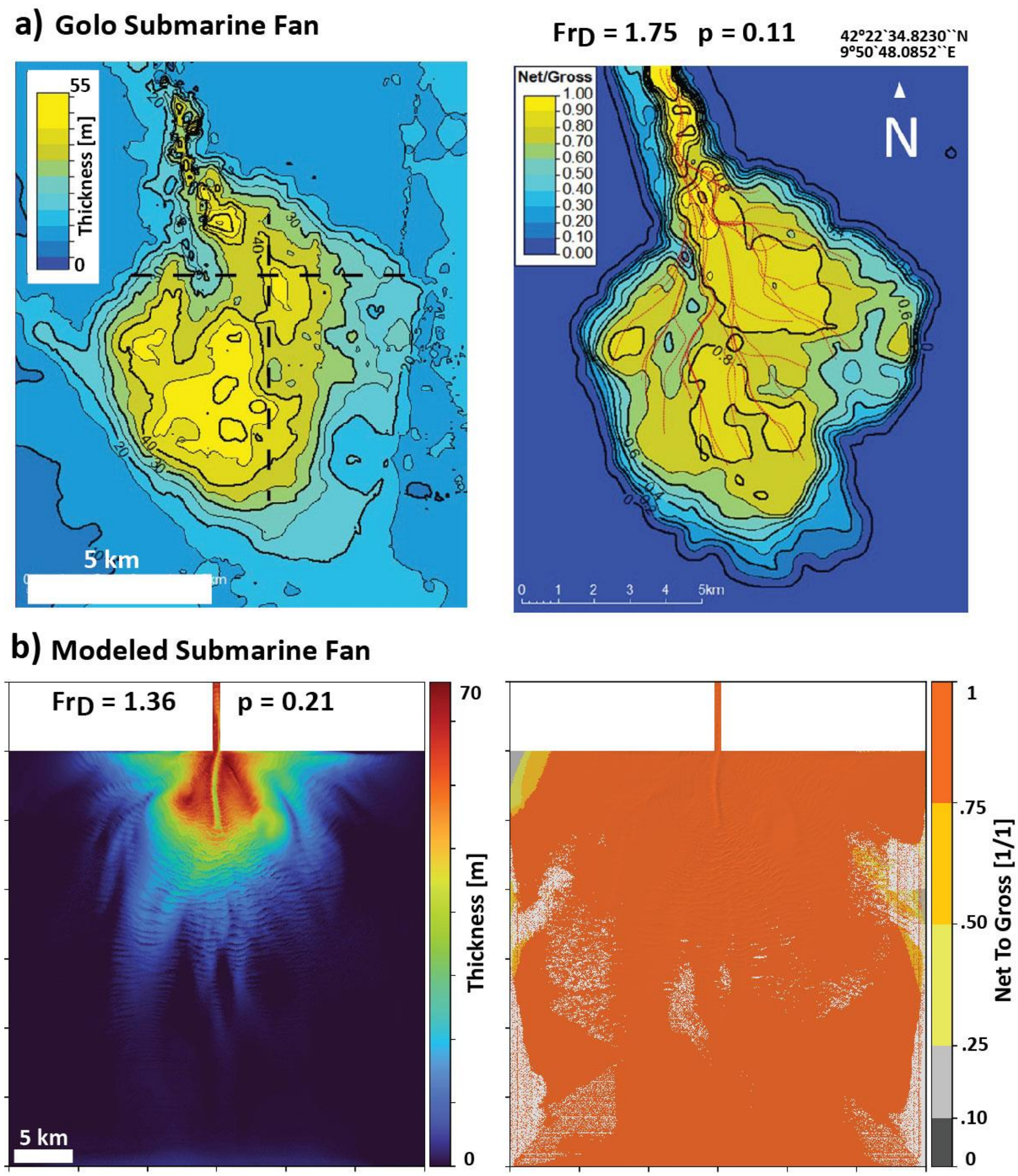

Figure 3. Comparison of the Quaternary Golo submarine fan to a high-gradient submarine fan numerical experiment. a) Maps show deposit thickness (contour interval is 10 m) and net-to-gross trends (contour interval is 0.1) in the Golo fan. The black dashed lines represent location of the seismic lines in Fig. 6a and 6c. The red dotted lines represent mapped channel bodies that are overlain on the net-to-gross map. b) Maps of deposit thickness and net-to-gross of high gradient submarine fan numerical experiment.

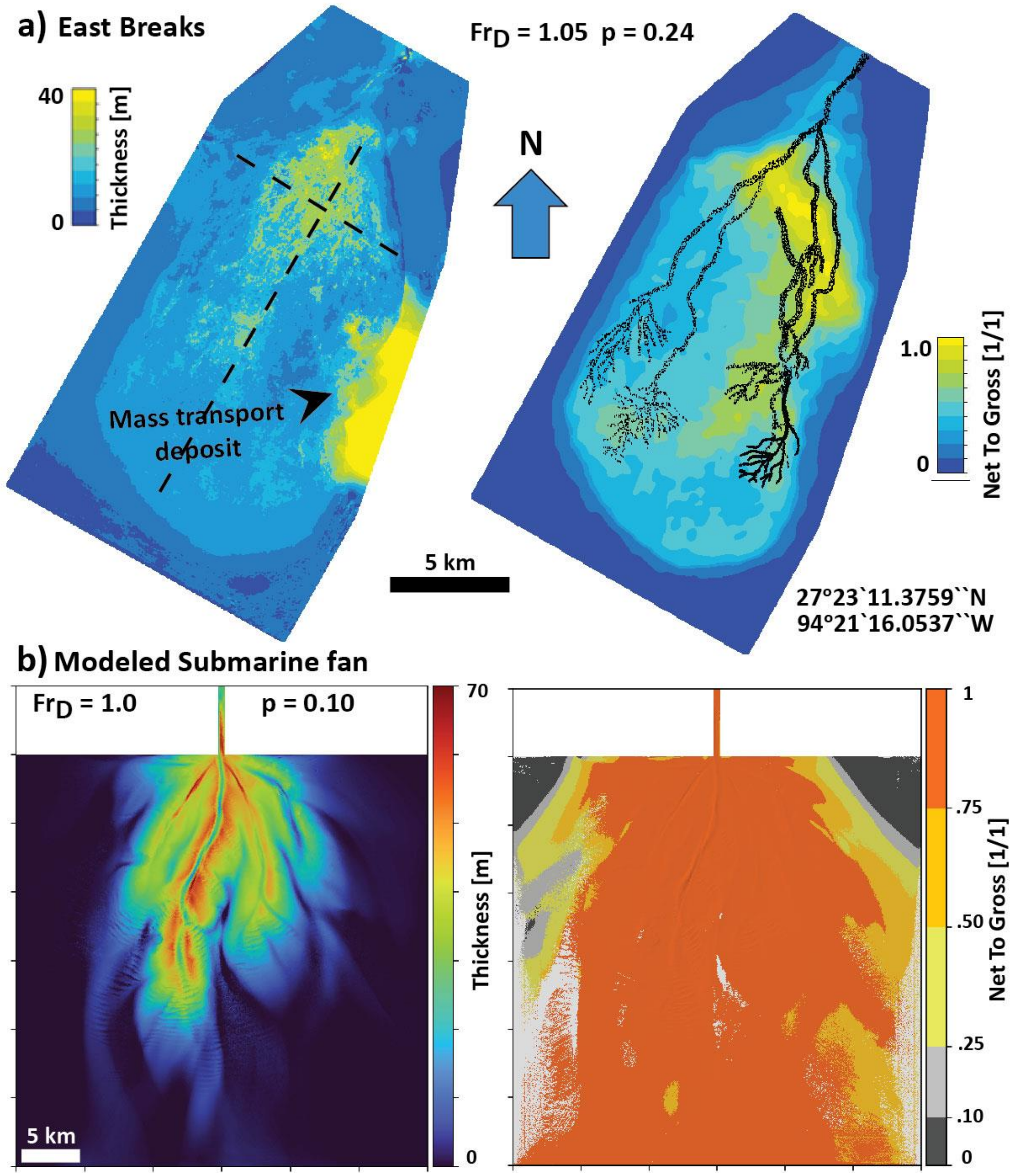

Figure 4. Comparison of the upper submarine fan in Basin IV of the Brazos-Trinity system to an intermediate-gradient submarine fan numerical experiment. a) Maps show deposit thickness and net-to-gross trends in the upper fan. The black dashed lines represent location of the seismic lines in Fig. 7a and 7c. The dotted lines represent mapped channel bodies interpreted in seismic volume. b) Maps of deposit thickness and net-to-gross for an intermediate gradient submarine fan numerical experiment.

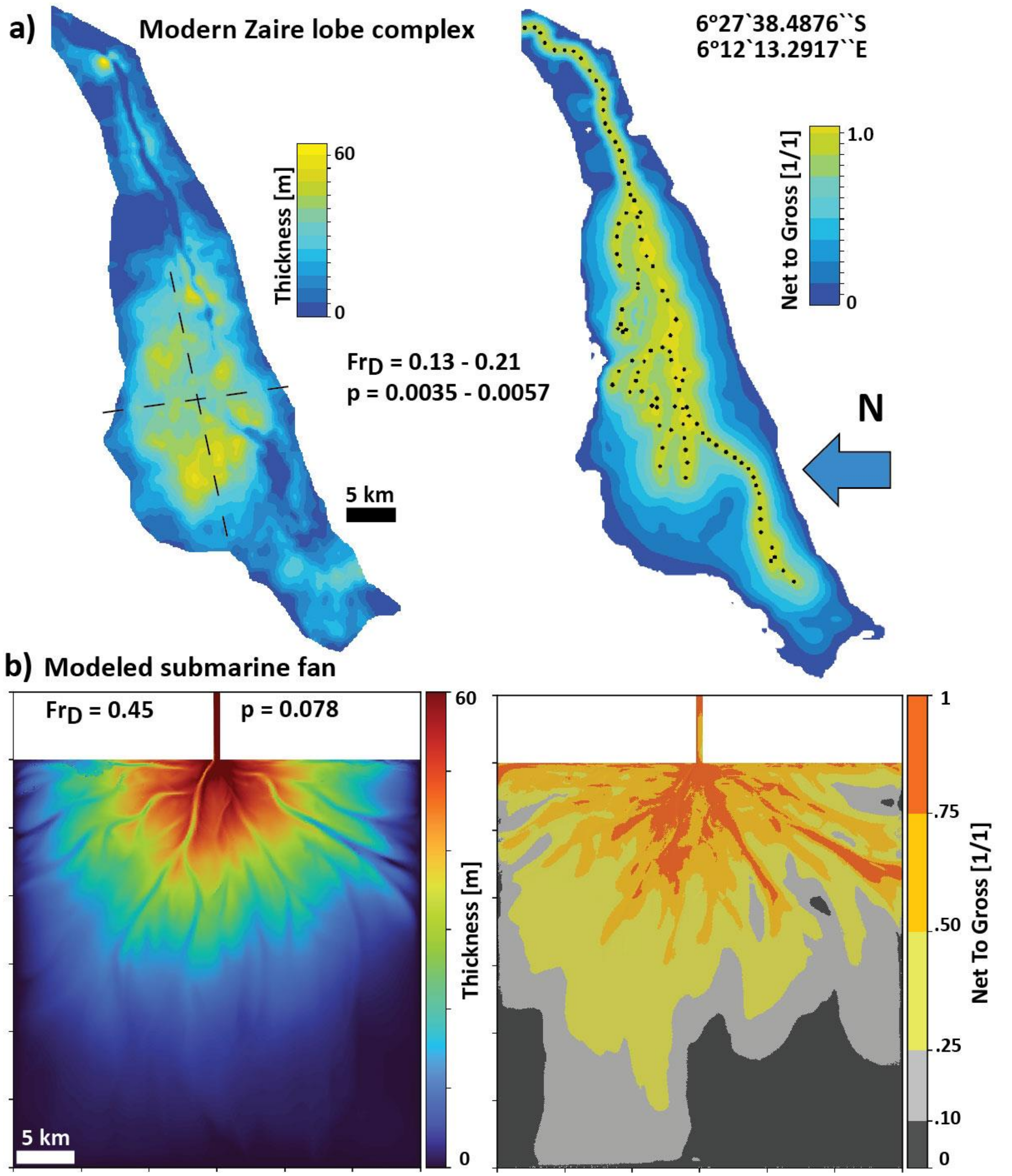

Figure 5. Comparison of the modern Zaire lobe complex to a low-gradient submarine fan numerical experiment. a) Maps show deposit thickness and net-to-gross trends in the modern Zaire lobe complex. The black dashed lines represent location of the seismic lines in Fig. 7a and 7c. Block dots on the map represent mapped channel locations. b) Maps of deposit thickness and net-to-gross resulting from a low gradient model.

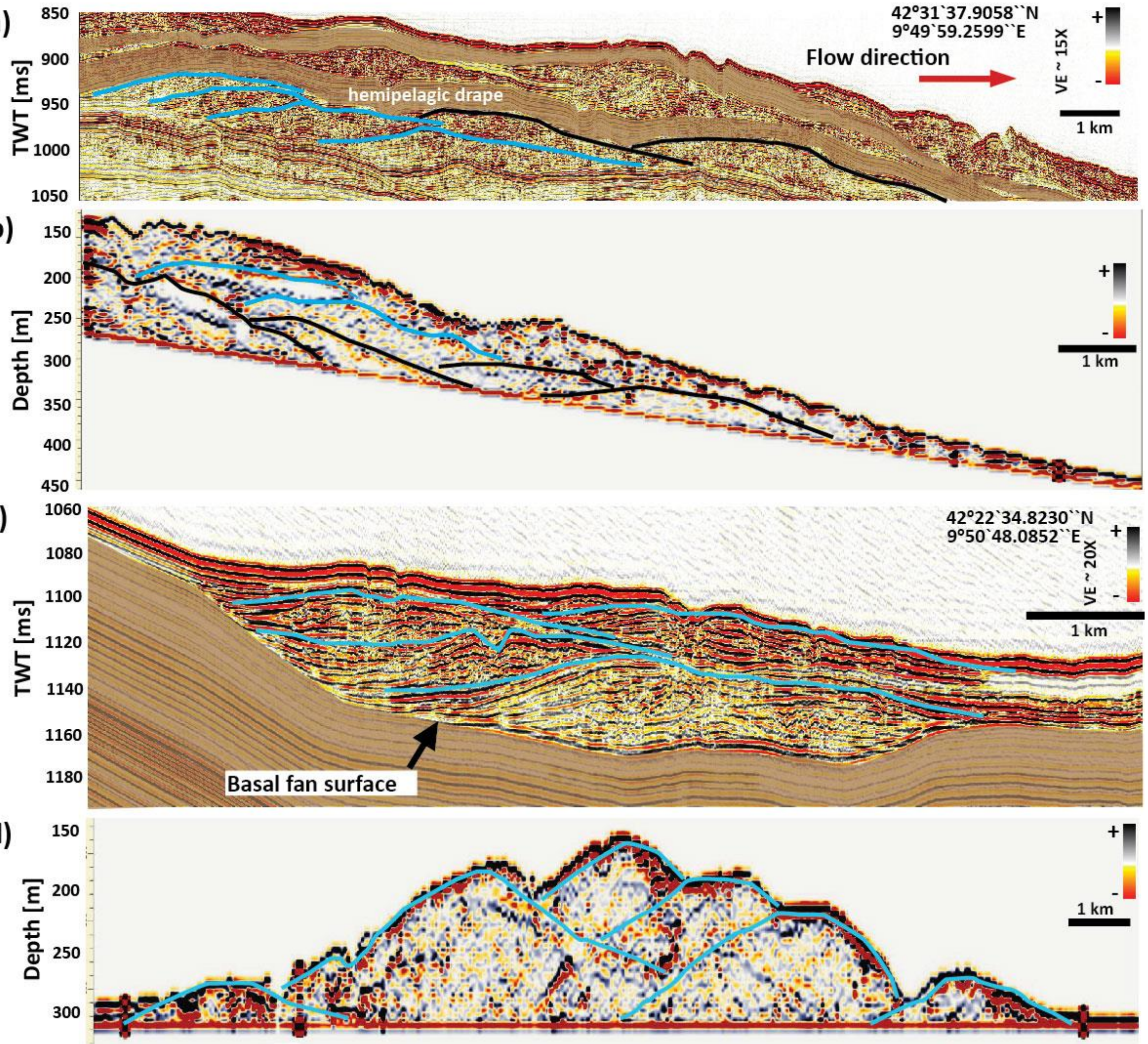

Figure 6. Comparison of seismic lines collected from the Quaternary Golo fan to a synthetic seismic survey generated from a modeled submarine fan. a) Dip seismic line from the Golo system shows onlapping reflector terminations (highlighted in blue) against the basal surface. Deposits of fans resulting from turbidity currents are separated by drapes of hemipelagic sediments, made semi-transparent here. These drapes are overlain by reflector terminations with downlapping geometries. b) Dip view from the synthetic seismic line shows similar stacking patterns as observed in a, minus the hemipelagic drapes. c) Strike view of the Golo seismic line shows compensational stacking of lobes (highlighted in blue). d) Strike view from synthetic seismic survey shows similar lobe stacking pattern as observed in c.

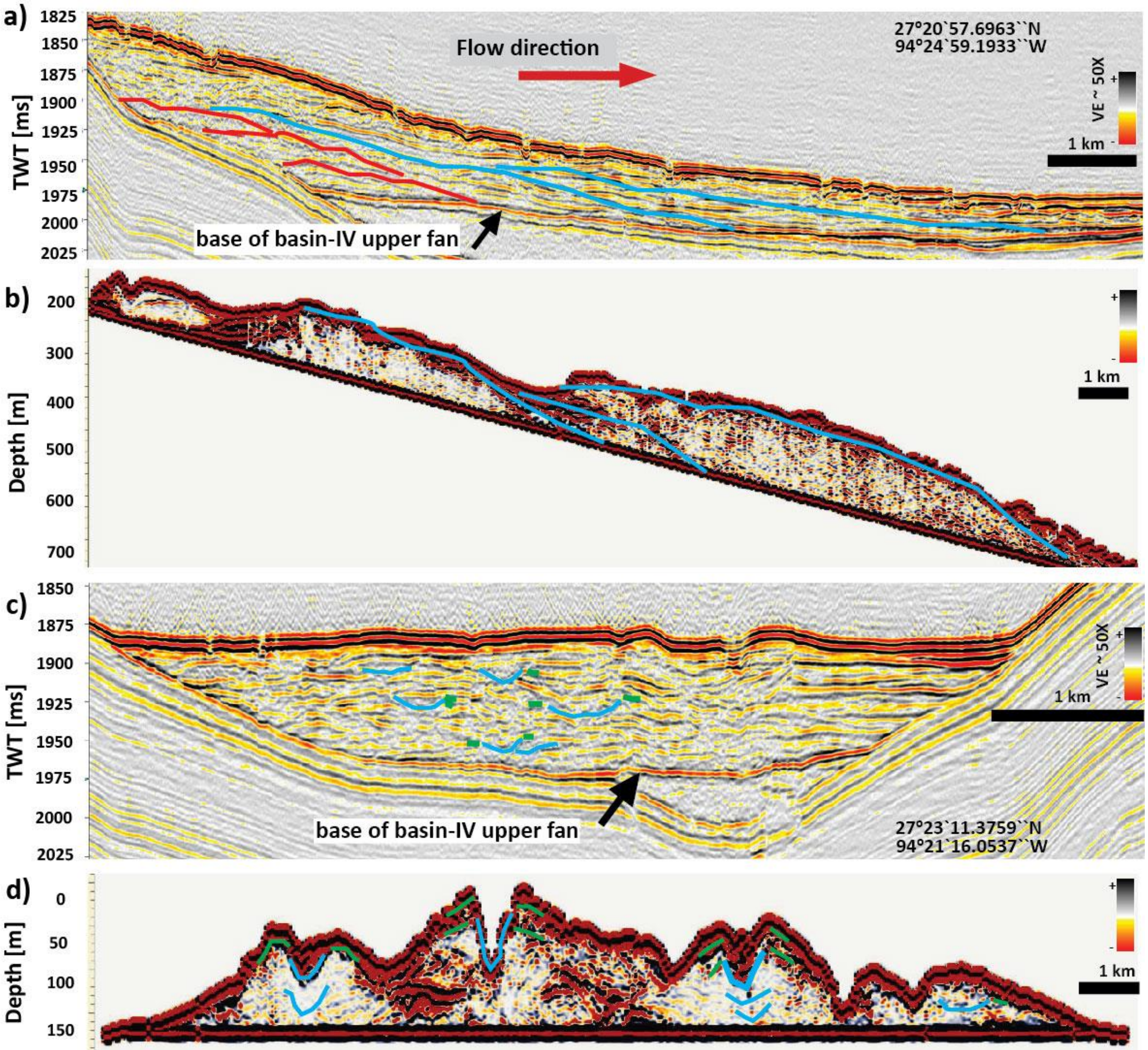

Figure 7. Comparison of seismic lines from Basin IV of the Brazos-Trinity system to a synthetic seismic survey generated from model stratigraphy. a) Dip view of the basin IV seismic line shows onlapping reflection terminations (highlighted in red) against the basal surface in the upper fan strata, which are overlain by reflectors with downlapping geometries (highlighted in blue). b) Dip view of the synthetic seismic survey only shows downlapping reflection terminations (highlighted in blue) against the basal surface. The lack of onlapping geometries in the synthetic surveys is due to fan growth on a constant slope that is relatively lower than the proximal input slope in Basin-IV c) Strike view of the basin IV seismic line shows clustered concave-up reflectors (highlighted in blue) adjacent to

diverging reflector terminations (highlighted in green). d) Strike view of the synthetic seismic data show similar seismic facies as observed in c.

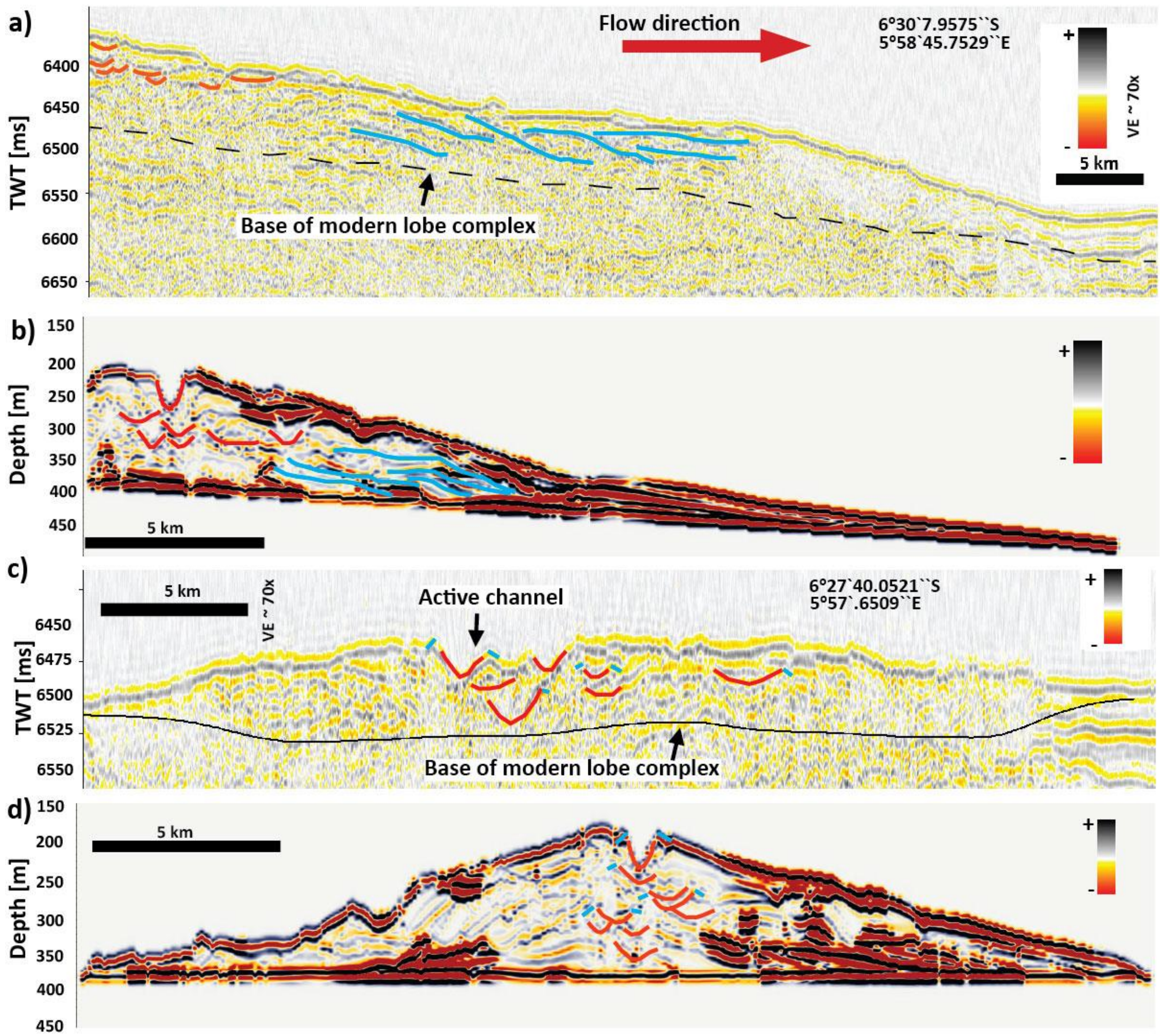

Figure 8. Comparison of seismic profiles collected from the modern Zaire fan to synthetic seismic of numerical experiment. a) Dip view of the Zaire seismic line shows proximal concave up geometries of reflectors (highlighted in red) that transition into laterally extensive and near horizontal reflectors (highlighted in blue) in the downstream direction. b) Dip oriented synthetic seismic profile from the model fan shows similar seismic facies as observed in a. c) Strike view of the Zaire seismic data shows clustered concave-up reflectors (highlighted in red) adjacent to diverging reflector (highlighted in blue) terminations. d) Strike view of the modeled synthetic seismogram shows similar seismic facies as observed in c.

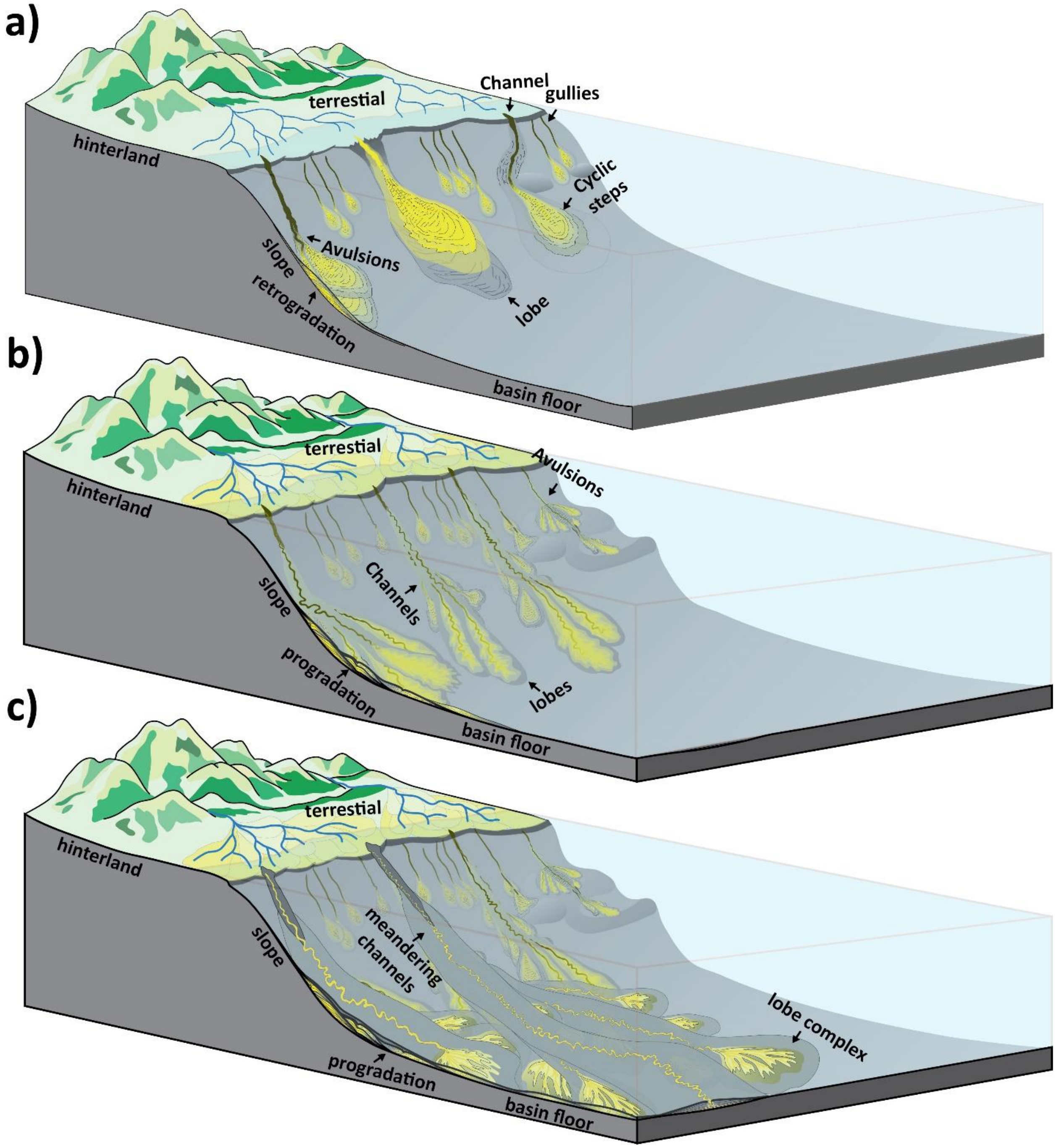

Figure 9. Depositional models for endmember submarine fans as a function of antecedent gradient. a) Schematic 3D representation of a continental margin and a submarine fan that developed on a high antecedent gradient. This fan is characterized by a relatively short length with proximally thick deposits and a high sand content. b) Schematic 3D representation of a submarine fan that grows on an intermediate gradient through several episodes of progradation into the basin. c) Schematic 3D representation of submarine a fan

that is formed on a low antecedent gradient. This fan is characterized by numerous distributive and meandering submarine channels with well-formed levees that can extend for 100's of km into the basin.

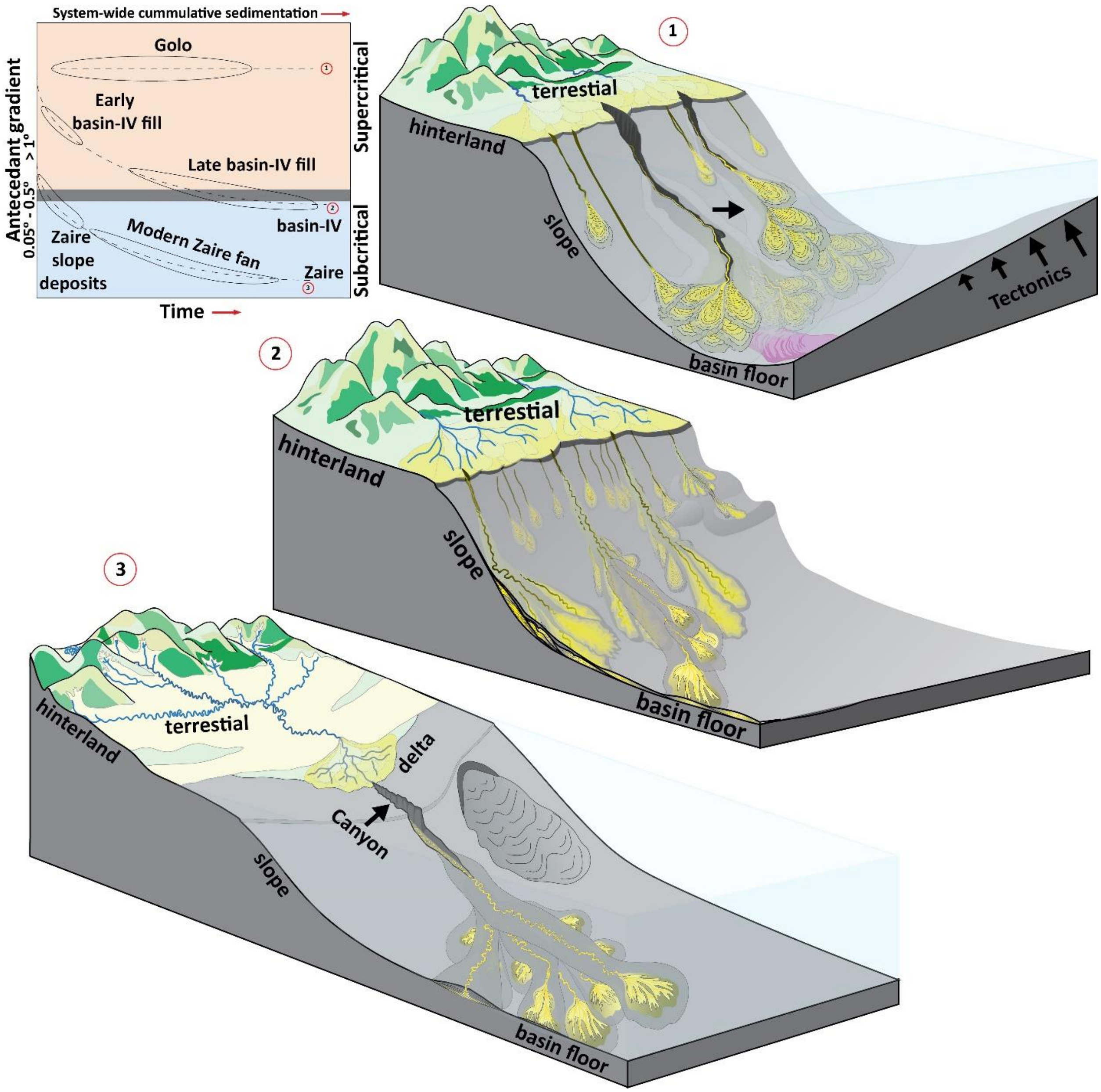

Figure 10. The evolution of a continental margin and its impact on submarine fan growth. The phase diagram shows the influence of system-wide sediment accumulations and antecedent gradient on the evolution of several known examples of modern submarine fans. The Golo fan continues growth on a high gradient due the influence of active salt tectonics that maintains overall high slope in the basin. Whereas Basin-IV and Zaire fan transition from initial growth on a high gradient to a more mature and distributive fan. This transition in gradient occurs because of system wide sediment accumulations in the basin that ultimately lowers the slope.

Supplementary materials

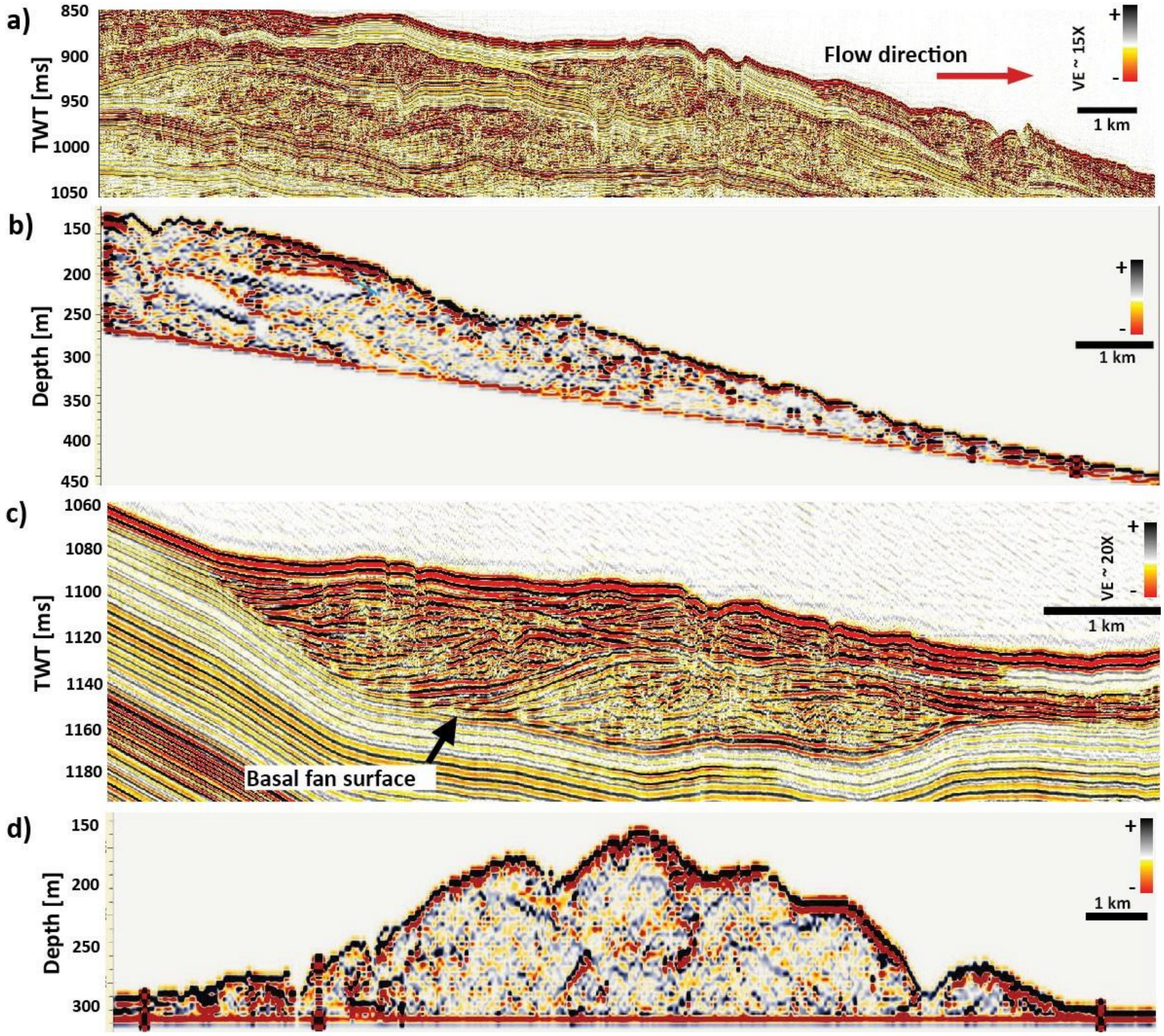

Supplementary Figure 1. Uninterpreted comparison of seismic lines collected from the Quaternary Golo fan to a synthetic seismic survey generated from a modeled submarine fan. See Figure 6 for detailed captions.

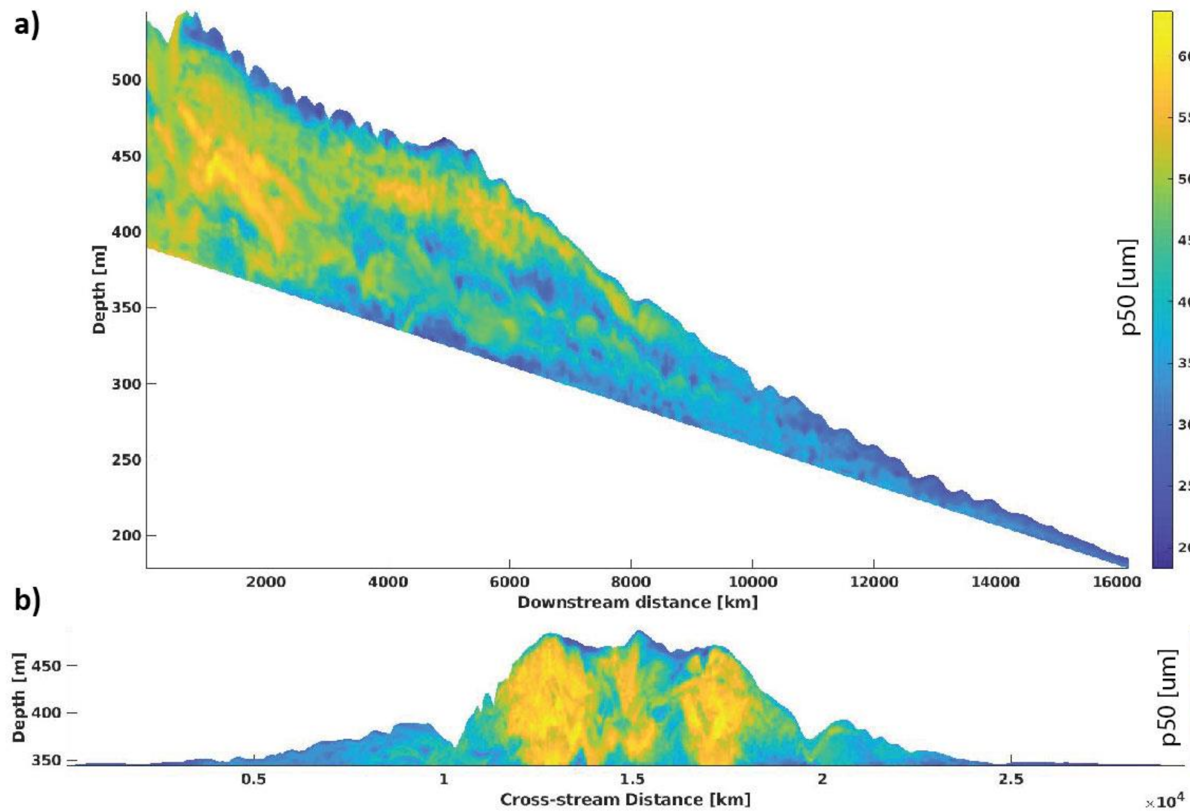

Supplementary Figure 2. Synthetic stratigraphy colored by the 50th percentile of the preserved grain sizes in the deposit. a) Dip section of stratigraphy from which synthetic seismogram in Fig, 6b was generated, b) Cross-section of stratigraphy from which the synthetic seismogram in Fig. 6d was generated.

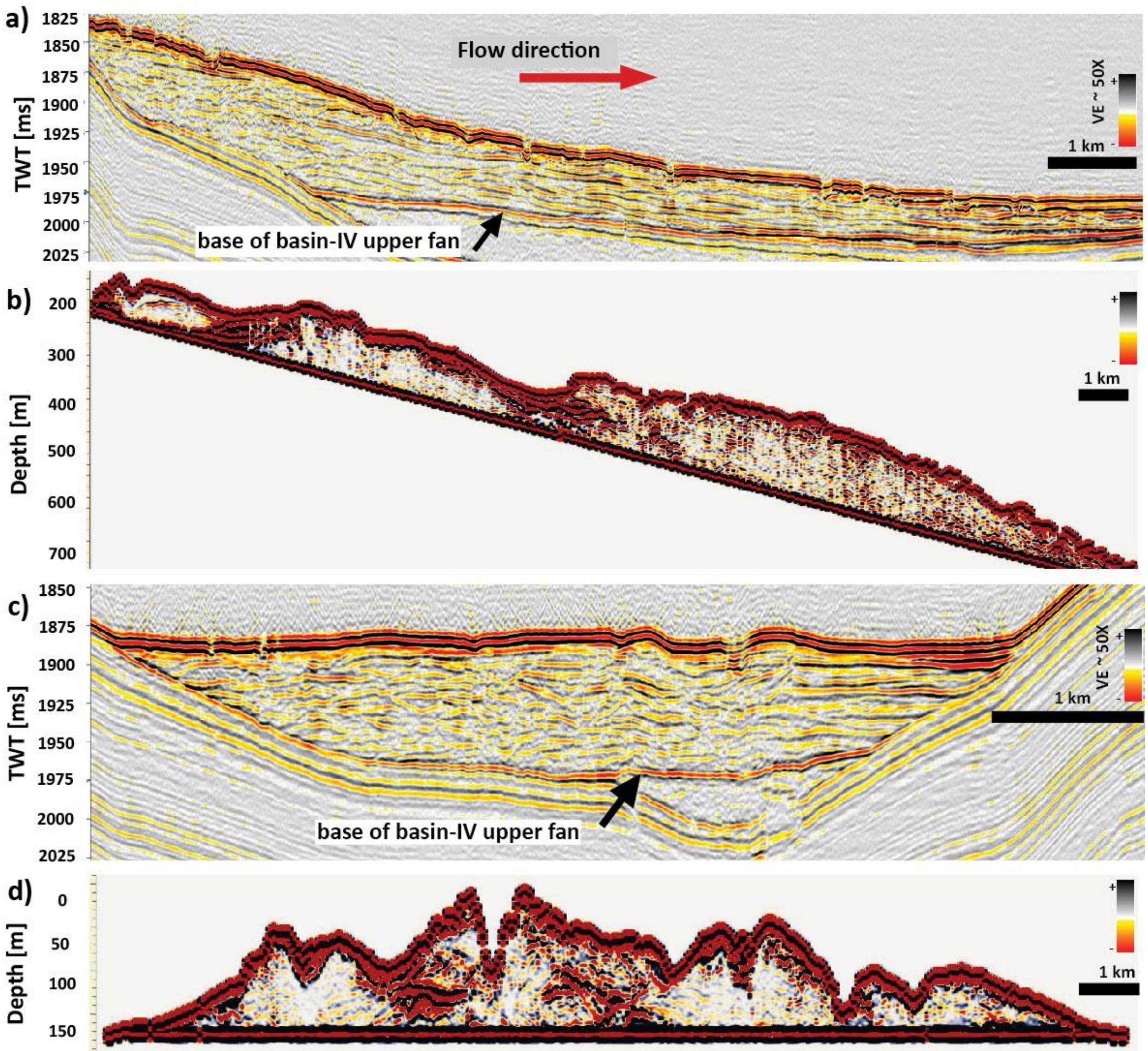

Supplementary Figure 3. Uninterpreted comparison of seismic lines from Basin IV of the Brazos-Trinity system to a synthetic seismic survey generated from model stratigraphy. See Figure 7 for detailed captions.

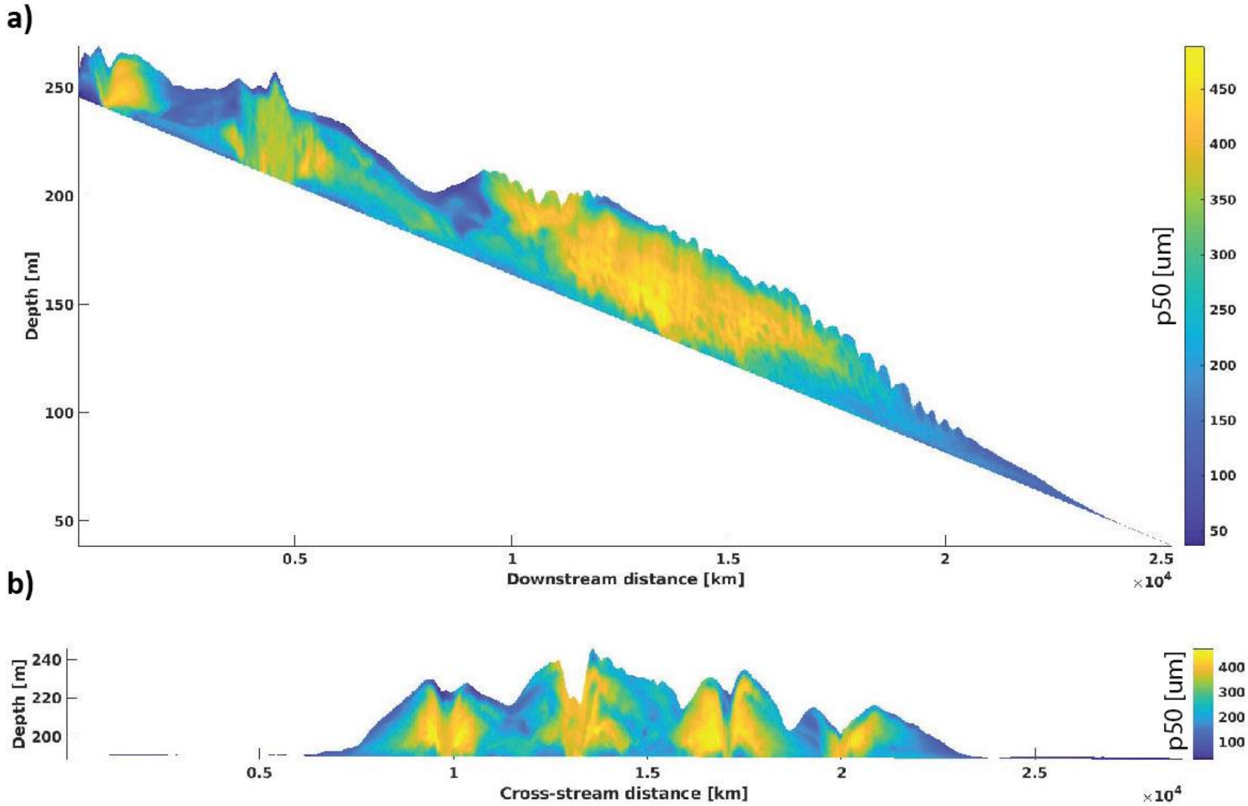

Supplementary Figure 4. Synthetic stratigraphy colored by the 50th percentile of the preserved grain sizes in the deposit. a) Dip section of stratigraphy from which synthetic seismogram in Fig, 7b was generated, b) Cross-section of stratigraphy from which the synthetic seismogram in Fig. 7d was generated.

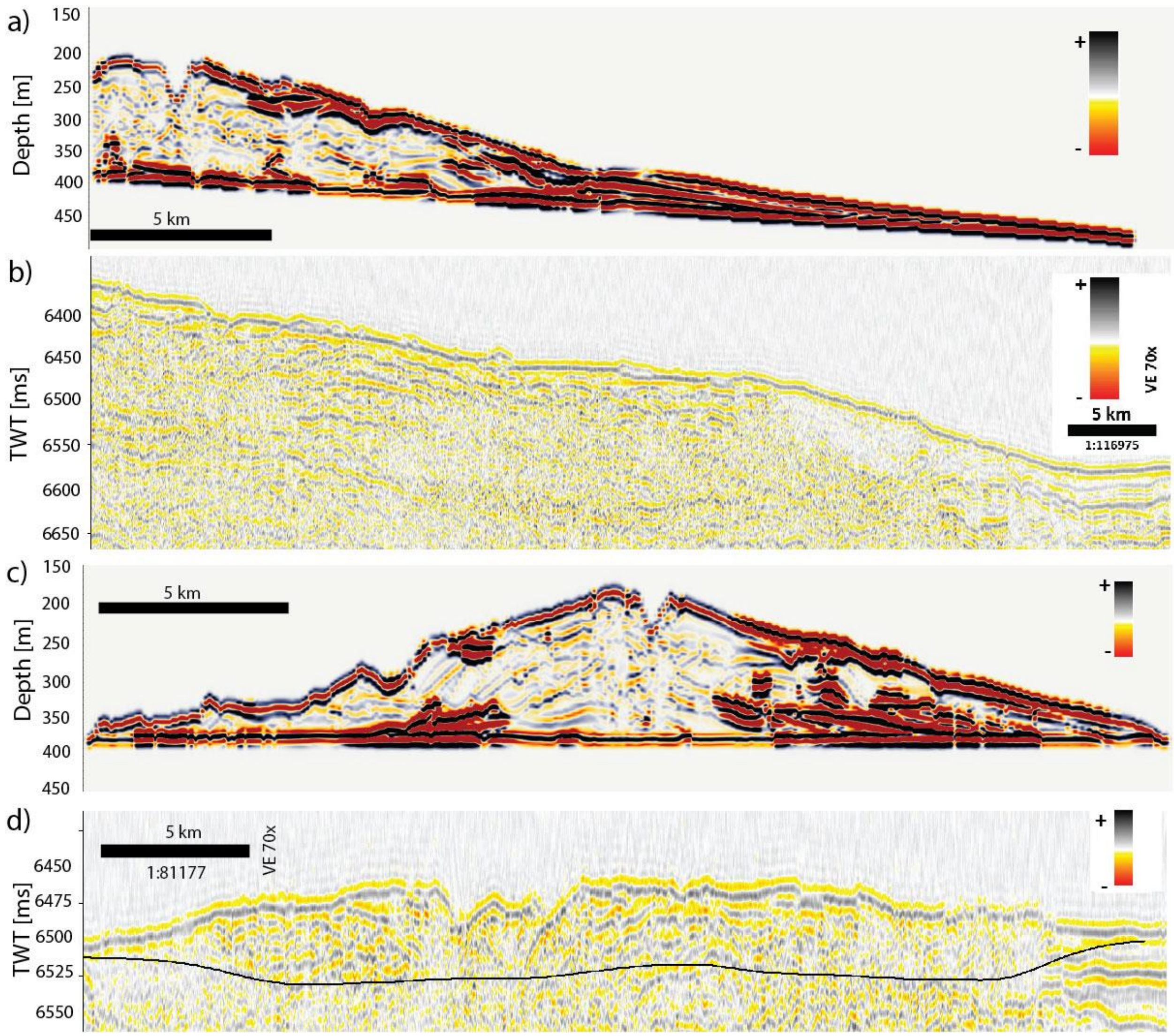

Supplementary Figure 5. Uninterpreted comparison of seismic profiles collected from the modern Zaire fan to synthetic seismic of numerical experiment. See Figure 8 for detailed captions.

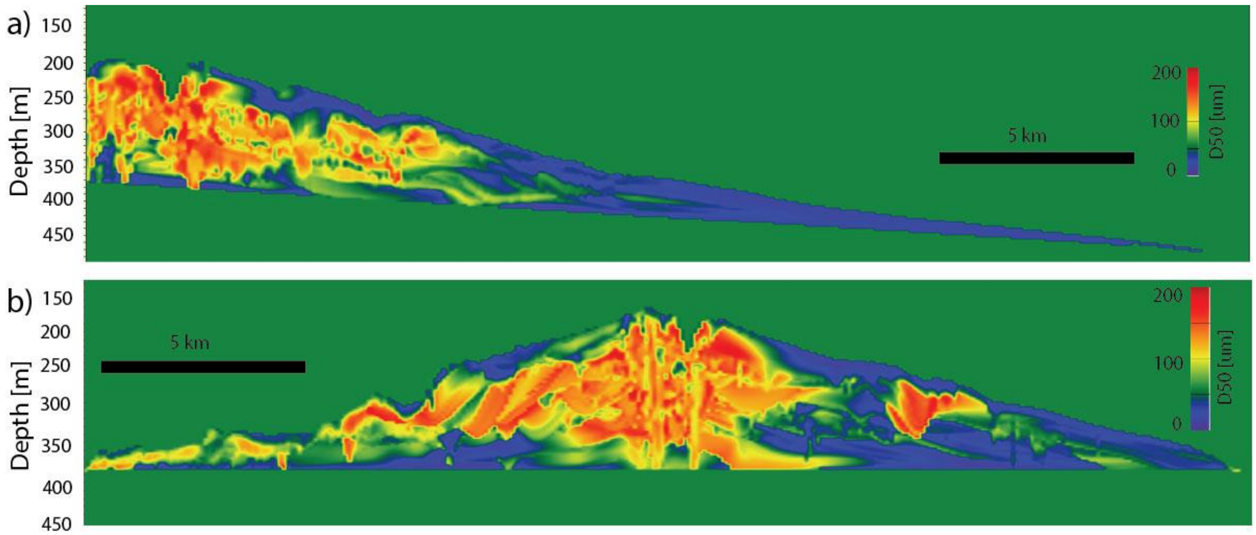

Supplementary Figure 6. Synthetic stratigraphy colored by the 50th percentile of the preserved grain sizes in the deposit. a) Dip section of stratigraphy from which synthetic seismogram in Fig, 8b was generated, b) Cross-section of stratigraphy from which the synthetic seismogram in Fig. 8d was generated.

CHAPTER 3: Inception, Maintenance, and Termination of Submarine Channels

Abstract

Channels are a key component of submarine fan morphology, and their deposits are critical architectural elements of deep-water strata. Submarine channels guide fan forming turbidity currents that influence the surface dynamics that construct submarine fans in deep-water settings on continental slopes and abyssal plains. Modern observations of seafloor bathymetry, seismic data, and outcrops point to an array of submarine channel shapes including meandering, distributive, and low sinuosity channels. Here we focus on distributive and low sinuosity channels and leverage a depth-average model for turbidity currents to explore controls on their inception, maintenance, and termination. We expand on previous numerical work that explored the very early stages of channel inception. We leverage the dimensionless framework from chapter 1 and test the hypotheses that bedload transport, erosion, grain size distributions, and bed cohesion set gradients in channel mobility during fan formation. We quantify emergent channel morphology including the total length of channels active on a fan at a given time and the complexity of channel branching on the fan surface using a novel computer vision algorithm. Results from this work aid stratigraphic predictions from *a priori* knowledge of boundary conditions and the inversion of paleo-hydraulics from preserved deep-water stratigraphy, which will aid the reconstruction of environmental signals.

Introduction

Submarine channels are an integral morphological element of submarine fans and the flows that craft them play an important role in ocean ecosystems by transporting sediments and nutrients into deep oceans (Meiburg and Kneller 2010, Peakall and Sumner 2015, Azpiroz-Zabala et al., 2017; Hage et al., 2019). The mobility of submarine channels in net aggradational settings can produce fans more than 100 kms in length and with thicknesses in excess of 100's of meters, especially on lower slopes (McHargue and Webb 1986; Babonneau et al., 2010; Galy et al., 2007). While initial exploration of submarine fan processes was motivated by the high quality and massive geofluid reservoirs they house (Weimer and Pettingill, 2007), recent studies highlight the geohazards they pose and their importance to the functioning of ecosystems and global climate. Channelized flows are also studied for their impact on global climate as they transport significant volumes of particulate organic matter (Galy et al., 2007; Hage et al., 2020; Cunningham et al. 2023; Talling et al., 2023). Flows confined by channels can also attain and maintain swift velocities that threaten subsea infrastructure, including subsea cables that transport the vast majority of data transferred between continents (Heezen and Ewing 1952; Carter et al., 2014; Stevenson et al., 2018; Talling et al., 2022). Channelized submarine flows also deliver microplastics into deep oceans where they threaten marine biodiversity (Kane et al., 2020; Pohl et al., 2020). Finally, channelized submarine fan deposits preserve the thickest accumulations of strata on Earth (Talling et al., 2015). This strata contains signals of paleo-environmental change, which if properly decoded could aid reconstruction of the Earth-system responses to episodes of climate change (Covault et al., 2010; Hessler and Fildani, 2019).

Like terrestrial rivers, submarine channels are bound by natural levees (Deptuck et al., 2003; Kane et al., 2007; Straub et al., 2008; Hodgson et al., 2011; Sylvester et al., 2011; Jobe et al., 2020), tend to become distributive near their terminus (Bobonneau et al., 2010; Pyles et al., 2014), can be highly sinuous (Clark et al., 1992; Peakall et al., 2000; Sylvester and Covault, 2016), and display a downslope fining trend in the size of sediment in transit (Droz et al., 1996). Both rivers and submarine channels craft large-scale landforms. In the case of a river, channelized flow entering a quiescent body of water like an ocean or a lake undergoes a spatial reduction in flow velocity, which drives net depositional conditions that craft deltas (Gilbert 1885; Davis 1889; Galloway 1975; Syvitski and Kettner, 2011; Ganti et al., 2016). In the case of submarine channels, large-scale fans result from the lateral motion of channels on continental slopes and abyssal plains (Bouma 1962; Normark 1970; Mutti and Lucchi 1978; Stow and Mayall 2000; Hodgson et al., 2006). Sediment is transported in these channels predominantly by turbidity currents, which move downslope as a function of the gravitational pull on the excess density due to entrainment of sediments (Bagnold 1962). In these settings deposition is promoted by the concave up profile of many continental margins and the entrainment of clear water into turbidity currents, which reduces current density and decelerates flows (Parker et al., 1986, Sequeiros et al., 2009). Submarine channel levees are much thicker than their terrestrial river cousins and can be as tall as the channels are deep (Damuth et al., 1988; Kostic and Parker 2006; Mohrig and Buttles 2007; Straub and Mohrig 2008; Talling et al., 2015; de Leeuw et al., 2018; Jobe et al., 2020).

Subsurface and outcrop studies have quantified channelized submarine fan deposits (Clark et al., 1992; Gardner et al., 2000; Abreu et al., 2003; Deptuck et al., 2003; Bobonneau et al., 2010). However, such studies provide limited insight into the inception and dynamics of submarine channels. To complement these static measurements, several research campaigns collected and analyzed active flow data in submarine channels (Azpiroz-Zabala et al., 2017; Hughes Clarke 2016; Simmons et al., 2020; Pope et al., 2022). While important for understanding the flow dynamics over event timescales, most of these campaigns have yet to collect data over sufficient durations to characterize the morphodynamics of fans that dictate the resulting stratigraphic architecture. Attempts to study these processes at laboratory scale with physical experiments have generally been unable to produce self-formed channels from flows that are unequivocally turbidity currents and display sufficient mobility (lateral channel migration and avulsions) to form a fully dynamic fan surface (Parsons et al., 2002, Rowland et al., 2010; Cantelli et al., 2011).

Several studies point out that submarine channel initial confinement is generally linked to an initial phase of erosion or deposition from turbidity currents (Kostic and Parker 2006; Eggenhuisen et al., 2011 Fildani et al., 2013; De Leeuw et al., 2016). Here we highlight the work of De Leeuw et al. (2016) who were able to produce a self-formed channel at a laboratory scale. This study showed that turbidity currents can self-channelize both by erosion and deposition from suspended load. However, the length of the emergent channel was less than 10 times its width and the experiment did not extend to timescales necessary to quantify channel migration rates or observe avulsions. As such even this seminal study explored a limited range of morphodynamic conditions necessary for maintenance of submarine channels.

Given the difficulty of collecting data that is of sufficient duration to explore the process of submarine channel initiation, maintenance and termination, the community leverages numerical models. Research in this area accelerated after the publication of the seminal governing depth-average equations for turbidity currents from RANS equations (Reynolds 1895; Parker et al., 1986). Two early studies that successfully achieved channel shapes used a numerical model with the depth-average equations for turbidity currents (Bradford 1996; Imran et al., 1998). The emergent channels in these studies did not avulse or craft stacked morphologies that are observed on modern examples of seafloor fans. The limited duration explored with these models was due to computational constraints at the time. Further both studies only simulated supercritical ($Fr_D > 1$) currents, and the model used lacked important processes such as, bedload transport, development of bed cohesion, flocculation of in-transit clay particles, and transport of polydisperse grain sizes. Halsey and Kumar, (2019) used a model, EMstrata, that also leverages the depth-average governing equations for turbidity currents. This study produced channels, but the simulations lacked bedload transport and were not run long enough to create a dynamic submarine fan surface.

Other computationally efficient models rely on reduced complexity formulations of the underlying physics of gravity flows in conjunction with rules-based algorithms that approximate sediment transport fields and turbidity current dynamics (Teles et al., 2016; Burgess et al., 2019). While these models are efficient in generating geologically realistic and gross-scale depositional behaviors, such as compensational stacking of lobe complex geobodies over an antecedent surface, they do not generate channels or account for erosion by a turbidity current and therefore are limited to unchannelized and purely depositional submarine fan deposits (Burgess et al., 2019). Another widely used model, Dionisis flow, solves non-linear diffusion equations and as such bypasses formal treatment of fluid dynamics (Carson and Kirkby 1972; Begin 1988). While this model produces channelized stratigraphy (Hawie et al., 2018), the lack of flow dynamics prevents the exploration and quantification of the morphodynamic conditions necessary for inception and maintenance of submarine channels.

Here we also leverage EMstrata, which is based on the governing depth-average equations of Parker et al. (1986). This model is parallelized and can solve for sediment fluxes in bedload and suspended load, entrainment of clear water, development of bed cohesion, and flocculation of clay sized particles in transport (Fig. 1 and see methods for more details on the model). We solve the governing equations using the finite volume method that accounts for any emerging discontinuity in turbidity currents, such as the dynamics found in the head of a current or due to hydraulic jumps or an avulsion (see methods). Prior work with EMstrata documents how the model produces realistic and fully dynamic submarine fan surfaces. Specifically, using this model Wahab et al. (2022) simplified critical forcing parameters, such as regional slopes and properties of sediments for turbidity currents to show that two dimensionless parameters (densimetric Froude (Fr_D) and Rouse (p) numbers) critically influence the morphology of submarine fans. Fr_D measures the ratio of inertial to gravitational forces and p weighs the ratio of sediment settling velocity to shear velocity of the flow. This dimensionless framework highlighted endmember submarine fans that are constructed by subcritical ($Fr_D < 1$), transcritical ($Fr_D \sim 1$), and supercritical ($Fr_D > 1$) flows, which closely resemble the morphologies and architecture of several modern submarine fans (see chapter 1 and 2 for more details).

We build on the Wahab et al. (2022) framework and posit that parameters such as, bedload transport, erosion, grain size distributions, and bed cohesion set gradients in channel mobility during fan formation. To test this hypothesis, we designed and ran several generations of model runs (totaling 150 model runs) and quantified emergent channel network behaviors, including average length of channelization and prevalence of bifurcations on the fan surface (Table 1 and supplementary Table 1 for more details).

Results

Erosion and deposition of a monodisperse grain size:

We explore channelization on submarine fans in six generations of numerical experiments. Generations vary in the algorithms included in the solver (i.e., bedload transport, flocculation of sediment, development of bed cohesion) and the complexity of the input sediment distribution. Numerical experiments from generation 1 explored turbidity currents and the evolution of topography with a model that only accounted for deposition (eq. 3.7) and erosion (eq. 3.9) of a monodisperse grain size in suspension (Fig. 2; Supplementary Figure 7). This generation does not solve for bedload transport.

Experiments that are forced with low p and low Fr_D initiated channels but could not maintain these over the duration of the experiment and eventually transitioned into unchannelized sheet flows (Fig. 3a-b and see case 1-2,6-8,11-14,16-19,21-24 in Supplementary Figure 7). For models that share a constant input p, increasing Fr_D past criticality (~1) inhibits flows from crafting channels that can migrate and avulse, as deposition is limited to production of levees (Fig, 2 and see case 4,5,9,10,15,20,25 In Supplementary Figure 7). Further, we observe that the location where flows lose confinement and transition into unchannelized sheet flow is tied to the input p.

For experiments that share a constant Fr_D, decreasing p improves the ability of flows to self-channelize. Here, we note that as p decreases, for experiments with high Fr_D (> 1), the spreading angle of the flow increases downstream of the inlet channel. This suggests that such conditions have low capacity to self-channelize (se case 5,10,15, 25 in Supplementary Figure 7). The longest channel with well-defined levees in generation 1 resulted from a model that was forced with a transcritical Fr_D (~1) and low p (see case 3 In Supplementary Figure 7). In this experiment sediments bypassed the proximal portion of a self-formed channel with no in-channel deposition. Sediments were then deposited at a channel to lobe transition (Fig. 2 and case 3 in Supplementary Figure 7). All experiments in this generation lacked lateral channel mobility and sufficient in-channel aggradation to setup avulsions. As a result, all experiments in this generation failed to develop a dynamic fan surface.

Erosion, deposition, and bedload transport of a monodisperse gain size distribution: The model for generation 2 experiments is identical to generation 1, except for the implementation of bedload transport via eq. 3.12 (Fig. 4-5; Supplementary Figure 8). Channels that emerged in these experiments maintained their form as the channel bed aggraded and migrated until an avulsion was triggered, which resulted in the formation of new channels (Fig. 5 a-b, Supplementary Figure 8). The only experiments that did not generate dynamic channels were forced by supercritical Fr_D (>1) and mostly low p (see case 3-5, 7-10, 13-15, 19-20, 25 in Supplementary Figure 8).

As the Fr_D increased to 1, for experiments that share the same input p, channel lengths increased. Further increase in Fr_D into supercritical territory resulted in channels formed through the development of levees, but no in-channel deposition (Fig. 4. And Supplementary

Figure 8). Here we note that dynamic channels (i.e., channels that avulsed, bifurcated, or were lateral mobile) only emerged in experiments that were forced with subcritical Fr_D (< 1.0). In these experiments, flows are generally net depositional and construct multiple self-formed channels bound by prominent levees. Distributive networks emerge as channel bifurcations developed (see case 1-2, 5-6, 11-12, 16-18, in Supplementary Figure 8). In this generation, experiments forced with near critical Fr_D (~1) produced the longest channels. These channels are bound by well-formed levees that prograded through time, in some cases outside of the experimental domain (see case 3, 8, 13 in Supplementary Figure 8), which prevented avulsions.

As p increases, for experiments that share the same Fr_D, the length of channels generally decrease (Supplementary Figure 8). Similar to generation 1, as p decreases for supercritical experiments, the flow spreading angle increases downslope of the inlet channel, which reduces the likelihood of channel development (see case 4-5,9-10,15,20,25 in Supplementary Figure 8). Further, we observe that traversing the regime space in generation 2 from low Fr_D and p toward high Fr_D and p, corresponds with an increase in channel incision, and a reduction in channel mobility (i.e., no avulsions).

Erosion, deposition, and bedload transport of a polydisperse grainsize distribution:

The models for generations 3 and 4 are identical to generation 2, except that they solved for erosion and bedload transport of a polydisperse grain size distribution (Fig. 6-7 and Supplementary Figure 9-10). We conduct experiments with a total of 20 grain sizes, implementing a uniform size distribution in generation 3 and a log-normal distribution in generation 4. The median grain size is computed as function of the settling velocity of the suspended sediments via choice of a p (eq. 3.8). The lower bound of this distribution is set by a clay particle size of 5 um and the upper bound (d_{99}) is computed, such that the average settling velocity of the mixture is consistent with the input p (see methods). The majority of the experiments in generations 3 and 4 formed channels that were mobile and produced dynamic fan surfaces. The lone exceptions were experiments with supercritical Fr_D and low p (see Fig. 6-7 and Supplementary Figure 9-10), which also had high shear velocities, were generally net erosional, and efficient bypassed fine sediments out the distal edge of the model domain.

In experiments with a polydisperse sediment size distribution (either uniform or log-normal), we observe similar trends in channel initiation and maintenance. Given constant p, we find that increasing Fr_D generally leads to net erosional flows and a decrease in channel mobility. In experiments where the Fr_D is kept constant, increasing p leads to net depositional flows and relatively short channels. The spreading angle of flows downstream of the entrance channel, for high Fr_D, are generally less when forced with a log-normal particle size distribution (compare cases 4-5,9-10,15,20 in Supplementary Figure 9 and 10). Further, we note that for the same Fr_D and p, experiments forced with a uniform distribution of sediment sizes produced the longest channels, and consequentially the largest dynamic submarine fan surfaces (compare Supplementary Figure 9 and 10).

Erosion, deposition, and bedload transport of a polydisperse grainsize distribution accounting for flocculation of clay particles and bed cohesion:

The models for generations 5 and 6 are like generation 3 and 4, except in both generations we solve for flocculation of clay particles and bed cohesion via equations 3.15 and 3.18.

These experiments produced similar channel dynamics as those seen in generations 3 and 4. (Fig. 8-9 and Supplementary Figure 11-12). The inclusion of flocculation and bed cohesion do not significantly change conditions necessary for channel initiation or the migration dynamics and as such the morphology of the fans are not significantly different from those in generation 3 and 4. Differences we did note, which result from modeling flocculation and bed cohesion, include fan fronts and lobes that grew thicker and more laterally extensive for supercritically forced experiments in generations 5 and 6, compared to generations 3 and 4.

Prevalence of bifurcations and length of channel networks:

We leverage novel computer vision algorithms (see methods for more details) to quantify emergent channel network complexity, including average length of channel networks and prevalence of bifurcations on the fan surface. Here we restrict our calculations to generation 2, generation 3, and generation 4 runs only (Fig. 10 a-b). Generation 1 failed to channelize in the majority of the experiments and generation 5 and 6 did not present significant difference in channel initiation and migration dynamics to those present in generations 3 and 4. Further, runs in generation 2, 3 and 4 that did not craft a dynamic fan surface are also excluded from this. Numerical experiments that did form a dynamic submarine fan surface, either via avulsion or bifurcating channels in generation 2-4, show similar gradients in Fr_D and p space for number of channel bifurcations total network length (Fig. 10 a-b). Given experiments with constant p, increasing Fr_D generally leads to fewer bifurcations and shorter channels. Number of channel bifurcations and length of channelization also decrease for experiments with constant Fr_D but increasing p at the inlet. Traversing the regime space diagonally from high Fr_D and p to low Fr_D and p, corresponds to an increase in the number of channel bifurcations and length of channelization.

Discussion

Influence of Fr_D and p on the shape of channels and channel networks:

A critical aspect of this study is the exploration of an inlet Fr_D and p on the shape of channels and the networks they formed. Thus, the model generations produced included experiments that spanned a range of these dimensionless parameters (Supplementary table 1). This range and the rules deployed resulted in overlap between some of our models and the conditions and rules used in previous studies that explored submarine channel development in numerical experiments (Bradford 1996; Imran et al., 1998; Halsey and Kumar 2019). However, given the numerical methods employed in EMStrata and advancements in compute power, we can solve the evolution of submarine fans over much longer timescales than these earlier studies. These longer run times allowed channels to grow, bifurcate, and avulse as fans grew (Fig. 3-9). A key difference in this study to previous numerical campaigns is the inclusion of subcritical flow conditions, which generally did not channelize in earlier studies that lacked algorithms for bedload transport (Bradford 1996; Imran et al., 1998). While differences exist between experiments that share a constant Fr_D and p, but are from different generations, we do note some general trends. First, we explore the impact of increasing Fr_D in experiments that share the same p. Low Fr_D flows tend to produce the most complex networks, with more frequent bifurcations (Fig. 10a); supplementary figure 8-12). This is likely due to the low inertia of these flows, which results in high spatial flow deceleration and thus complex patterns of deposition that can nucleate bifurcations (Hay 1982; Imran et al. 1998; Halsey and Kumar 2019). As Fr_D increases towards criticality, channels tend to elongate and the frequency of bifurcations drops as flow inertial increases and spatial deceleration decreases, driving longer particle advection scales (Fig. 3-9; supplementary figure 8-12). This trend continues until flows have so much inertia at high Fr_D that sediment dominantly bypasses the domain, with only limited channel development due to proximal levee deposition (Halsey and Kumar 2019). Migrating through the regime diagrams along an axis with constant Fr_D but increasing p results in channels that are shorter and less complex (i.e., fewer total bifurcations; Fig. 10a-b; supplementary figure 8-12). The decrease in channel length is a result of transporting coarser sediment as p increases (Fig. 10b). These coarser grains are harder to advect long distances before deposition (Ganti et al., 2018), thus shutting down channel extension by levee progradation.

The influence of bedload in suspended load dominated flows:

The largest change in fan morphology, due to algorithms included in a model generation, came from either the inclusion or exclusion of bedload transport (eq 3.12) (Kumar and Zaretskiy et al., 2019). This might be surprising, given that turbidity currents by definition transport most of their sediment in suspension (Bagnold 1962). This suspended load gives turbidity currents their excess density and moves the center of mass of this driving gravitational force away from the bed (Sequeiros 2010a), which further enhances transport rates. The fraction of sediment transported via turbidity currents in the form of bedload is poorly constrained, but one experimental study quantified it at less than 10^{-4} (Straub et al., 2008). It is reasonable to assume that this value is generally less than 1% for field scale conditions. While bedload is a small fraction of the total load in turbidity currents, evidence for the importance of bedload transport can be found in bedforms covering modern channel beds and preserved in the rock record (Rijn et al., 1984; Nelson et al., 1995; Fedele et al.

2016). A link between bedload transport in turbidity currents and the development of bedforms was made by Sequeiros et al. (2010b), who found important dynamic feedbacks between bedforms and the hydraulics of turbidity currents. However, the importance of bedload on channel and channel network development has to our knowledge not been quantified. The importance of bedload on channel form and channel network structure has extensively been studied in the terrestrial (see Church, 2006 and references therein). This work highlights that the short transport lengths associated with bedload transport lead to frequent bed elevation adjustments, even if the overall sediment transport rates are low. In contrast, sediment traveling in suspension typically travels down system many channel widths between bed exchange events [Bagnold 1962; Ganti et al., 2018]. This infrequent bed interaction reduces the importance of this mechanism of transport to the morphology of alluvial networks. Our results suggest a similar importance of bedload transport for the maintenance of submarine channels and the morphology of their networks.

We note that earlier numerical studies on the conditions necessary to initiate submarine channels did not include algorithms for bedload transport (Bradford 1996; Imran et al., 1998; Halsey and Kumar 2019). Some of the conditions explored in these earlier studies are reproduced in our generation 1 models (Table 1; Fig. 2 and supplementary figure 7). For example, the channel forms that develop from supercritical (Fr_D >1) flows in generation 1 (Fig. 2) craft similar channel forms as seen in the modeling studies of Imran et al. (1998) and Bradford (1996). At subcritical (Fr_D <1) and transcritical (Fr_D~1) flows, channels that did develop early in the simulations failed to maintain confinement for any significant duration (Fig. 2-3). The deposition that occurred from suspension fallout in these models was generally patchy and highly heterogenous, which led to topography characterized by small length scale roughness (Fig. 3a-b). This rough surface topography tends to facilitate flow acceleration and erosion where the gradients are steep and deposition where gradients are low (Inman et al., 1976; Stacey and Bowen 1988; Sequeiros et al., 2009). However, the highly transient nature of these topographic highs and lows on the fan surface hindered the ability of incoming flows to maintain channel forms (Fig. 3b). The occasional long channels that are seen in generation 1 develop where deposition from suspended load is suppressed due to low input *p,* typically linked to fine sediments (Fig. 2 and see case 3 in supplementary figure 7). In such experiments, the flow can keep the majority of their sediments in suspension avoiding the development of transient topographic instabilities. This result indicates that while submarine channels can form from deposition and erosion of a single grain size in suspension, they cannot be maintained for subcritical (Fr_D <1) and transcritical ($Fr_D \sim 1$) flow conditions (Fig. 2, Fig. 3a-b) without the inclusion of a bedload flux algorithm.

We find that inclusion of a bedload flux algorithm is important for both channel initiation and maintenance (eq. 3.12; Fig.4-5 and supplementary figure 8). Regarding channel initiation, inclusion of a bedload flux algorithm is tied to development of scours, as gradients in bedload flux develop over minor bed roughness elements. This helps to nucleate channels and drive channel extension through bed scour through a positive feedback loop (Covault et al., 2014; Hamilton et al., 2015; Rowland et al., 2010). As channels extend and channel slopes decrease, mouthbar deposition initiates primarily due to high spatial gradients in bedload fluxes, which drives channel bifurcation and the development of complex networks. Eventually channel extension lowers slopes to such a degree that significant deposition at a channel-lobe transition triggers in-bed aggradation, again largely resulting from spatial gradients in bedload, which ultimately results in channel avulsion. All these dynamics come about in a model that is layer averaged and thus cannot produce dunes and bars that result from the vertical flow structure. We imagine that these bed and bar forms would only increase spatial gradients in bedload fluxes in real world systems, thus enhancing the importance of bedload to the development of submarine fans. Further, bedload transport is critical in migration dynamics of submarine channels (Sanders and Middelton 1965; Das et al., 2004; Sequeiros et al., 2010; Kane et al., 2010; Hamilton et al., 2017). For example, the migration of sinuous channels are critically linked to erosion along cutbanks and transport of this material near the bed to the inner banks of bends (Abad et al., 2011). Taken as a whole, our results hint towards the universal importance of bedload transport to the morphology of channels and the structure of channel networks, whether in subaerial or submarine settings.

Secondary controls on the morphodynamics of submarine channel networks:

While the inclusion of a bedload flux algorithm was the single most important variable explored for channel and channel network development, quantifiable differences did result from the class of grain size distribution implemented and to a lesser extent the inclusion of flocculation and bed cohesion algorithms (Table 1; supplementary Figure 1-2). We note that complex and polydisperse distributions of sediments in transport reduced the downstream extension of channels and the resulting planform size of submarine fans (Fig. 6-9, Supplementary Fig. 9 -12). In these experiments, coarse grains settle proximally within channel fills, limiting downstream channel extension (Halsey and Kumar 2019), and the finest grains in transport bypass channel tips, resulting in sheet-like pro-channel mud aprons. Here we note that channel lengths were usually greater in experiments forced with a uniform sediment size distribution compared to a lognormal grain size distribution (compare experiments in Fig. 7-8). More fine grains are incorporated in the uniform distribution, which helps flows maintain their driving force via sediment suspension and therefore achieve longer downstream extension (compare experiments in supplementary Figure 9 and 10). Experiments with a single grain size produced the longest channels in this study (Fig. 4, Fig, 10b and supplementary Figure 8). Such flow tends to keep that single grain size in suspension within the channel, with deposition primarily occurring on levees as the flow decelerates from lateral spreading. This works to stabilize channels as deposition on levees and in far-field sites lengthens the time between avulsions that are setup due to channel superelevation (Jobe et al. 2020) or channel back-filling (Hamilton et al., 2017). As a result, channels can prograde, sometimes out of the model domain (Fig. 4, Supplementary Fig. 8). This result suggest that the longer submarine channel systems, some of which extend for 100's of kms, might be tied to flows that have very well sorted grain size distributions (Picot et al., 2016; Bobanneau et al., 2010).

Adding algorithms to account for flocculation (eq 3.14) and development of bed cohesion (eq 3.18) did not result in clear differences in the morphology or dynamics of the channel networks (Fig. 8-9). This might partially be explained by the fact that all experiments were run with 10% mud in the sediment mixture. The lack of mud preserved in most experiments suggests that the input mud content was not sufficient to influence channel behavior, possibly because the simulated flows were efficient at eroding and bypassing mud size particles out of the simulation domain. Thus, additional runs with incrementally higher mud content in the input sediment mixture could more fully explore the influence of flocculation and cohesion on submarine channel morphodynamics.

Conclusions

We explored morphodynamic conditions for the inception, maintenance, and termination of submarine channels by leveraging a forward physics-based numerical model for turbidity currents. Results highlighted here have implications for how to model the development of submarine fans which sequester vast amounts of organic carbon [Galy et al., 2007; Hage et al., 2020; Cunningham et al. 2023; Talling et al., 2023] and house diverse ecosystems that are vulnerable to pollutants delivered by turbidity currents [Kane et al., 2020; Pohl et al., 2020]. Our results demonstrate the utility of leveraging a process-based model which accounts for important physics at play in turbidity currents and the deposits they produce, including bedload transport, the distribution of particles in transport, flocculation, and the development of bed cohesion. We highlight the following three points:

1) The inclusion (or lack thereof) of a bedload flux algorithm was the single most important choice made for the resulting morphology of submarine fans. This highlights that while the flux of sediment near the bed might be a small fraction of a turbidity current's total flux, it is critically important to crafting the texture of submarine fans.

2) Systematic changes in the length of submarine channels and the complexity of channel networks are tied to the densimetric Froude and Rouse numbers of the turbidity currents that build submarine fans.

3) The shape of a grain size distribution released into a submarine fan has secondary controls on channel length and network complexity. Here we highlight differences in modeling fan development with a single grain size vs. a distribution of sizes. Flows

characterized by single grain size (analogous to a very well sorted grain size distribution in the field) generated longer channels with less network complexity, compared to fans constructed by a distribution of grain sizes.

Methods

Numerical Model and Design

We leverage a forward and a parallel numerical model, EMstrata, that solves four depth-average equations for turbidity currents (Parker et al., 1986). These equations assume the representation of flow velocity components (u and v), concentration of sediments (c), and turbulent kinetic energy (k) as follows,

$$u(x, y, z, t) = U(x, y, t)f_u(\zeta) \quad 3.1$$

$$v(x, y, z, t) = V(x, y, t)f_v(\zeta) \quad 3.2$$

$$h(x, y, z, t) = H(x, y, t)f_h(\zeta) \quad 3.3$$

$$c(x, y, z, t) = C(x, y, t)c(\zeta) \quad 3.4$$

$$k(x, y, z, t) = K(x, y, t)f_k(\zeta) \quad 3.5$$

Where $\zeta = z/h(x, y, t)$ and h is the depth-average height of the current. The depth-average approach means that the model does not resolve vertical flow structures and processes such as flow stripped by partial confinement. Here we utilize a top hat function $f_{(u,v,h,c,k)}(\zeta)$, similar to Parker et al. (1986) to account for flows stripped by partial condiment. We note that this shape function $f_{(u,v,h,c,k)}(\zeta)$ may not accurately represent the vertical profiles of the flow variables. However, the depth average equations will in general account for their dynamic evolution in space and time. This assumption poses limitation to the ability of the model to resolve surface morphologies that are tied to the vertical flow structures, such as ripples and dunes. Recent literature has proposed more sophisticated shape functions that vary as a function of the Fr_D and p and can aid estimation of mass and momentum fluxes

(Dorrell et al. 2014). These limitations noted, EMstrata captures rich dynamics of turbidity currents and their resulting deposits with reasonable computational costs, allowing investigation of hundreds of models.

With the abovementioned assumptions, the governing equations for a 2D turbidity current driven by sediments of various sizes, can be written in following Eulerian form,

$$\frac{\partial Q}{\partial t} + \frac{\partial F}{\partial x} + \frac{\partial G}{\partial y} = S, \qquad (3.6)$$

where,

$$Q = \begin{bmatrix} h \\ hu \\ hv \\ hc_i \\ hk \\ \eta_i \end{bmatrix}, \quad F = \begin{bmatrix} hu \\ hu^2 + \frac{1}{2} gRh^2 \sum c_i \\ huv \\ huc_i \\ huk \\ q_{bi}^x \end{bmatrix}, \quad G = \begin{bmatrix} hv \\ huv \\ hv^2 + \frac{1}{2} gRh^2 \sum c_i \\ hvc_i \\ hvk \\ q_{bi}^y \end{bmatrix}.$$

The right-hand term S is defined as,

$$S = \begin{bmatrix} e_w \sqrt{u^2 + v^2} \\ -gRh(\sum c_i) \frac{\partial}{\partial x} \sum \eta_i - c_d u \sqrt{u^2 + v^2} \\ -gRh(\sum c_i) \frac{\partial}{\partial y} \sum \eta_i - c_d v \sqrt{u^2 + v^2} \\ E_i - D_i \\ P - \epsilon \\ \frac{1}{1-\emptyset} (E_i - D_i) \end{bmatrix}.$$

Here, h is the depth-average thickness of a turbidity current, u and v are velocity components in x, y directions, c_i is the volumetric concentration of i^{th} sediment type, k is the turbulent kinetic energy, η_i is the deposit thickness of i^{th} sediment, g is acceleration due to gravity (9.81 ms^{-2}), R is the relative sediment density, for quartz (1.65), $q_{bi}^x$and q_{bi}^y are bedload fluxes in x, y directions, e_w is the clear water entrainment rate, c_d is the drag coefficient and set to a value of 0.004, $E_i$is the sediment resuspension flux for the i^{th} sediment, D_i is the sediment deposition flux for the i^{th} sediment, $P - \epsilon$ are production and dissipation of turbulent kinetic energy in the fourth equation in Parker et al. (1986), and $\emptyset$ is the sediment layer porosity.

The closed system of equations in 3.6 requires additional closure terms. For entrainment of clear water into the turbidity current we use the following relationships (Parker et al., 1987),

$$e_w = \frac{0.075}{\sqrt{(1 + Ri^{2.4})}}\,, \quad Ri = \frac{1}{(Fr_D)^2} \;\; and \quad Fr_D = \frac{(u+v)}{\sqrt{Rgh\sum c_i}}$$

Where is the Ri is Richardson number, which is the inverse of the square of Fr_D. The deposition rate of the i^{th} sediment from suspension is calculated as follows,

$$D_i = r_0 c_i ws_i \qquad (3.7)$$

r_0 is computed from Garcia (1994) as,

$$r_{0i} = 0.4\left(\frac{d_i}{d_g}\right)^{1.64} + 1.64, \;\; d_g = \left(\prod_{i=1}^{n} d_i\right)^{\frac{1}{n}}$$

where d_g denotes the geometric mean size of the suspended sediment mixture. The settling velocity ws_i of the i^{th} sediment from suspension is measures using the Dietrich method (Dietrich 1982) as follows,

$$log_{10}W_* = -3.76715 + 1.92944 log_{10}d_* - 0.09815(log_{10}d_*)^2 - 0.00575(log_{10}d_*)^3$$
$$+ 0.00056(log_{10}d_*)^4, \qquad (3.8)$$

$$W_* = \frac{w_{si}^3}{Rg\nu}, \qquad d_* = \frac{Rgd_i^3}{\nu^2}$$

Where d_i is particle size and ν is the kinematic viscosity (1.5e-6m²/s). The erosion/resuspension rates are modeled as a turbulent diffusive transport as follows,

$$E_i = D_T(p_i c_{bi} - c_i)/h \qquad (3.9),$$

where D_T is the turbulent diffusivity, c_{bi} is the near bed concentration of i^{th} sediment in the eroded (fluidized) bed, and c_i is i^{th} depth average concentration of sediments. D_T is computed as follows,

$$D_T = \frac{h}{(1 + 3.33Ri)^{1.5}}\sqrt{k}$$

We use the Garcia and Parker (1991) formulation for the near bed concentration of sediments c_{bi} as follows,

$$c_{bi} = \frac{1.3 * 10^{-7} Z_i^5}{1 + \frac{1.3}{0.3} * 10^{-7} Z_i^5}, \qquad Z_i \kappa \frac{u_8}{ws_i} f(Re_{pi}) \left(\frac{d_i}{d_{50}}\right)^{0.2}$$

where d_{50} is the median grain size of the deposited sediment, $\kappa = 1 - 0.288\sigma_\phi$ accounts for the non-uniformity of the deposited sediments, and ϕ is the sorting parameter. The function $f(Re_{pi})$ is given as follows,

$$f(Re_{pi}) = \{Re_{pi}^{0.6}, if\ Re_{pi} \geq 2.34\ or\ 0.586 Re_{pi}^{1.23} m\ if\ Re_{pi} < 2.34. \qquad (3.10)$$

So, the final form of the sediment entrainment flux in eq (3.9) is computed as follows,

$$E_i = \frac{\sqrt{k}(c_{bi} - c_i)}{(1 + 3.33Ri)^{1.5}}$$

The governing equations and their closure terms are solved using a finite volume method with a dynamic time step that is a function of grid spacing, flow velocity, and wave speed. The finite volume method captures discontinuities in the turbidity current flow such as the head of the turbidity current or a hydraulic jump. Once a current is released into the domain it contains a head that propagates through the model domain and eventually exits the simulation domain. This head develops due to sharp spatial gradients in hydrostatic pressure and shear stresses between cells that have near zero velocity or concentration, and those characterizing the current front. The model then simulates the body of the current until a new head originates from a node where the system undergoes an avulsion. The amount of morphodynamic work by the head and the body of the turbidity current is controlled by empirical closures (Meyer_Peter and Müller, 1948; Garcia and Parker, 1991; Garcia 1994) that are functions of shear stresses within the flow. A more detailed description of the depth-averaged theory, governing equations and analyses of their approximate analytical solutions, and a choice of the numerical solver is published in prior studies (Halsey et al., 2017, Halsey and Kumar 2019, Wahab et al., 2022).

We design several generations of numerical experiments to explore the influence of grain size distribution, bedload transport, and cohesive sediment transport on submarine channel dynamics (Table 1; Supplementary Table 1). Within each generation that is defined by the above constraints, we also vary the flow Fr_D and p of the input flow to the simulation. 10% of the input sediment mixture is mud for all model runs. To this end, we design a model for generation 1 experiments that accounts for erosion and deposition of sediments from a mixture that contains a single grain size. All simulations in generation 1 and others described below are stopped when a defined volume of sediment is released into the simulation domain.

In generation 2, we use the same forcing criterion as above, except add an algorithm to model bedload transport. This mode of transport in turbidity currents accounts for saltation, rolling, sliding, and traction of sediments near or slightly above bed. Here we use the bedload formulation form Meyer-Peter and Müller (1948), which is given as,

$$\Phi = 3.97\ (\tau^* - \tau_c^*)\left(\sqrt{\tau^* - \tau_c^*}\right), \quad \tau_c^* = \frac{1}{2}\left(0.22 Re_p^{0.6} + 0.06 * 10^{-7 Re_p^{0.6}}\right) \qquad 3.11$$

We reformulate this equation to consider a mixture of sediments as follows,

$$q_b = \sum_i q_{bi}^{x,y} = \sum_i p_i \sqrt{Rgd_i^3 \Phi}(\tau_i^* - \tau_{ci}^*) \qquad 3.12$$

where p_i is the fraction of the i^{th} sediment in the transported layer (Kumar and Zaretskiy et al., 2019).

In generations 3 and 5, we introduce a uniform grain size distribution with 20 total sediment sizes and solve for erosion, deposition, and bedload transport (supplementary Figure 1). We compute the uniform distribution of sediments as a function of d_{50} and d_{99}. In generations 4 and 6 we introduce a log-normal distribution (supplementary Figure 2); we compute the grain size distribution as a function of the d_{50} and sorting. Here sorting is computed using the Folk criterion (Folk, 1966) as follows,

$$sorting = \frac{\emptyset_{16} + \emptyset_{84}}{4} + \frac{\emptyset_{95} - \emptyset_5}{6.6} \qquad 3.13$$

where ∅ represents grain size percentile. For both distributions, we iteratively solve for the d_{50} and d_{99}, such the settling velocity ws_i of the average grain size in the distribution is consistent with settling velocity of the Rouse number and the d_{99} does not exceed a value of 1 mm. Finally, we compute for equispaced grain diameters to achieve the final distribution of the sediment mixture.

In generations 5 and 6, we implement a model for flocculation of clay particles (Kuprenas et al., 2018, Winterwerp 1998) and a cohesive transport model (Winterwerp and Kesteren 2004), while keeping all other forcing conditions the same as generations 3 and 4. The equation for solving for a diameter of a floccule is given by Kuprenas et al., 2018 as,

$$\frac{\partial D}{\partial t} = \frac{k_A^j}{nf}\frac{D_p^{nf-3}}{\rho_s} GCD^{A-nf} - \frac{k_B^j}{nf} DG\left(\frac{D-D_p}{D_p}\right)^p \left(\frac{\tau_t}{\tau_y}\right)^q \qquad 3.14$$

where D is the diameter of the floccule, D_p is the primary clay particle size (5um), C is the mass concentration, ρ_s is the density of the primary clay particle, G = $\sqrt{\in/\nu}$ where $\in = 0.09k^{1.5}/h$, k is the turbulent energy term, $\tau_t = \mu G$ is the turbulent induced stress on the floc size, $\tau_y = F_y/D^2$ is the strength term for each floc size, $\mu = 0.001$ is the dynamic viscosity of the fluids, $F_y = 1e-10$ is the floc yield force, K_A is a Collison term for flocs , K_B is a term for break efficiency of flocs, and p and q are power coefficients (Winterwerp 1998). To solve for the erosion and deposition of the mud size particles, we implement the depth-average volumetric concentration (c) of mud and number density (n)of floccules as follows,

$$\frac{\partial hc}{\partial t} + \frac{\partial hcu}{\partial x} + \frac{\partial hcv}{\partial y} = -D + E \qquad (3.15)$$

$$\frac{\partial hn}{\partial t} + \frac{\partial hcnu}{\partial x} + \frac{\partial hcnv}{\partial y} = Ah + Bh - D_n + E_n \qquad (3.16)$$

where,

$$A = k_A^j G V_p \left(\frac{D}{D_p}\right)^3 n^2 , \qquad B = k_B^j G \left(\frac{D - D_p}{D_p}\right)^p \left(\frac{\mu G}{\frac{F_y}{D^2}}\right)^q n.$$

The deposition rate is computed as follows,

$$D = 2.04 v_s c \qquad (3.17)$$

where c is volumetric concentration of mud size sediments, and v_s is the settling velocity of floccules. The diameter of the floc is calculated from n and c using the following equation,

$$D = \left(\frac{c}{V_p n}\right)^{1/nf} D_p$$

this diameter value a settling velocity v_s is computed using eq. (3.8). The erosion and deposition rates for the floccule number density n follows

$$-D_n + E_n = -(D + E).\frac{1}{V_p}\left(\frac{D}{D_p}\right)^{-nf}$$

So, the final form of the eq. (3.16) is implemented as follows,

$$\frac{\partial hn}{\partial t} + \frac{\partial hcnu}{\partial x} + \frac{\partial hcnv}{\partial y} = \left(k_A^j G V_p \left(\frac{D}{D_p}\right)^3 n^2\right) h + \left(k_B^j G \left(\frac{D-D_p}{D_p}\right)^p \left(\frac{\mu G}{\frac{F_y}{D^2}}\right)^q n\right) h - (D + E).\frac{1}{V_p}\left(\frac{D}{D_p}\right)^{-nf} \qquad 3.18$$

Channel Tracking Criterion

We track channels once every 40 hours into each simulation. This process is carried out in several steps (supplementary Figure 3), which are described below.

Pre-processing: We track channels in each simulation using the sediment load property (hc). This property is a product of the height (h) [m] of the current and concentration (c) [1/1] of suspended sediments in the flow at any given cell [m^2]. First, we interpolate this property onto a Cartesian grid. Next, we apply an image processing algorithm that enhances the contrast in the sediment load property. We achieve this by applying a contrast-limited adaptive histogram equalization (CLAHE) on an input image (Zuiderveld 1994). This method enhances the contrast of an image by applying histogram equalization to local regions of the image, rather than the entire image at once. Next, we a apply a Gabor filter (Gabor 1946; Sahoo et al., 2018) which helps in highlighting edges, curves, and linear features of different orientations and scales. This filter is a combination of a Gaussian function and a sine or cosine wave function. By varying the orientation and frequencies, this approach highlights different types of features from the image.

Tracking: Channel tracking is initiated by defining the starting coordinates, which are set to the source coordinates of the inlet channel. We ignore tracking in the inlet channel itself, and only start this process at the inlet to main domain. For all model runs in this study, we use a minimum threshold of hc at 0.0625 i.e., 25 % of the hc value at the inlet. To track channel like features, we first compute the Hessian matrix of the sediment load property every 40 hours. The Hessian matrix is a square matrix of second-order partial derivatives of a function with respect to its variables (Duda and Hart 1973; Forsyth and Ponce 2002). This matrix is commonly used in image processing to detect and analyze features such as edges, and ridgelines (Voorn et al., 2013; Jin et al., 2021). The ridgelines resemble the morphology of branches in a tree leaf, river networks on a continent or submarine channels in deepwater settings. We compute the Hessian matrix using a Gaussian filter with a specified 2D kernel

(Jin et al., 2021; Malladi and Sethian 1995; Zhu et al., 2017). The kernel value controls the size of this filter and is used to adjust for the size of the features that are detected. We performed sensitivity analyses to choose an optimum kernel value of 12 such that it will allow detection of channels of various sizes in the simulations.

Once a channel feature is identified close to the starting point, an intensity cross-section profile of the hc property is calculated. This cross-section profile consists of uneven data points and is often noisy. We apply a low-pass Savitsky-Golay filter to smooth this profile to allow for a cleaner fit of the data in the following steps (Jardim and Morgado-Dias, 2020). The Savitsky-Golay filter smooths the noise in the cross-section profile by fitting a series of polynomial curves to the data and then uses those curves to estimate the underlying hc data. A probability density function is applied to the intensity profile of the hc cross-section to determine the total number of peaks. If there is only one peak (e.g., within a channel), then a unimodal Gaussian distribution fit is applied (Supplementary Figure 4). Conversely, if the data is defined by two peaks (e.g., at a channel bifurcation node), then a bimodal distribution Gaussian fit is applied (Supplementary Figure 5). We implement the choice of the optimal fit to the data by measuring the mean squared error (MSE) of the fit for both unimodal and bimodal Gaussian distributions. When both fits can be applied to the distribution (i.e., the MSE is not zero), we calculate the overlap coefficient of the two distributions. The value of this coefficient ranges between 0 (no overlap) and 1 (complete overlap). If the overlap coefficient is less than 0.2 (i.e., 20% overlap), the bimodal distribution is chosen because the two distributions are sufficiently different (Supplementary Figure 5). Otherwise, a unimodal distribution is chosen because it is a simpler model and there is not enough evidence to support the use of a more complex bimodal fit (Supplementary Figure 6). The peak of the model fit is then used to continue tracking the channel or the x-y coordinates of the branches. The algorithm iteratively updates the width of the hc cross-section, azimuth angle, current position of the channel centerline, and applies a Boolean mask to the region already tracked to avoid redundancy. Once the value of the peak of the distribution is smaller than then minimum predefined hc threshold the channel tracking is terminated.

Branching Criterion: We implement a minimum length threshold to keep, or prune tracked branches throughout the tracking process. This criterion is implemented to isolate instances during a model run where flow stripping occurs. Such phenomenon usually occurs over short distances. Here, we remove channel branches that are shorter than 250 m. We apply this branching criterion across all models runs irrespective of their forcing conditions.

Channel Network Statistics: We measure two statistics to quantify the distributary network structure and the degree of total channelization in model runs that are defined across a spectrum of flow forcing conditions. First, we measure the number of channel bifunctions. This metric is essentially nodes within the simulations where the sediment load property at a given x-y location is defined by a bimodal distribution (Supplementary Figure 5). At these sites the channel splits into two branches. We measure all such bifurcation points every 40 hours into the simulations for all model runs explored in this study. Finally, we computed the arithmetic mean of the measured bifurcations. Next, we compute the total length of channels in the domain every 40 hours into the simulation. This is achieved by measuring the Euclidean distance across all x and y coordinates that defines the channels and their branches. Finally, we compute the average of this length scale to quantify the degree of channelization across a model run.

References cited

Abad, J. D., Parker, G., Sequeiros, O., Spinewine, B., Garcia, M. H., & Pirmez, C. (2011, December). Flow structure in submarine meandering channels, a continuous discussion on secondary flow. In *AGU Fall Meeting Abstracts* (Vol. 2011, pp. EP53B-03).

Abreu, V., Sullivan, M., Pirmez, C., & Mohrig, D. (2003). Lateral accretion packages (LAPs): an important reservoir element in deep water sinuous channels. *Marine and Petroleum Geology*, *20*(6-8), 631-648.

Alexander, J. A. N., McLelland, S. J., Gray, T. E., Vincent, C. E., Leeder, M. R., & Ellett, S. (2008). Laboratory sustained turbidity currents form elongate ridges at channel mouths. *Sedimentology*, *55*(4), 845-868.

Azpiroz-Zabala, M., Cartigny, M. J., Talling, P. J., Parsons, D. R., Sumner, E. J., Clare, M. A., ... & Pope, E. L. (2017). Newly recognized turbidity current structure can explain prolonged flushing of submarine canyons. *Science advances*, *3*(10), e1700200.

Babonneau, N., Savoye, B., Cremer, M. & Bez, M., (2010). Sedimentary architecture in meanders of a submarine channel: detailed study of the present Congo turbidite channel (Zaiango project). Journal of Sedimentary Research **80**, 852-866.

Bagnold, R. A. (1962). Auto-suspension of transported sediment; turbidity currents. *Proceedings of the Royal Society of London. Series A. Mathematical and Physical Sciences*, *265*(1322), 315-319.

Begin, Z. E. B. (1988). Application of a diffusion-erosion model to alluvial channels which degrade due to base-level lowering. *Earth Surface Processes and Landforms*, *13*(6), 487-500.

Bouma, A. H. (1962). Sedimentology of some flysch deposits. *Agraphic approach to facies interpretation*, *168*.

Bradford, S. F. (1996). *Numerical modeling of turbidity current hydrodynamics and sedimentation*. University of Michigan.

Burgess, P. M., Masiero, I., Toby, S. C., & Duller, R. A. (2019). A big fan of signals? Exploring autogenic and allogenic process and product in a numerical stratigraphic forward model of submarine-fan development. *Journal of Sedimentary Research*, *89*(1), 1-12.

Cantelli, A., Pirmez, C., Johnson, S., & Parker, G. (2011). Morphodynamic and stratigraphic evolution of self-channelized subaqueous fans emplaced by turbidity currents. *Journal of Sedimentary Research*, *81*(3), 233-247.

Carson, M. A., & Kirkby, M. J. (1972). Hillslope form and process. Cambridge Geographical studies no.3., 475, p. 195

Carter, L., Gavey, R., Talling, P. J., & Liu, J. T. (2014). Insights into submarine geohazards from breaks in subsea telecommunication cables. *Oceanography*, *27*(2), 58-67.

Clark, J. D., Kenyon, N. H., & Pickering, K. T. (1992). Quantitative analysis of the geometry of submarine channels: implications for the classification of submarine fans. *Geology*, *20*(7), 633-636.

Covault, J. A., & Graham, S. A. (2010). Submarine fans at all sea-level stands: Tectono-morphologic and climatic controls on terrigenous sediment delivery to the deep sea. *Geology*, *38*(10), 939-942.

Covault, J. A., Kostic, S., Paull, C. K., Ryan, H. F., & Fildani, A. (2014). Submarine channel initiation, filling and maintenance from sea-floor geomorphology and morphodynamic modelling of cyclic steps. *Sedimentology*, *61*(4), 1031-1054.

Cunningham, C. M., Ruso, S. F., & Arnott, R. W. C. (2023). Controls on the stratigraphic distribution of organic carbon in ancient deep-marine levees. *Marine and Petroleum Geology*, *148*, 106039.

Damuth, J. E., Flood, R. D., Kowsmann, R. O., Belderson, R. H., & Gorini, M. A. (1988). Anatomy and growth pattern of Amazon deep-sea fan as revealed by long-range side-scan sonar (GLORIA) and high-resolution seismic studies. *AAPG bulletin*, *72*(8), 885-911.

Das, H. S., Imran, J., Pirmez, C., & Mohrig, D. (2004). Numerical modeling of flow and bed evolution in meandering submarine channels. *Journal of Geophysical Research: Oceans*, *109*(C10).

Davis, W. M. (1889). The rivers and valleys of Pennsylvania: National Geographic Society.

De Leeuw, J., Eggenhuisen, J. T., & Cartigny, M. J. (2016). Morphodynamics of submarine channel inception revealed by new experimental approach. *Nature communications*, *7*(1), 1-7.

de Leeuw, J., Eggenhuisen, J. T., & Cartigny, M. J. (2018). Linking submarine channel–levee facies and architecture to flow structure of turbidity currents: insights from flume tank experiments. *Sedimentology*, *65*(3), 931-951.

Deptuck, M. E., Steffens, G. S., Barton, M., & Pirmez, C. (2003). Architecture and evolution of upper fan channel-belts on the Niger Delta slope and in the Arabian Sea. *Marine and Petroleum Geology*, *20*(6-8), 649-676.

Dietrich, W. E. (1982). Settling velocity of natural particles. *Water resources research*, *18*(6), 1615-1626.

Dorrell, R. M., Darby, S. E., Peakall, J., Sumner, E. J., Parsons, D. R., & Wynn, R. B. (2014). The critical role of stratification in submarine channels: implications for channelization and long runout of flows. Journal of Geophysical Research: Oceans, 119(4), 2620-2641.

Droz, L., Rigaut, F., Cochonat, P., & Tofani, R. (1996). Morphology and recent evolution of the Zaire turbidite system (Gulf of Guinea). *Geological Society of America Bulletin*, *108*(3), 253-269.

Duda, R. O., & Hart, P. E. (1973). Pattern recognition and scene analysis. New York:Wiley.

Eaton, B. C., Church, M., & Davies, T. R. (2006). A conceptual model for meander initiation in bedload-dominated streams. *Earth Surface Processes and Landforms: The Journal of the British Geomorphological Research Group*, *31*(7), 875-891.

Edmonds, D. A., & Slingerland, R. L. (2008). Stability of delta distributary networks and their bifurcations. *Water Resources Research*, *44*(9).

Eggenhuisen, J. T., McCAFFREY, W. D., Haughton, P. D., & Butler, R. W. (2011). Shallow erosion beneath turbidity currents and its impact on the architectural development of turbidite sheet systems. *Sedimentology*, *58*(4), 936-959.

Fedele, J., Hoyal D., Barnaal, Z., Tulenko, J., Awalt, S., (2016). Bedforms Created by Gravity Flows", Autogenic Dynamics and Self-Organization in Sedimentary Systems, David A. Budd, Elizabeth A. Hajek, Sam J. Purkis

Fildani, A., Hubbard, S. M., Covault, J. A., Maier, K. L., Romans, B. W., Traer, M., & Rowland, J. C. (2013). Erosion at inception of deep-sea channels. *Marine and Petroleum Geology*, *41*, 48-61.

Fildani, A., Normark, W. R., Kostic, S., & Parker, G. (2006). Channel formation by flow stripping: Large-scale scour features along the Monterey East Channel and their relation to sediment waves. *Sedimentology*, *53*(6), 1265-1287.

Folk, R. L. (1966). A review of grain-size parameters. *Sedimentology*, *6*(2), 73-93.

Forsyth, D. A., & Ponce, J. (2002). *Computer vision: a modern approach*. prentice hall professional technical reference.

Gabor, D. (1946). Theory of communication. Part 1: The analysis of information. *Journal of the Institution of Electrical Engineers-part III: radio and communication engineering*, *93*(26), 429-441.

Galloway, W. D, 1975. in *Deltas, Models for Exploration* (ed. Broussard, M. L.) 86–98 (Houston)

Galy, V., France-Lanord, C., Beyssac, O., Faure, P., Kudrass, H., & Palhol, F. (2007). Efficient organic carbon burial in the Bengal fan sustained by the Himalayan erosional system. *Nature*, *450*(7168), 407-410.

Ganti, V., Chadwick, A. J., Hassenruck-Gudipati, H. J., & Lamb, M. P. (2016). Avulsion cycles and their stratigraphic signature on an experimental backwater-controlled delta. *Journal of Geophysical Research: Earth Surface*, *121*(9), 1651-1675.

Ganti, V., Lamb, M. P., & McElroy, B. (2014). Quantitative bounds on morphodynamics and implications for reading the sedimentary record. *Nature communications*, *5*(1), 3298.

Garcia, M. H. (1994). Depositional turbidity currents laden with poorly sorted sediment. *Journal of hydraulic engineering*, *120*(11), 1240-1263.

Garcia, M., & Parker, G. (1991). Entrainment of bed sediment into suspension. *Journal of Hydraulic Engineering*, *117*(4), 414-435.

Gardner, M. H., Borer, J. M., Bouma, A. H., & Stone, C. G. (2000). Submarine channel architecture along a slope to basin profile, Brushy Canyon Formation, west Texas. *SPECIAL PUBLICATION-SEPM*, *68*, 195-214.

Gilbert, G. K. (1885). *The topographic features of lake shores*. US Government Printing Office.

Hage, S., Cartigny, M. J., Sumner, E. J., Clare, M. A., Hughes Clarke, J. E., Talling, P. J., ... & Watts, C. (2019). Direct monitoring reveals initiation of turbidity currents from extremely dilute river plumes. *Geophysical Research Letters*, *46*(20), 11310-11320.

Hage, S., Galy, V. V., Cartigny, M. J. B., Acikalin, S., Clare, M. A., Gröcke, D. R., ... & Talling, P. J. (2020). Efficient preservation of young terrestrial organic carbon in sandy turbidity-current deposits. *Geology*, *48*(9), 882-887.

Halsey, T. C., & Kumar, A. (2019). Levees Formed by Turbidity Currents: A Depth-Averaged Modeling Treatment. *Journal of Geophysical Research: Oceans*, *124*(7), 4389-4415.

Halsey, T. C., Kumar, A., & Perillo, M. M. (2017). Sedimentological regimes for turbidity currents: Depth-averaged theory. *Journal of GEOPHYSICAL research: Oceans*, *122*(7), 5260-5285.

Hamilton, P. B., Strom, K. B., & Hoyal, D. C. (2015). Hydraulic and sediment transport properties of autogenic avulsion cycles on submarine fans with supercritical distributaries. *Journal of Geophysical Research: Earth Surface*, *120*(7), 1369-1389.

Hamilton, P., Gaillot, G., Strom, K., Fedele, J., & Hoyal, D. (2017). Linking hydraulic properties in supercritical submarine distributary channels to depositional-lobe geometry. *Journal of Sedimentary Research*, *87*(9), 935-950.

Hawie, N., Covault, J. A., Dunlap, D., & Sylvester, Z. (2018). Slope-fan depositional architecture from high-resolution forward stratigraphic models. *Marine and Petroleum Geology*, *91*, 576-585.

Hay, A.E. (1982). The effects of submarine channels on river tailings disposal, in Marine Tailings Disposal, pp. 139-181, Butterworth-Heinemann, Newton, Mass.

Heezen, B. C., & Ewing, W. M. (1952). Turbidity currents and submarine slumps, and the 1929 Grand Banks [Newfoundland] earthquake. *American journal of Science*, *250*(12), 849-873.

Hessler, A. M., & Fildani, A. (2019). Deep-sea fans: Tapping into Earth's changing landscapes. *Journal of Sedimentary Research*, *89*(11), 1171-1179.

Hodgson, D. M., Di Celma, C. N., Brunt, R. L., & Flint, S. S. (2011). Submarine slope degradation and aggradation and the stratigraphic evolution of channel–levee systems. *Journal of the Geological Society*, *168*(3), 625-628.

Hodgson, D. M., Flint, S. S., Hodgetts, D., Drinkwater, N. J., Johannessen, E. P., & Luthi, S. M. (2006). Stratigraphic evolution of fine-grained submarine fan systems, Tanqua depocenter, Karoo Basin, South Africa. *Journal of sedimentary Research*, *76*(1), 20-40.

Hughes Clarke, J. E. (2016). First wide-angle view of channelized turbidity currents links migrating cyclic steps to flow characteristics. *Nature communications*, *7*(1), 11896.

Imran, J., Parker, G., & Katopodes, N. (1998). A numerical model of channel inception on submarine fans. *Journal of Geophysical Research: Oceans*, *103*(C1), 1219-1238.

Inman, D. L., Nordstrom, C. E., & Flick, R. E. (1976). Currents in submarine canyons: An air-sea-land interaction. *Annual Review of Fluid Mechanics*, *8*(1), 275-310.

Jardim, R., & Morgado-Dias, F. (2020). Savitzky–Golay filtering as image noise reduction with sharp color reset. *Microprocessors and Microsystems*, *74*, 103006.

Jin, S., Liu, Y., Fagherazzi, S., Mi, H., Qiao, G., Xu, W., ... & Fichot, C. G. (2021). River body extraction from sentinel-2A/B MSI images based on an adaptive multi-scale region growth method. *Remote Sensing of Environment*, *255*, 112297.

Jobe, Z. R., Howes, N. C., Straub, K. M., Cai, D., Deng, H., Laugier, F. J., ... & Shumaker, L. E. (2020). Comparing aggradation, superelevation, and avulsion frequency of submarine and fluvial channels. *Frontiers in Earth Science*, *8*, 53.

Kane, I. A., Clare, M. A., Miramontes, E., Wogelius, R., Rothwell, J. J., Garreau, P., & Pohl, F. (2020). Seafloor microplastic hotspots controlled by deep-sea circulation. Science, 368(6495), 1140-1145.

Kane, I. A., Kneller, B. C., Dykstra, M., Kassem, A., & McCaffrey, W. D. (2007). Anatomy of a submarine channel–levee: an example from Upper Cretaceous slope sediments, Rosario Formation, Baja California, Mexico. *Marine and Petroleum Geology*, *24*(6-9), 540-563.

Kane, I. A., McCaffrey, W. D., Peakall, J., & Kneller, B. C. (2010). Submarine channel levee shape and sediment waves from physical experiments. *Sedimentary Geology*, *223*(1-2), 75-85.

Kleinhans, M. G., Ferguson, R. I., Lane, S. N., & Hardy, R. J. (2013). Splitting rivers at their seams: bifurcations and avulsion. *Earth surface processes and landforms*, *38*(1), 47-61.

Kostic, S., & Parker, G. (2006). The response of turbidity currents to a canyon–fan transition: internal hydraulic jumps and depositional signatures. *Journal of Hydraulic Research*, *44*(5), 631-653.

Kumar, A., & Zaretskiy, Y. (2019). *U.S. Patent Application No. 16/191,528*.

Kuprenas, R., Tran, D., & Strom, K. (2018). A shear-limited flocculation model for dynamically predicting average floc size. *Journal of Geophysical Research: Oceans*, *123*(9), 6736-6752.

Maier, K. L., Fildani, A., Paull, C. K., McHargue, T. R., Graham, S. A., & Caress, D. W. (2013). Deep-sea channel evolution and stratigraphic architecture from inception to abandonment from high-resolution autonomous underwater vehicle surveys offshore central California. *Sedimentology*, *60*(4), 935-960.

Malladi, R., & Sethian, J. A. (1995). Image processing via level set curvature flow. *proceedings of the National Academy of sciences*, *92*(15), 7046-7050.

McHargue, T. R., & Webb, J. E. (1986). Internal geometry, seismic facies, and petroleum potential of canyons and inner fan channels of the Indus submarine fan. *AAPG bulletin*, *70*(2), 161-180.

Meiburg, E., & Kneller, B. (2010). Turbidity currents and their deposits. *Annual Review of Fluid Mechanics*, *42*, 135-156.

Meyer-Peter, E., & Müller, R. (1948). Formulas for bed-load transport. In IAHSR 2nd meeting, Stockholm, appendix 2. IAHR.Aki, K. and Richards, P.G, 2002, Quantitative Seismology, University Science Books, Mohrig, D., & Buttles, J. (2007). Deep turbidity currents in shallow channels. *Geology*, *35*(2), 155-158.

Mutti, E., & Ricci Lucchi, F. (1978). Turbidites of the northern Apennines: introduction to facies analysis. *International geology review*, *20*(2), 125-166.

Nelson, J. M., Shreve, R. L., McLean, S. R., & Drake, T. G. (1995). Role of near-bed turbulence structure in bed load transport and bed form mechanics. *Water resources research*, *31*(8), 2071-2086.

Normark, W. R. (1970). Growth patterns of deep-sea fans. *AAPG bulletin*, *54*(11), 2170-2195.

Parker, G., Fukushima, Y., & Pantin, H. M. (1986). Self-accelerating turbidity currents. *Journal of Fluid Mechanics*, *171*, 145-181.

Parker, G., Garcia, M., Fukushima, Y., & Yu, W. (1987). Experiments on turbidity currents over an erodible bed. *Journal of Hydraulic Research*, *25*(1), 123-147.

Parsons, J. D., Schweller, W. J., Stelting, C. W., Southard, J. B., Lyons, W. J., & Grotzinger, J. P. (2002). A preliminary experimental study of turbidite fan deposits. *Journal of Sedimentary Research*, *72*(5), 619-628.

Peakall, J., & Sumner, E. J. (2015). Submarine channel flow processes and deposits: A process-product perspective. *Geomorphology*, *244*, 95-120.

Peakall, J., McCaffrey, B., & Kneller, B. (2000). A process model for the evolution, morphology, and architecture of sinuous submarine channels. *Journal of Sedimentary Research*, *70*(3), 434-448.

Picot, M., Droz, L., Marsset, T., Dennielou, B., & Bez, M. (2016). Controls on turbidite sedimentation: Insights from a quantitative approach of submarine channel and lobe architecture (Late Quaternary Congo Fan). *Marine and Petroleum Geology*, *72*, 423-446.

Pohl, F., Eggenhuisen, J. T., Kane, I. A., & Clare, M. A. (2020). Transport and burial of microplastics in deep-marine sediments by turbidity currents. Environmental science & technology, 54(7), 4180-4189.

Pope, E. L., Cartigny, M. J., Clare, M. A., Talling, P. J., Lintern, D. G., Vellinga, A., ... & Vendettuoli, D. (2022). First source-to-sink monitoring shows dense head controls sediment flux and runout in turbidity currents. Science Advances, 8(20), eabj3220.

Porcile, G., Enrile, F., Besio, G., & Pittaluga, M. B. (2022). Hydrostatic vs. non-hydrostatic modelling of density currents developing two dimensionally on steep and mild slopes. *Applied Ocean Research*, *121*, 103085.

Pyles, D. R., Strachan, L. J., & Jennette, D. C. (2014). Lateral juxtapositions of channel and lobe elements in distributive submarine fans: Three-dimensional outcrop study of the Ross Sandstone and geometric model. *Geosphere*, *10*(6), 1104-1122.

Reynolds, O. (1895). IV. On the dynamical theory of incompressible viscous fluids and the determination of the criterion. *Philosophical transactions of the royal society of london.(a.)*, (186), 123-164.

Rowland, J. C., Hilley, G. E., & Fildani, A. (2010). A test of initiation of submarine leveed channels by deposition alone. *Journal of Sedimentary Research*, *80*(8), 710-727.

Sahoo, P. K., Soltani, S. A. K. C., & Wong, A. K. (1988). A survey of thresholding techniques. *Computer vision, graphics, and image processing*, *41*(2), 233-260.

Sanders, J. E., & Middleton, G. V. (1965). Primary sedimentary structures and their hydrodynamic interpretation. *Soc. Econ. Paleontologists and Mineralogists Spec. Pub. 12*, 192-219.

Savitzky, A., & Golay, M. J. (1964). Smoothing and differentiation of data by simplified least squares procedures. *Analytical chemistry*, *36*(8), 1627-1639.

Sequeiros, O. E., Naruse, H., Endo, N., Garcia, M. H., & Parker, G. (2009). Experimental study on self-accelerating turbidity currents. *Journal of Geophysical Research: Oceans*, *114*(C5).

Sequeiros, O. E., Spinewine, B., Beaubouef, R. T., Sun, T. A. O., Garcia, M. H., & Parker, G. (2010b). Bedload transport and bed resistance associated with density and turbidity currents. *Sedimentology*, *57*(6), 1463-1490.

Sequeiros, O. E., Spinewine, B., Beaubouef, R. T., Sun, T., García, M. H., & Parker, G. (2010a). Characteristics of velocity and excess density profiles of saline underflows and turbidity currents flowing over a mobile bed. *Journal of Hydraulic Engineering*, *136*(7), 412-433.

Simmons, S. M., Azpiroz-Zabala, M., Cartigny, M. J. B., Clare, M. A., Cooper, C., Parsons, D. R., ... & Talling, P. J. (2020). Novel acoustic method provides first detailed measurements of sediment concentration structure within submarine turbidity currents. *Journal of Geophysical Research: Oceans*, *125*(5), e2019JC015904.

Stacey, M. W., & Bowen, A. J. (1988). The vertical structure of turbidity currents and a necessary condition for self-maintenance. *Journal of Geophysical Research: Oceans*, *93*(C4), 3543-3553.

Stevenson, C. J., Feldens, P., Georgiopoulou, A., Schönke, M., Krastel, S., Piper, D. J., ... & Mosher, D. (2018). Reconstructing the sediment concentration of a giant submarine gravity flow. *Nature communications*, *9*(1), 2616.

Stow, D. A., & Mayall, M. (2000). Deep-water sedimentary systems: New models for the 21st century. Marine and Petroleum Geology, 17(2), 125-135.

Straub, K. M., & Mohrig, D. (2008). Quantifying the morphology and growth of levees in aggrading submarine channels. *Journal of Geophysical Research: Earth Surface*, *113*(F3).

Straub, K. M., Mohrig, D., McElroy, B., Buttles, J., & Pirmez, C. (2008). Interactions between turbidity currents and topography in aggrading sinuous submarine channels: A laboratory study. *Geological Society of America Bulletin*, *120*(3-4), 368-385.

Sylvester, Z., & Covault, J. A. (2016). Development of cutoff-related knickpoints during early evolution of submarine channels. *Geology*, *44*(10), 835-838.

Sylvester, Z., Pirmez, C., & Cantelli, A. (2011). A model of submarine channel-levee evolution based on channel trajectories: Implications for stratigraphic architecture. *Marine and Petroleum Geology*, *28*(3), 716-727.

Syvitski, J. P., & Kettner, A. (2011). Sediment flux and the Anthropocene. *Philosophical Transactions of the Royal Society A: Mathematical, Physical and Engineering Sciences*, *369*(1938), 957-975.

Talling, P. J., Allin, J., Armitage, D. A., Arnott, R. W., Cartigny, M. J., Clare, M. A., ... & Xu, J. (2015). Key Future Directions For Research On Turbidity Currents And Their Depositskey Future Directions For Research On Turbidity Currents And Their Deposits. *Journal of Sedimentary Research*, *85*(2), 153-169.

Talling, P. J., Baker, M. L., Pope, E. L., Ruffell, S. C., Jacinto, R. S., Heijnen, M. S., ... & Hilton, R. J. (2022). Longest sediment flows yet measured show how major rivers connect efficiently to deep sea. *Nature communications*, *13*(1), 4193.

Talling, P. J., Hage, S., Baker, M. L., Bianchi, T. S., Hilton, R. G., & Maier, K. L. (2023). The global turbidity current pump and its implications for organic carbon cycling. *Annual Review of Marine Science*, *16*.

Teles, V., Chauveau, B., Joseph, P., Weill, P., & Maktouf, F. (2016). CATS–A process-based model for turbulent turbidite systems at the reservoir scale. *Comptes Rendus Geoscience*, *348*(7), 489-498.

Van Rijn, L. C. (1984). Sediment transport, part I: bed load transport. *Journal of hydraulic engineering*, *110*(10), 1431-1456.

Voorn, M., Exner, U., & Rath, A. (2013). Multiscale Hessian fracture filtering for the enhancement and segmentation of narrow fractures in 3D image data. *Computers & geosciences*, *57*, 44-53.

Wahab, A., Hoyal, D. C., Shringarpure, M., & Straub, K. M. (2022). A dimensionless framework for predicting submarine fan morphology. *Nature Communications*, *13*(1), 7563.

Weimer, P., & Pettingill, H. S. (2007). Global overview of deep-water exploration and production.

Winterwerp, J. C. (1998). A simple model for turbulence induced flocculation of cohesive sediment. *Journal of hydraulic research*, *36*(3), 309-326.

Winterwerp, J. C., & Van Kesteren, W. G. (2004). *Introduction to the physics of cohesive sediment dynamics in the marine environment*. Elsevier.

Zhu, C., Zou, B., Zhao, R., Cui, J., Duan, X., Chen, Z., & Liang, Y. (2017). Retinal vessel segmentation in colour fundus images using extreme learning machine. *Computerized Medical Imaging and Graphics*, *55*, 68-77.

Zuiderveld, K. (1994). Contrast limited adaptive histogram equalization. *Graphics gems*, 474-485.

Figures

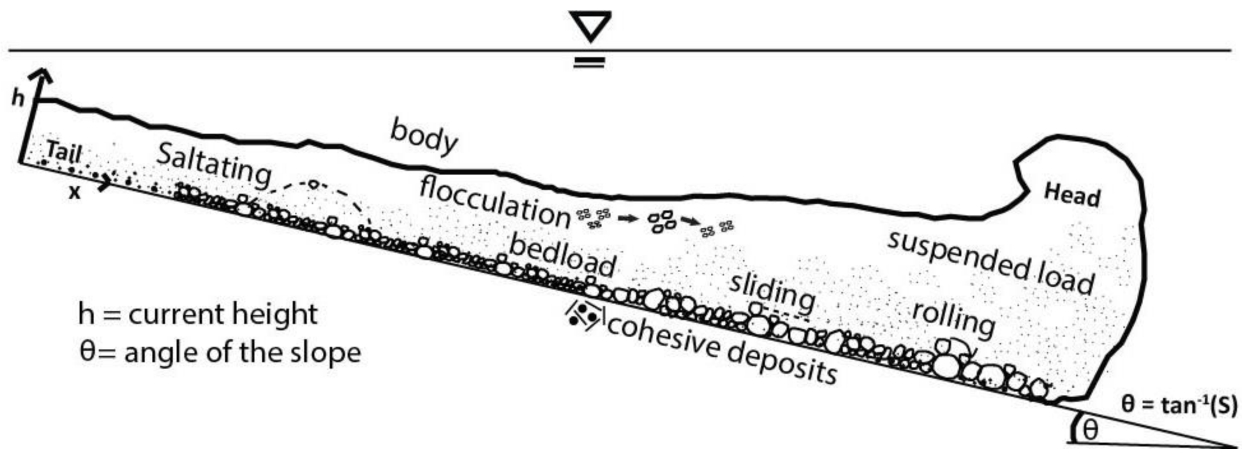

Figure 1: Schematic of bedload and suspended load transport in a turbidity current. In bedload transport, a grain of sediment can skip, saltate, slide, or roll over the active bed. Flocculation is a process where clay particles stick together to form larger particles 'floccules' that can eventually breakdown into smaller floccules. Once this sediment is deposited from suspension a deposit can stiffen through cohesive strengthening.

	Single grain	Poly grains (20)	Uniform distribution	Lognormal distribution	Erosion	Bedload	Cohesion	Flocculation	Runs
Gen 1	✓	X	X	X	✓	X	X	X	25
Gen 2	✓	X	X	X	✓	✓	X	X	25
Gen 3	X	✓	✓	X	✓	✓	X	X	25
Gen 4	X	✓	X	✓	✓	✓	X	X	25
Gen 5	X	✓	✓	X	✓	✓	✓	✓	25
Gen 6	X	✓	X	✓	✓	✓	✓	✓	25

Table 1: Numerical design for simulations investigated in this study. For more details on input conditions see supplementary Table 1.

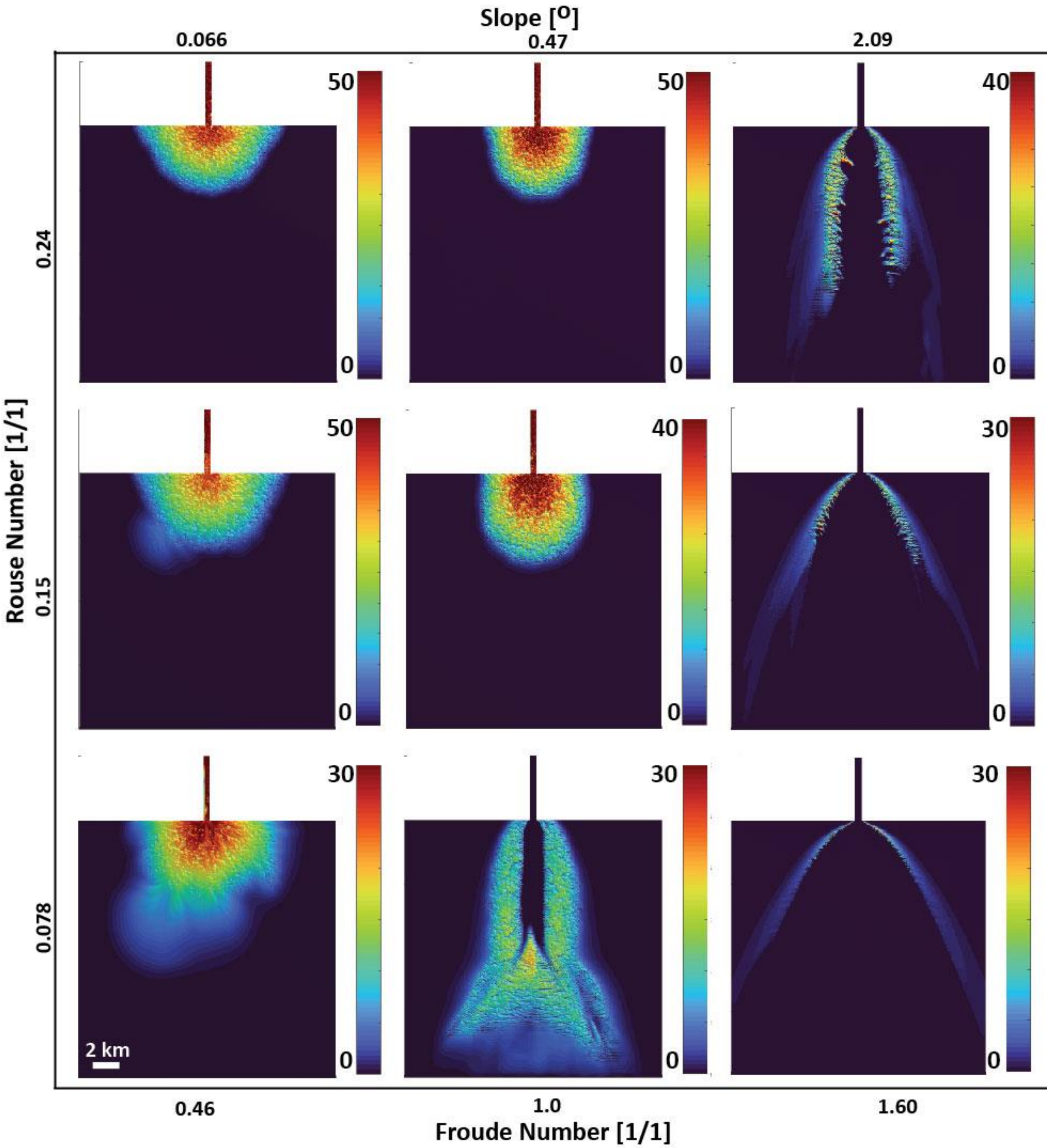

Figure 2. Sediment thickness at the end of generation 1 model runs. A subset of simulated and self-formed submarine fans forced by unique combinations of Fr_D and *p*. Colored bars represents deposit thickness in meters. Models have a domain size of 25 x 20 km. Additional variables are listed in supplementary Table 1.

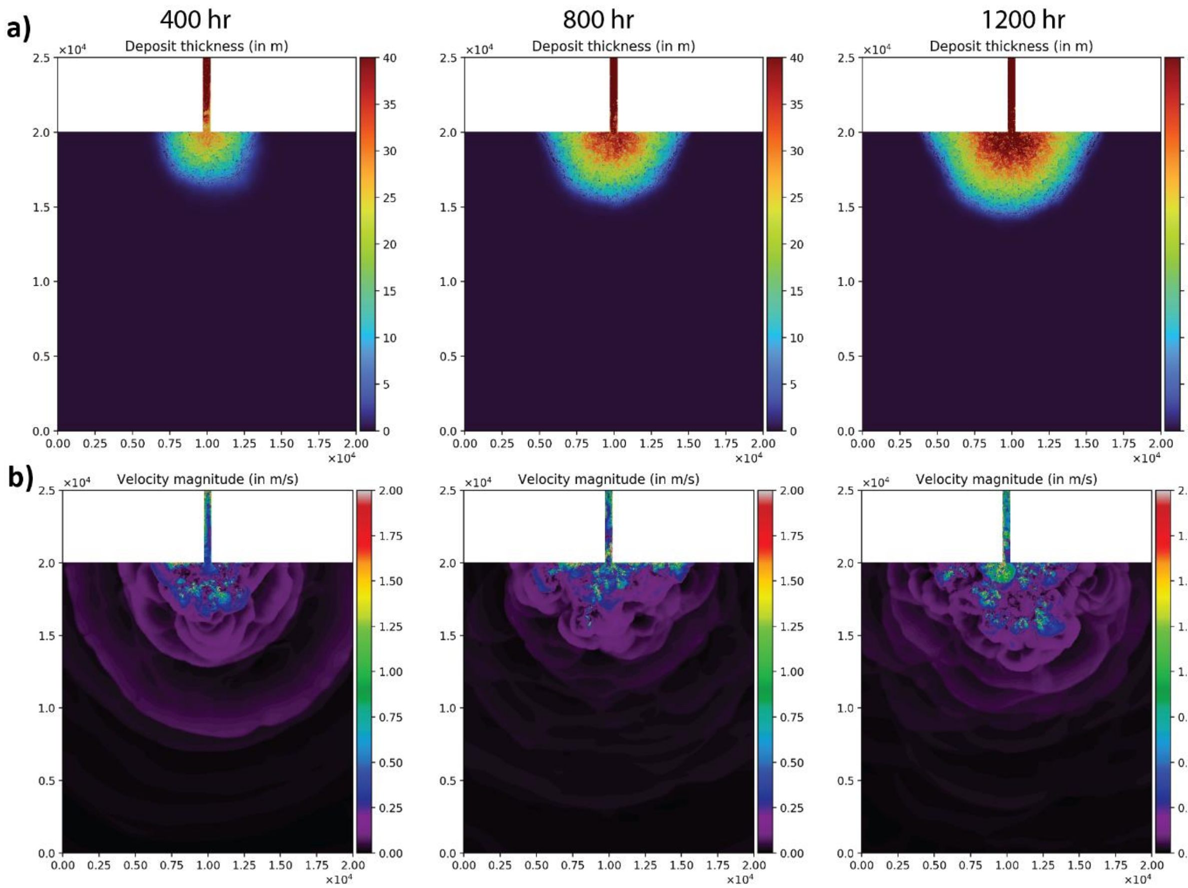

Figure 3. The channel maintenance in experiments that model erosion and deposition from suspension, but do not model bedload transport, flocculation, or bed cohesion. a, Maps of a single model from generation 1 show deposit thickness at various times into the simulation forced by Fr_D (0.46) and p (0.195). Note the lack of channel formation in the deposit thickness maps. b, Maps show velocity magnitude at the active surface at the same time as the maps above. Note that the velocity field indicates the absence of any channelized flow. Model dimensions are 25 x 20 km.

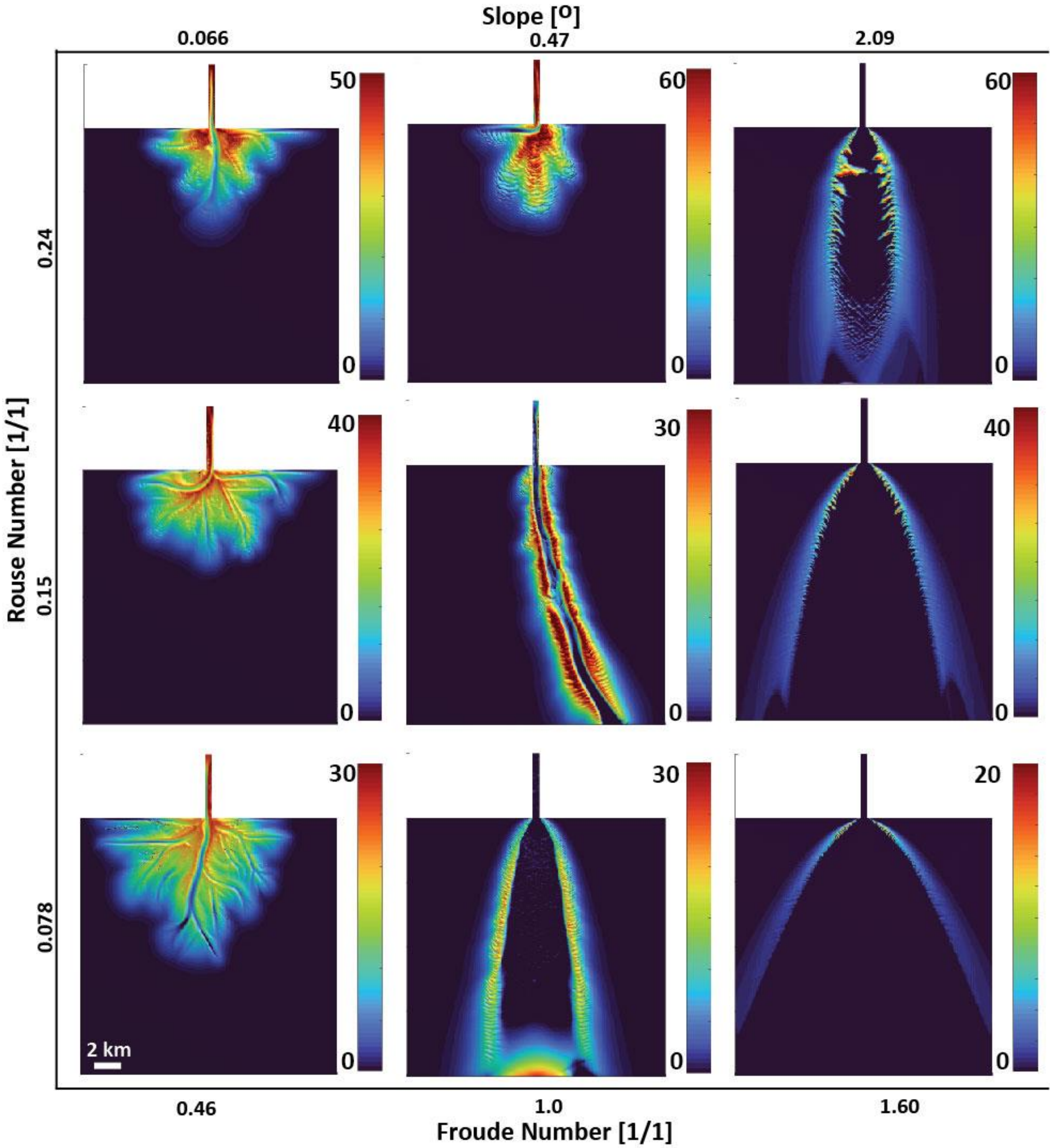

Figure 4. Sediment thickness at the end of generation 2 model runs. A subset of simulated and self-formed submarine fans forced by unique combinations of Fr_D and p. Colored bars represents deposit thickness in meters. Models have a domain size of 25 x 20 km. Additional variables are listed in supplementary Table 1.

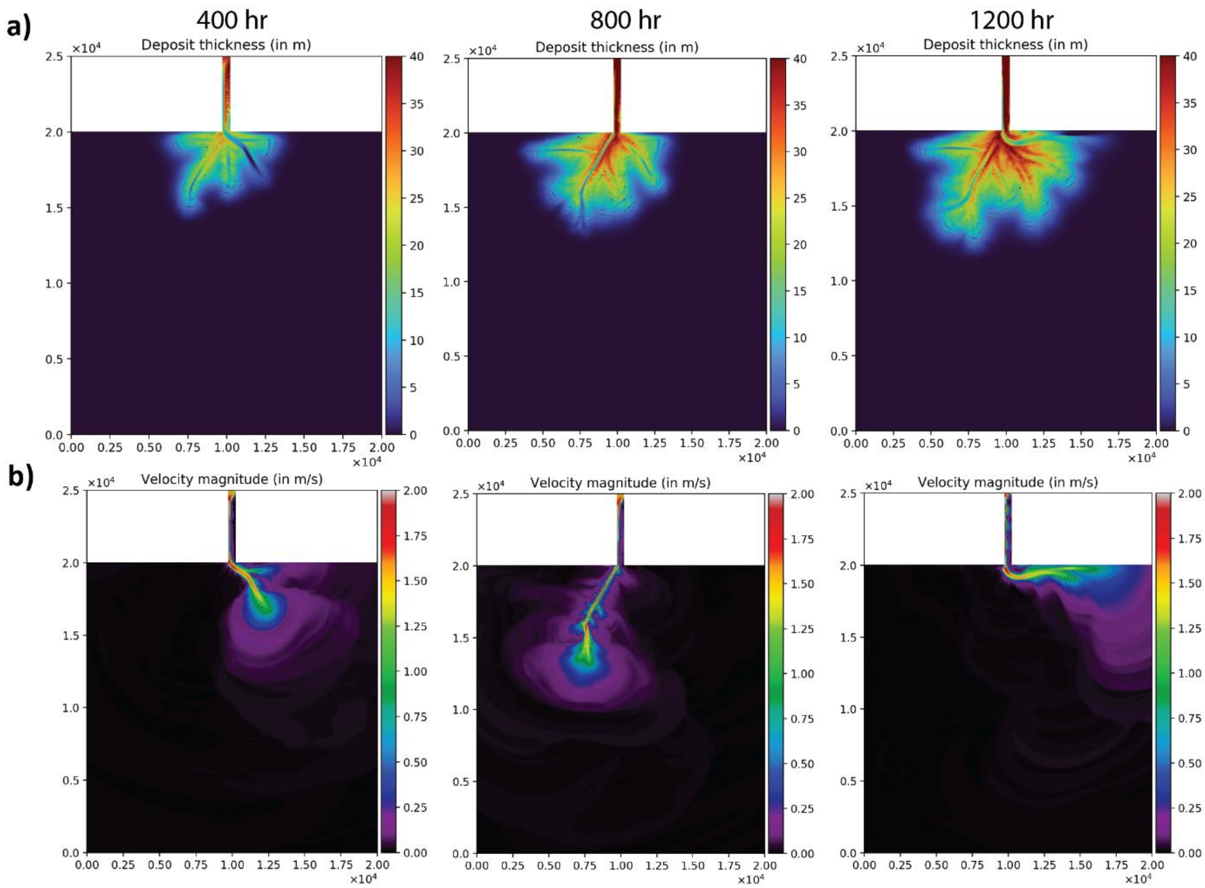

Figure 5. The impact of bedload transport on channel maintenance. a, Maps of a model from generation 2 show deposit thickness at various times into a simulation forced by Fr_D (0.46) and p (0.195). Note the development of a channel in the deposit thickness maps. This model is forced with similar boundary conditions as displayed in Fig. 3 except for the addition of bedload transport. b, Maps show velocity magnitude at the active surface at the same times as the maps above. Note that the velocity field indicates the presence of distributive channel flow. Model dimensions are 25 x 20 km.

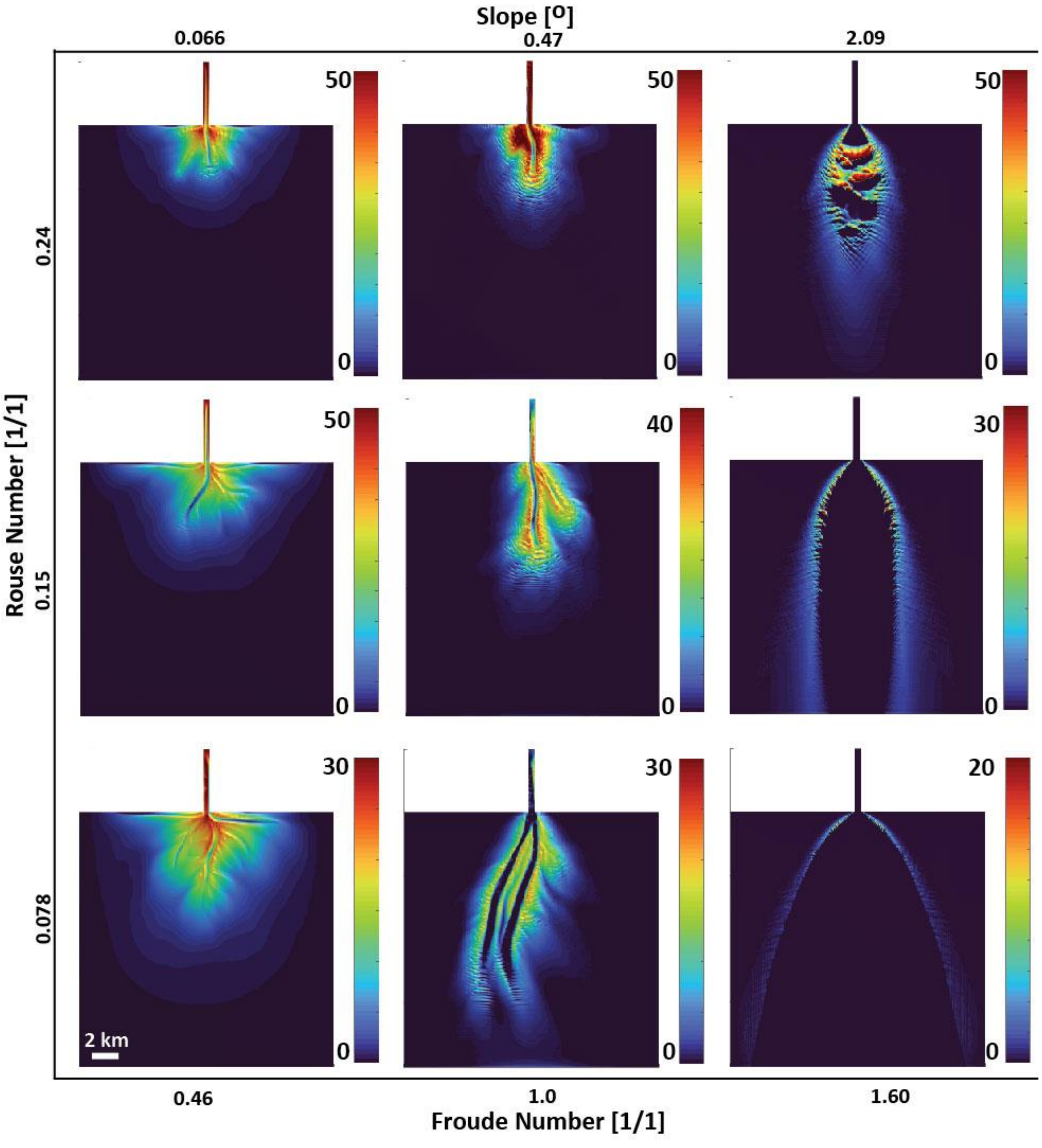

Figure 6. Sediment thickness at the end of generation 3 model runs. A subset of simulated and self-formed submarine fans forced by unique combinations of Fr_D and p. Colored bars represents deposit thickness in meters. Models have a domain size of 25 x 20 km. Additional variables are listed in supplementary Table 1.

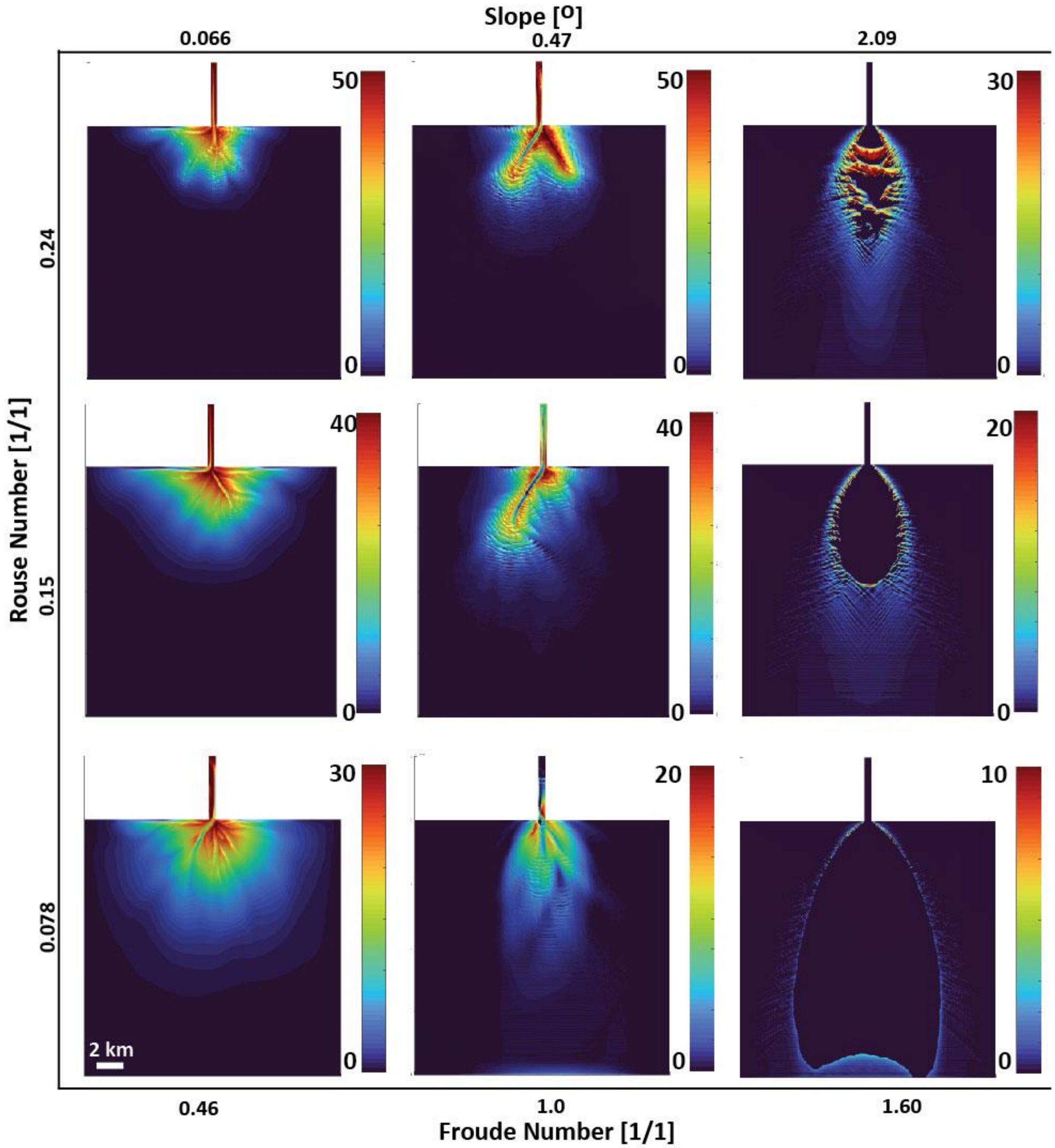

Figure 7. Sediment thickness at the end of generation 4 model runs. A subset of simulated and self-formed submarine fans forced by unique combinations of Fr_D and p. Colored bars represents deposit thickness in meters. Models have a domain size of 25 x 20 km. Additional variables are listed in supplementary Table 1.

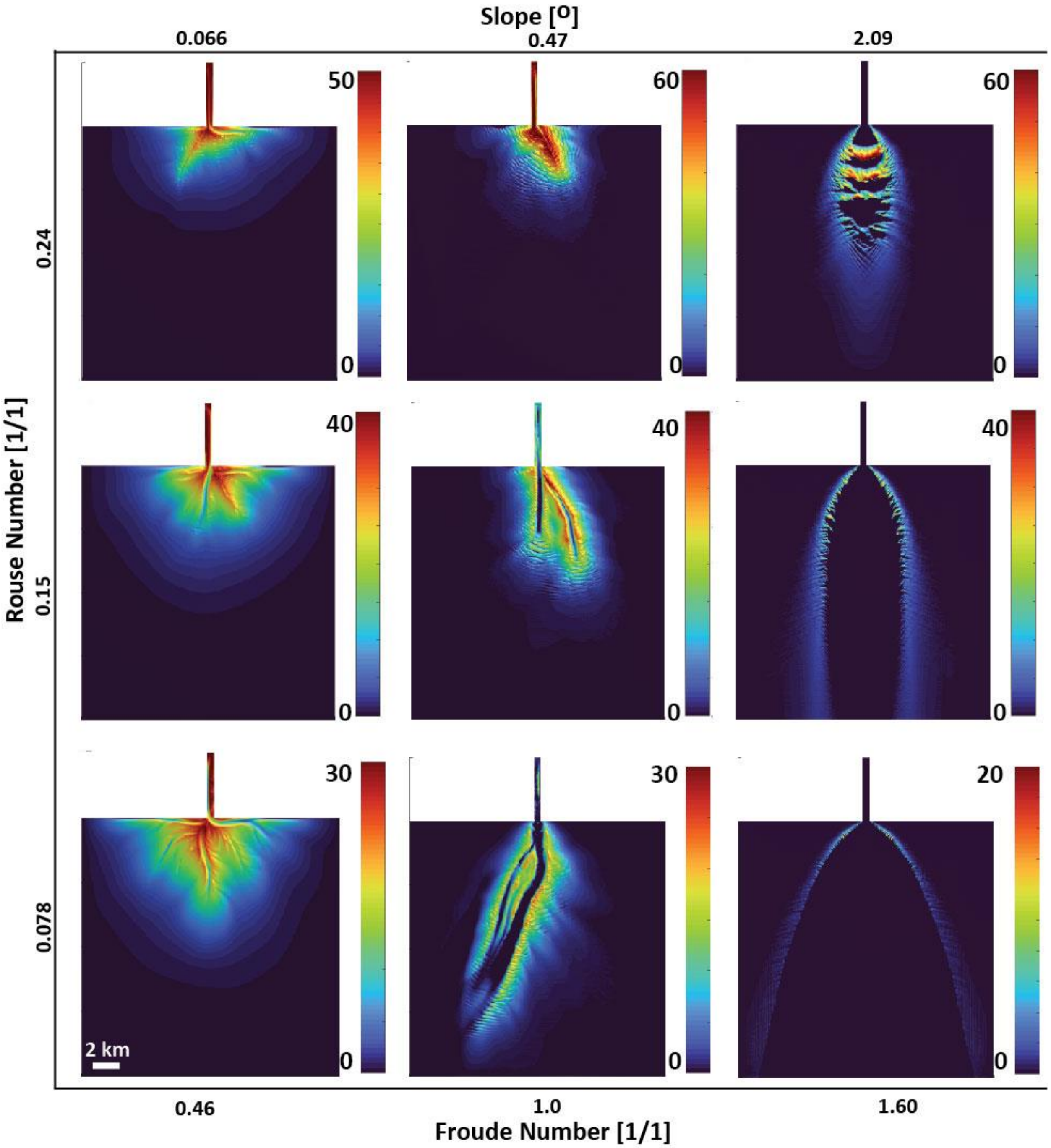

Figure 8. Sediment thickness at the end of generation 5 model runs. A subset of simulated and self-formed submarine fans forced by unique combinations of Fr_D and *p*. Colored bars represents deposit thickness in meters. Models have a domain size of 25 x 20 km. Additional variables are listed in supplementary Table 1.

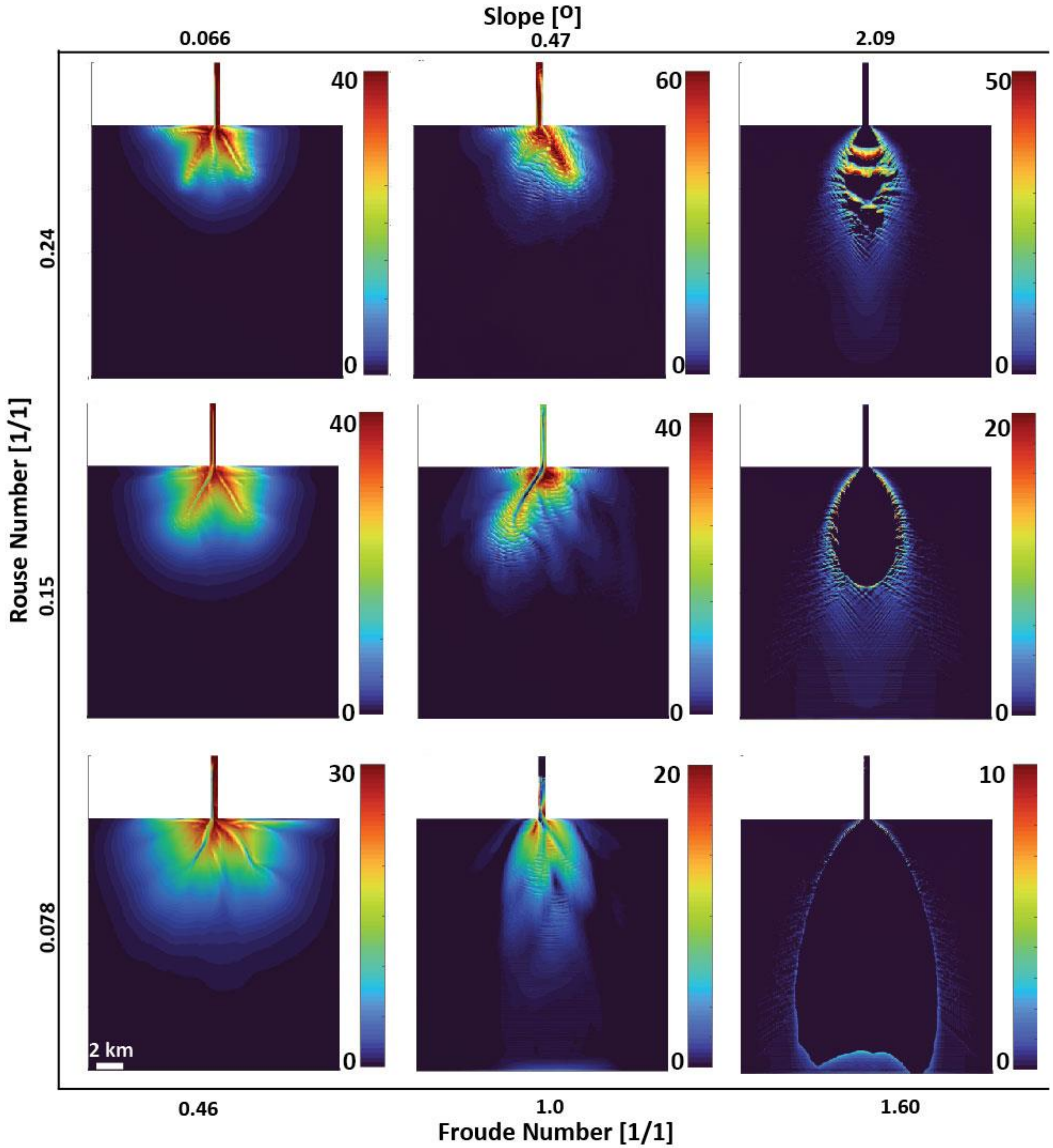

Figure 9. Sediment thickness at the end of generation 6 model runs. A subset of simulated and self-formed submarine fans forced by unique combinations of Fr_D and *p*. Colored bars represents deposit thickness in meters. Models have a domain size of 25 x 20 km. Additional variables are listed in supplementary Table 1.

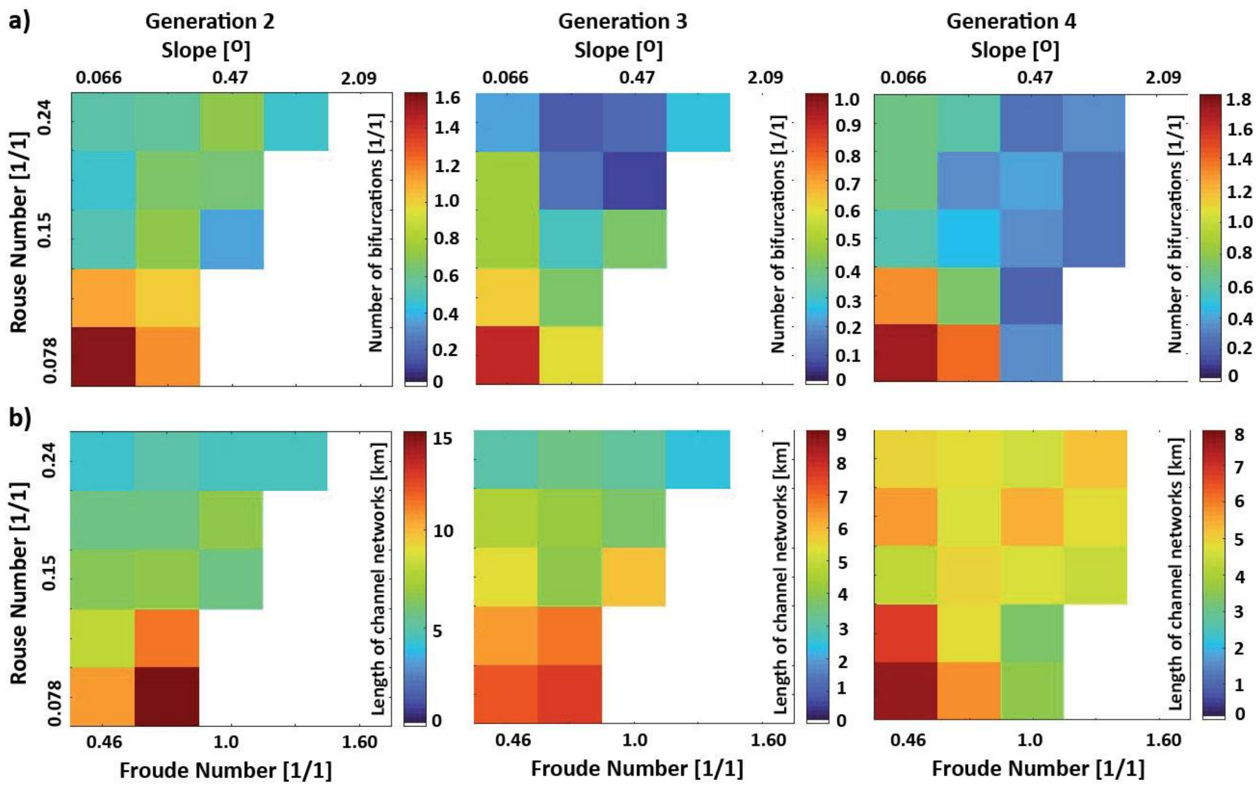

Figure 10. Number of channel bifurcations and length of channelization across models from generations 2, 3, and 4. a, Matrix shows average number of bifurcations over the course of model runs, where bifurcations are counted every 40 hours into the simulation. b, Matrix shows the average length of channels present on an active surface over the course of the model runs, where total length of channelization is measured every 40 hours into the simulation. White regions represent models in which input sediment largely bypassed model domains and thus channelize was not sufficient to craft a dynamic fan surface.

Supplementary Materials

Case	Fr_D	p	Slope (deg)	u [m/s]	d50 [um]	sorting	Ws [m/s]	Duration [sec]	u* [m/s]	d98 [um]
1	0.46	0.078	0.066	0.93	65	1.2	0.005	5403382	0.059	465
2	0.73	0.078	0.200	1.47	74	1.5	0.007	3404871	0.093	796
3	1	0.078	0.470	2.01	77	1.7	0.010	2485556	0.127	1247
4	1.36	0.078	1.209	2.74	74	2.1	0.013	1827615	0.173	2124
5	1.6	0.078	2.092	3.22	69	2.3	0.016	1553472	0.204	2972
6	0.46	0.1	0.066	0.93	82	1.1	0.006	5403382	0.059	465
7	0.73	0.1	0.200	1.47	97	1.3	0.009	3404871	0.093	796
8	1	0.1	0.470	2.01	104	1.5	0.013	2485556	0.127	1247
9	1.36	0.1	1.209	2.74	105	1.9	0.017	1827615	0.173	2124
10	1.6	0.1	2.092	3.22	101	2.1	0.020	1553472	0.204	2972
11	0.46	0.15	0.066	0.93	117	0.8	0.009	5403382	0.059	465
12	0.73	0.15	0.200	1.47	145	1.1	0.014	3404871	0.093	796
13	1	0.15	0.470	2.01	164	1.3	0.019	2485556	0.127	1247
14	1.36	0.15	1.209	2.74	177	1.5	0.026	1827615	0.173	2124
15	1.6	0.15	2.092	3.22	179	1.7	0.031	1553472	0.204	2972
16	0.46	0.195	0.066	0.93	146	0.7	0.011	5403382	0.059	465
17	0.73	0.195	0.200	1.47	186	0.9	0.018	3404871	0.093	796
18	1	0.195	0.470	2.01	216	1.1	0.025	2485556	0.127	1247
19	1.36	0.195	1.209	2.74	242	1.3	0.034	1827615	0.173	2124
20	1.6	0.195	2.092	3.22	252	1.5	0.040	1553472	0.204	2972
21	0.46	0.24	0.066	0.93	173	0.6	0.014	5403382	0.059	465
22	0.73	0.24	0.200	1.47	225	0.8	0.022	3404871	0.093	796
23	1	0.24	0.470	2.01	266	1.0	0.031	2485556	0.127	1247
24	1.36	0.24	1.209	2.74	307	1.2	0.042	1827615	0.173	2124
25	1.6	0.24	2.092	3.22	326	1.4	0.049	1553472	0.204	2972

Supplementary Table 1. Select common variables used in this study. Fr_D **=** Densimetric Froude Number; p = Rouse Number; u = Mean velocity at the inlet; d50 = Mean sand diameter; Ws = Mean settling velocity of suspended material at the inlet; Duration = Total simulation time on a supercomputer; u* = Mean shear velocity at the inlet; d98 = Maximum sand diameter

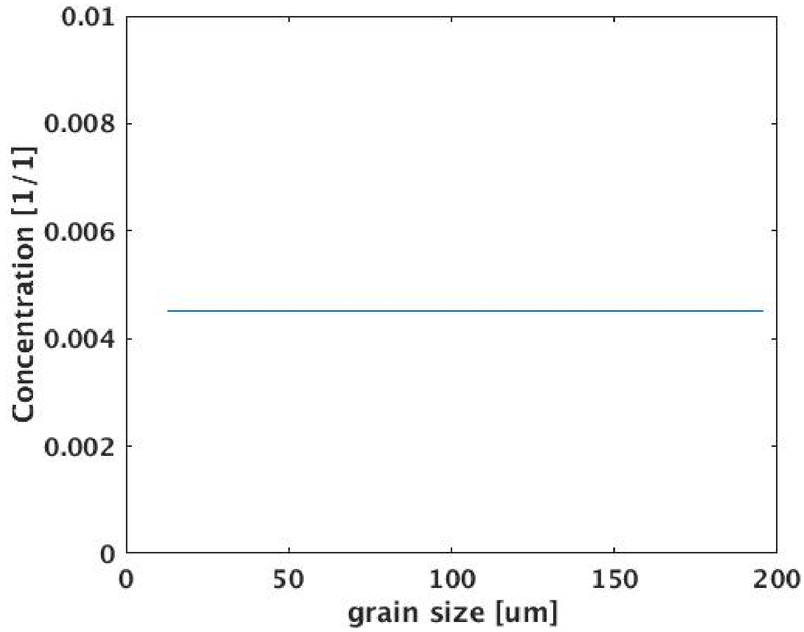

Supplementary Figure 1: An example of a uniform grain size distribution.

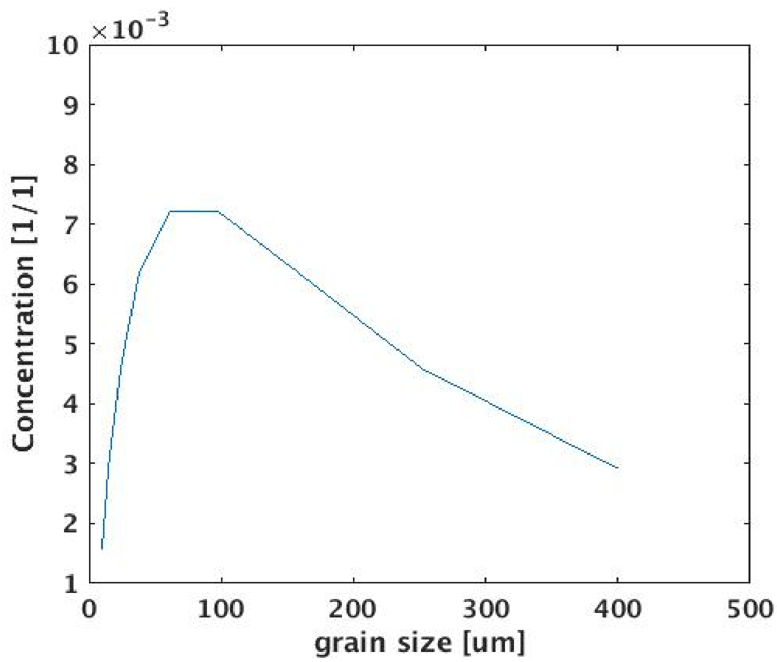

Supplementary Figure 2: An example of a log-normal grain size distribution.

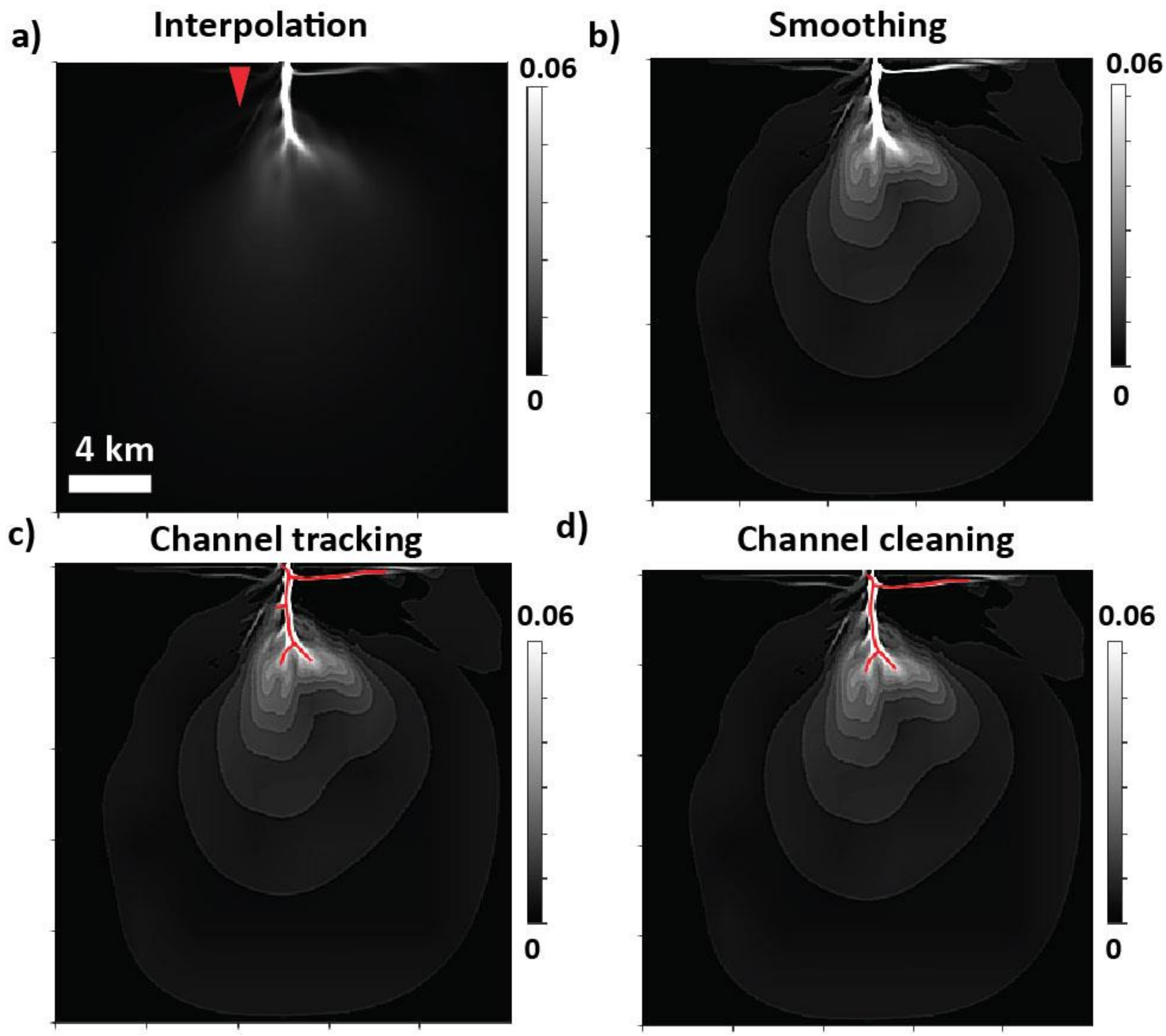

Supplementary Figure 3. Example of channel tracking in a simulation. a, Sediment load (height*concentration) data is interpolated from a triangular irregular network (TIN) to a Cartesian grid. This model is from generation 3 and is forced with a Fr_D (0.46) and p (0.1). Red arrow shows primary flow direction. b, A Gabor filter is applied to smooth and enhance the sharpness of the data. This step helps in determining channel edges due to the sharp contrast with the non-channelized background (see methods). c, The channels are tracked using the peak of the fitted distribution every 40 hours into the simulation. d, Small channel branches that are tracked because of partial flow stripping from the main channel network are removed.

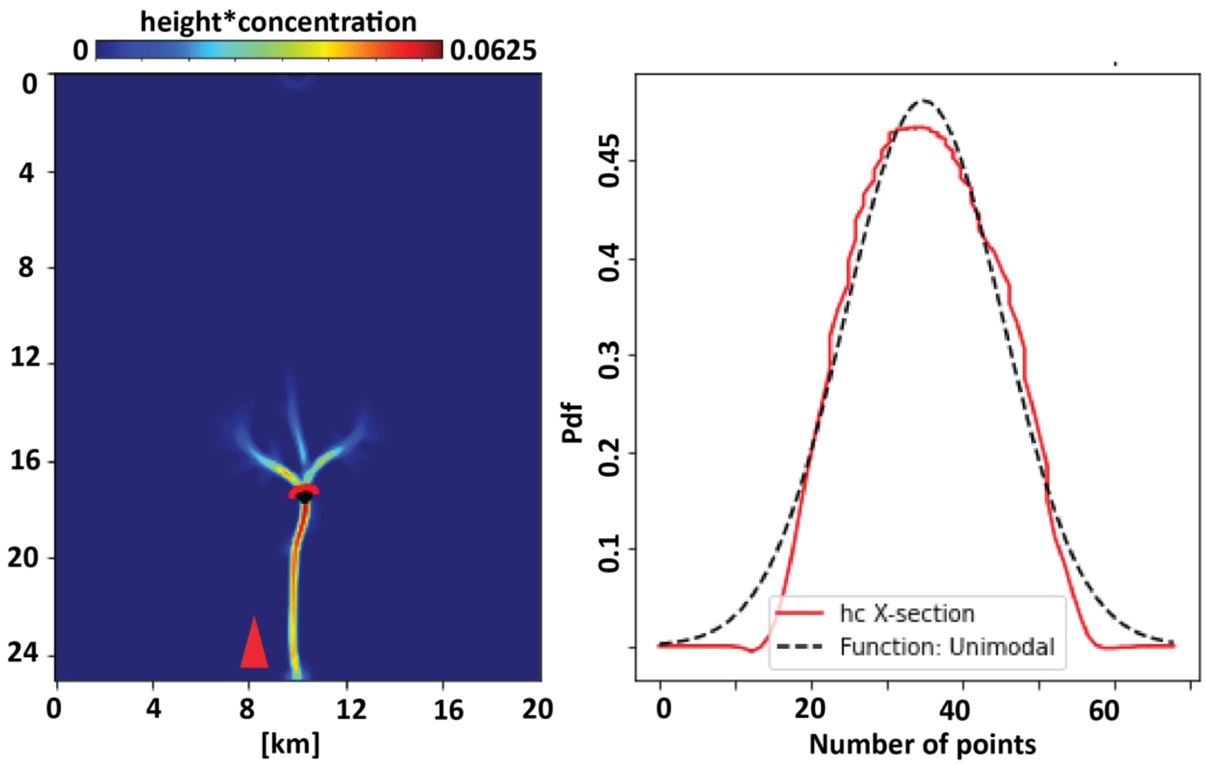

Supplementary Figure 4. Fitting a unimodal distribution using the sediment load property. In this example the tracking workflow approximates the sediment load data through a unimodal distribution based on the closeness of the fit. Left plot: Image displays the interpolated sediment load property. Red arrow indicates the primary direction of the flow. Color bar represents sediment load value. Red curve outlines the cross-section where a channel is being tracked. Right plot: Plot of the probability density function (red) of the sediment load from the cross-section in the left image. The dotted black line is unimodal distribution fit to the data.

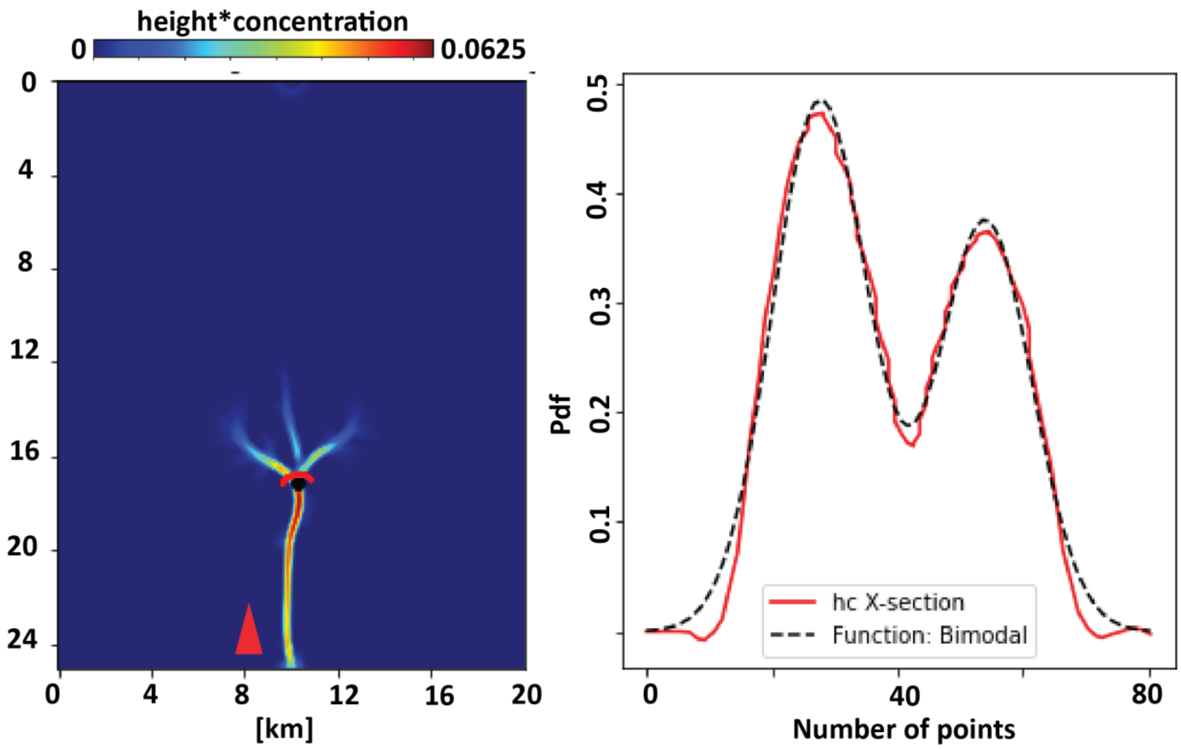

Supplementary Figure 5. Fitting a bimodal distribution using the sediment load property. In this example, the tracking workflow approximates the sediment load data through a Bimodal Gaussian distribution based on a low overlap coefficient (0.09). Left panel: Image of the interpolated sediment load property. Red arrow indicates the primary flow direction. Color bar represents sediment load value. Red curve outlines the cross-section where a channel is being tracked. Right panel: Plot of the probability density function (red) of the sediment load from the cross-section in the left panel. The dotted black line is a bimodal distribution fit to the data. The closeness of the fit and the low overlap value suggest that the two distributions are sufficiently different from one another. The workflow picks the peak of each distribution to track channel branches (see methods for more details).

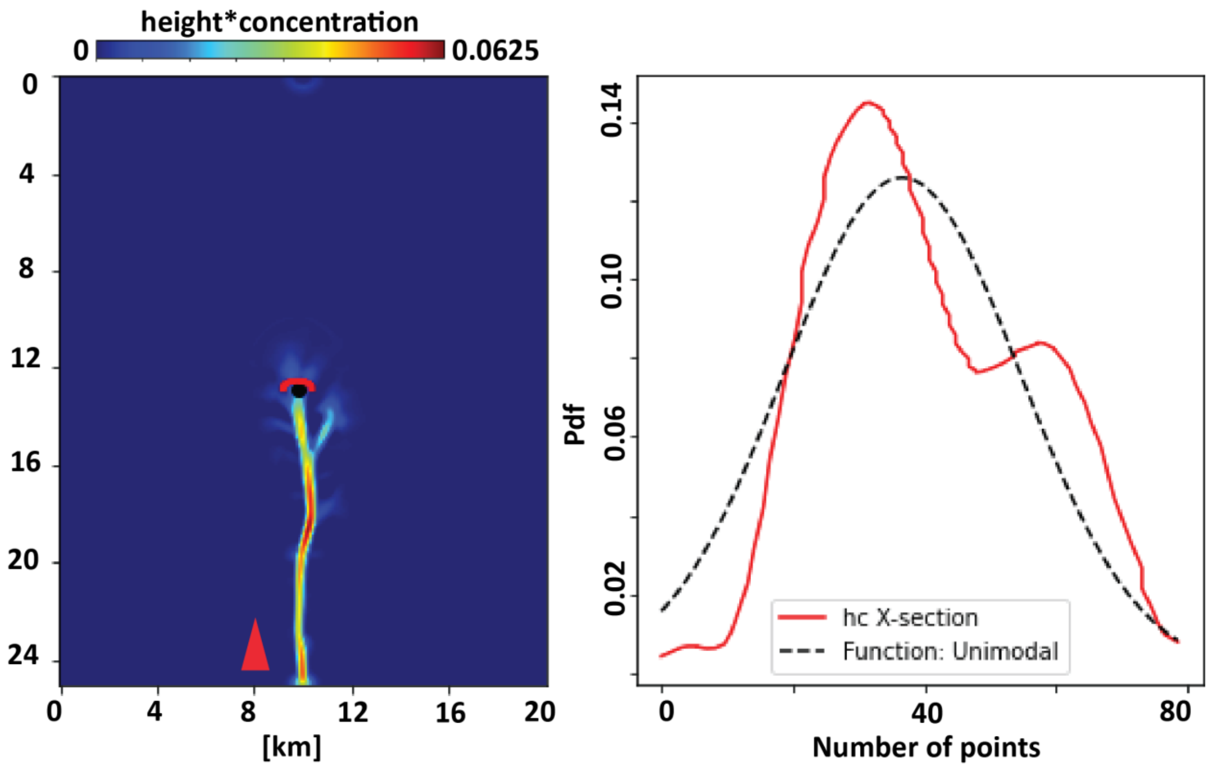

Supplementary Figure 6. Determining a distribution fit. In this example the tracking workflow approximates the sediment load data through a Unimodal Gaussian distribution based on high overlap coefficient (0.25). Left plot: Image is plotting an instance of the interpolated sediment load property. Red arrow points to the primary direction of the flow. Color bar represents sediment load value. Red curve outlines the cross-section where channel is being tracked. Right plot: Plot of the probability density function (red) of the sediment load from the cross-section in the left image. The dotted black line is unimodal distribution fit to the data. The fit suggest that the two distributions are not sufficiently different from one another.

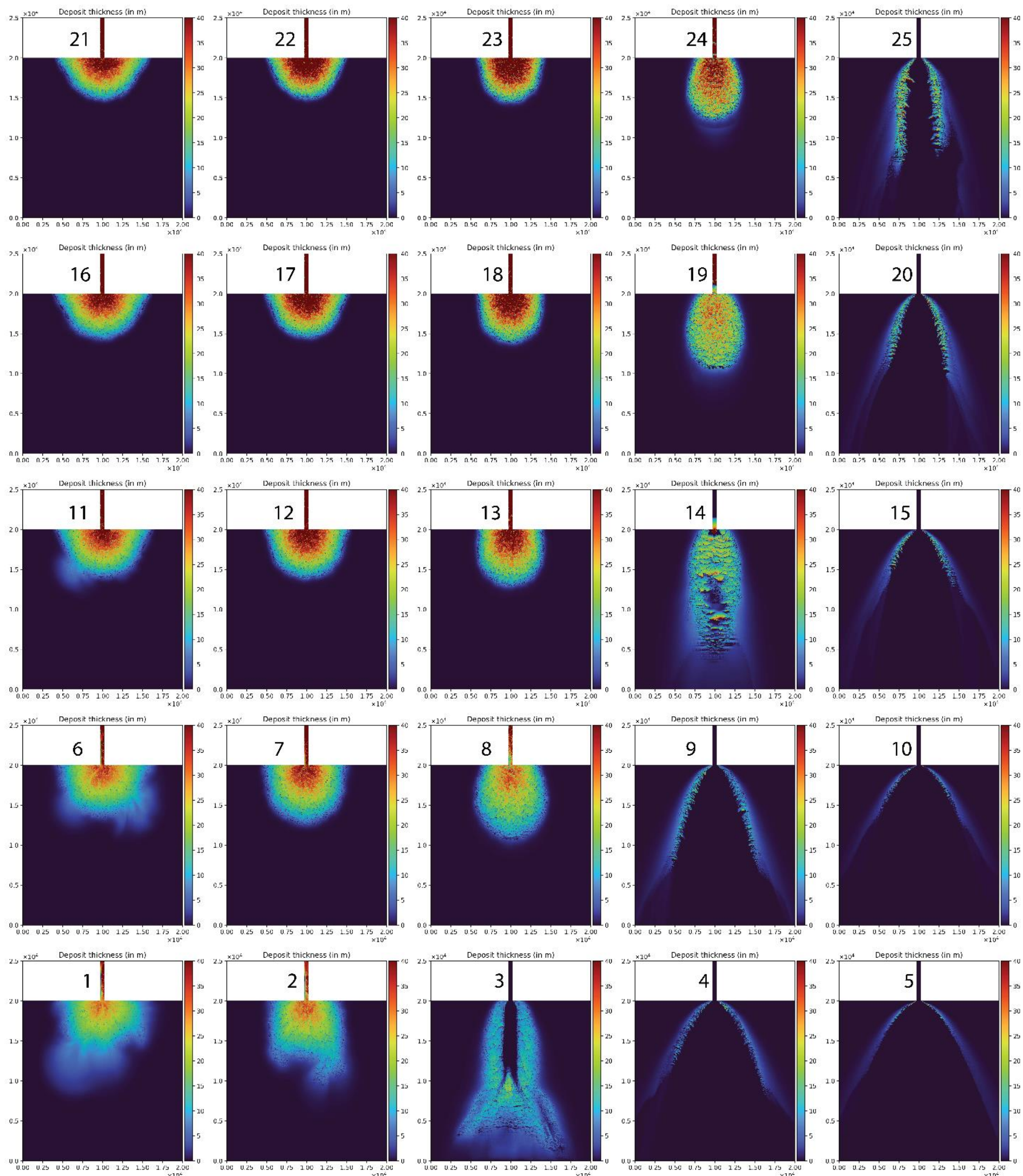

Supplementary Figure 7. Generation 1 deposit thickness maps at the end of each numerical experiment. Column represents increasing Fr_D from left to right and rows represents p increasing from bottom to top. Color bar is for deposit thickness in m. See Supplementary Table 1 for more details.

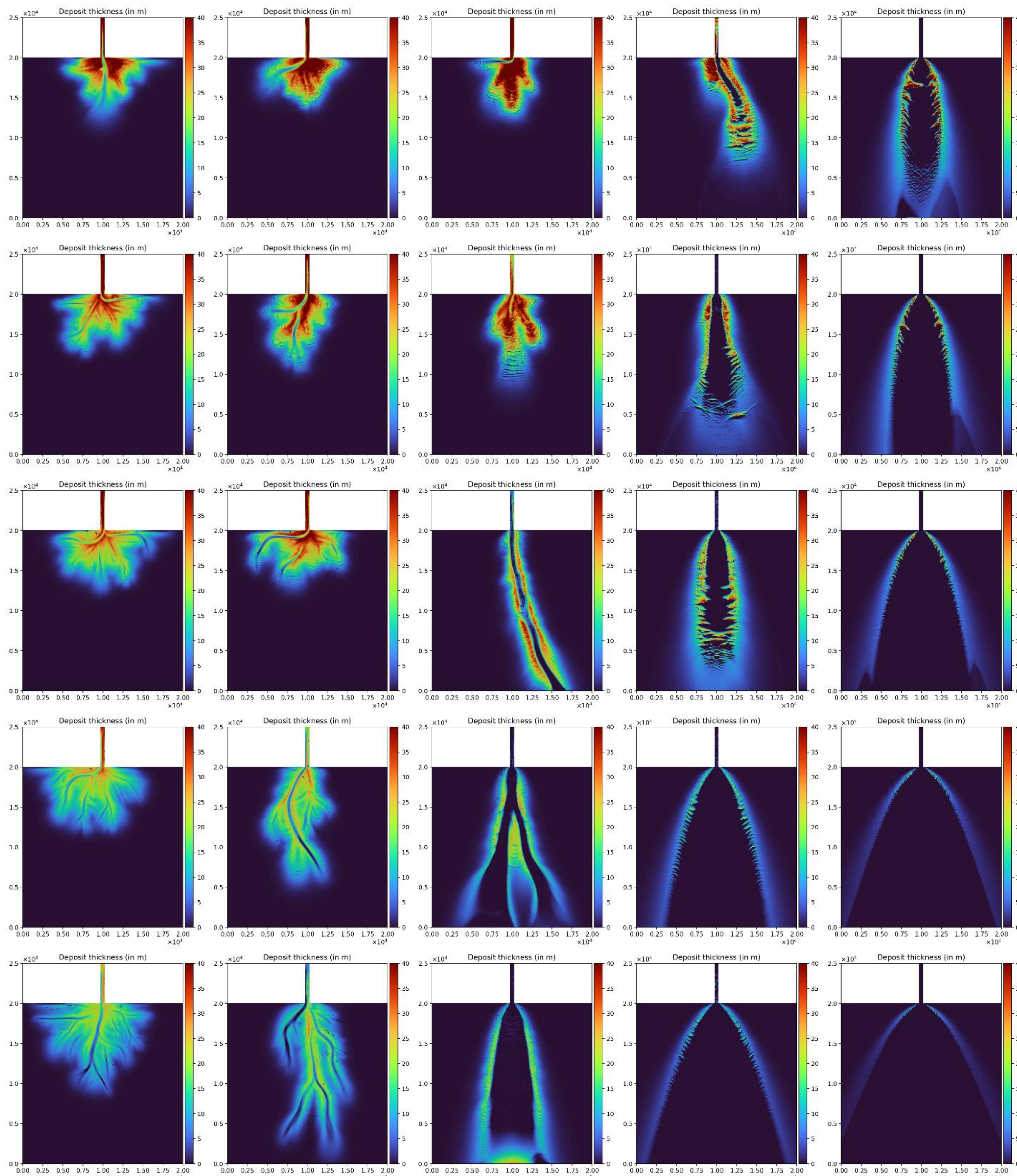

Supplementary Figure 8. Generation 2 deposit thickness maps of all models runs at the end of the simulation. Column represents increasing Fr_D from left to right and rows represents p increasing from bottom to top. Color bar is for deposit thickness in m. Similar case numbers as Supplementary Figure 7 and see Supplementary Table 1 for more details.

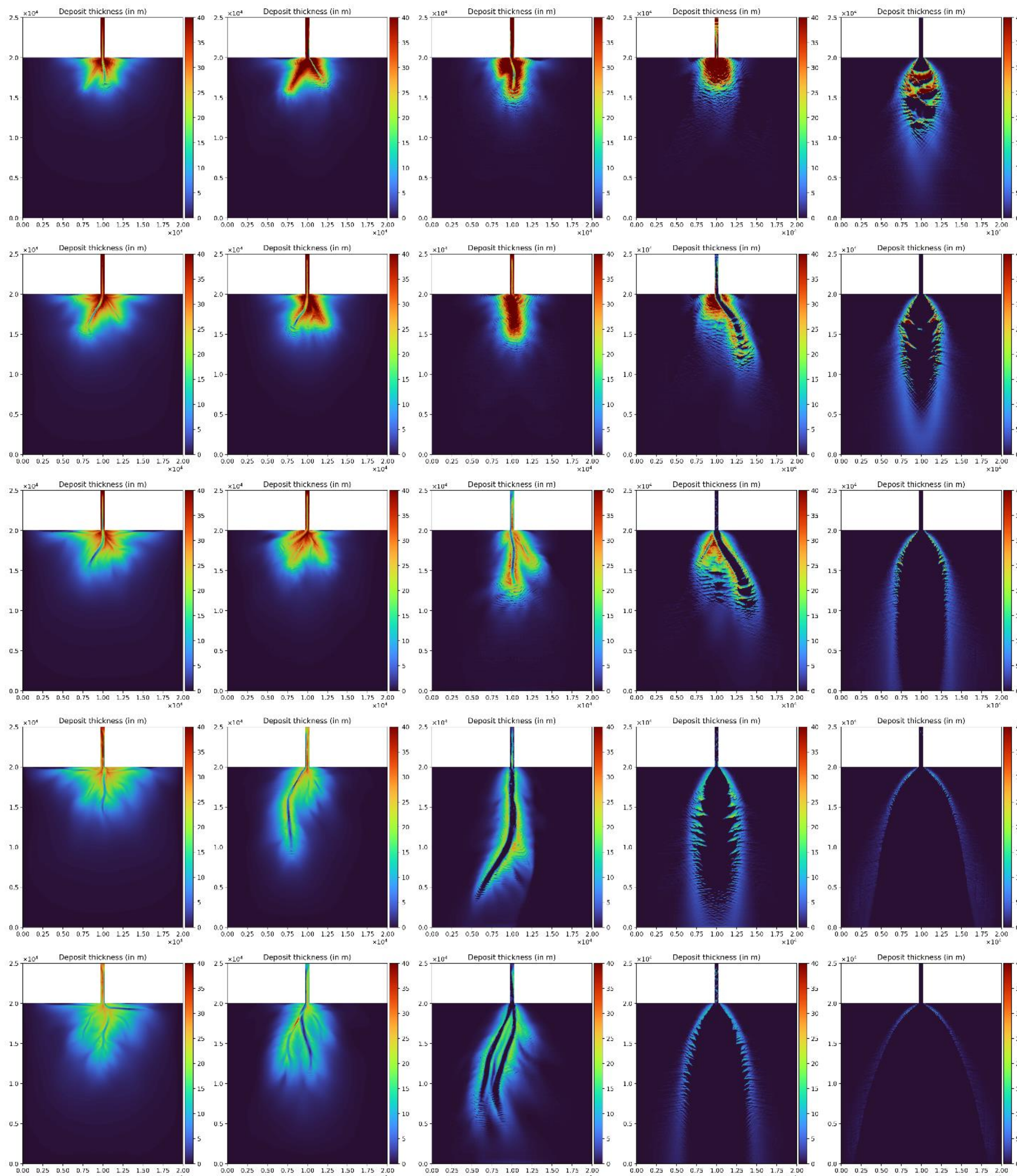

Supplementary Figure 9. Generation 3 deposit thickness maps of all models runs at the end of the simulation. Column represents increasing Fr_D from left to right and rows represents p increasing from bottom to top. Color bar is for deposit thickness in m. Similar case numbers as Supplementary Figure 7 and see Supplementary Table 1 for more details.

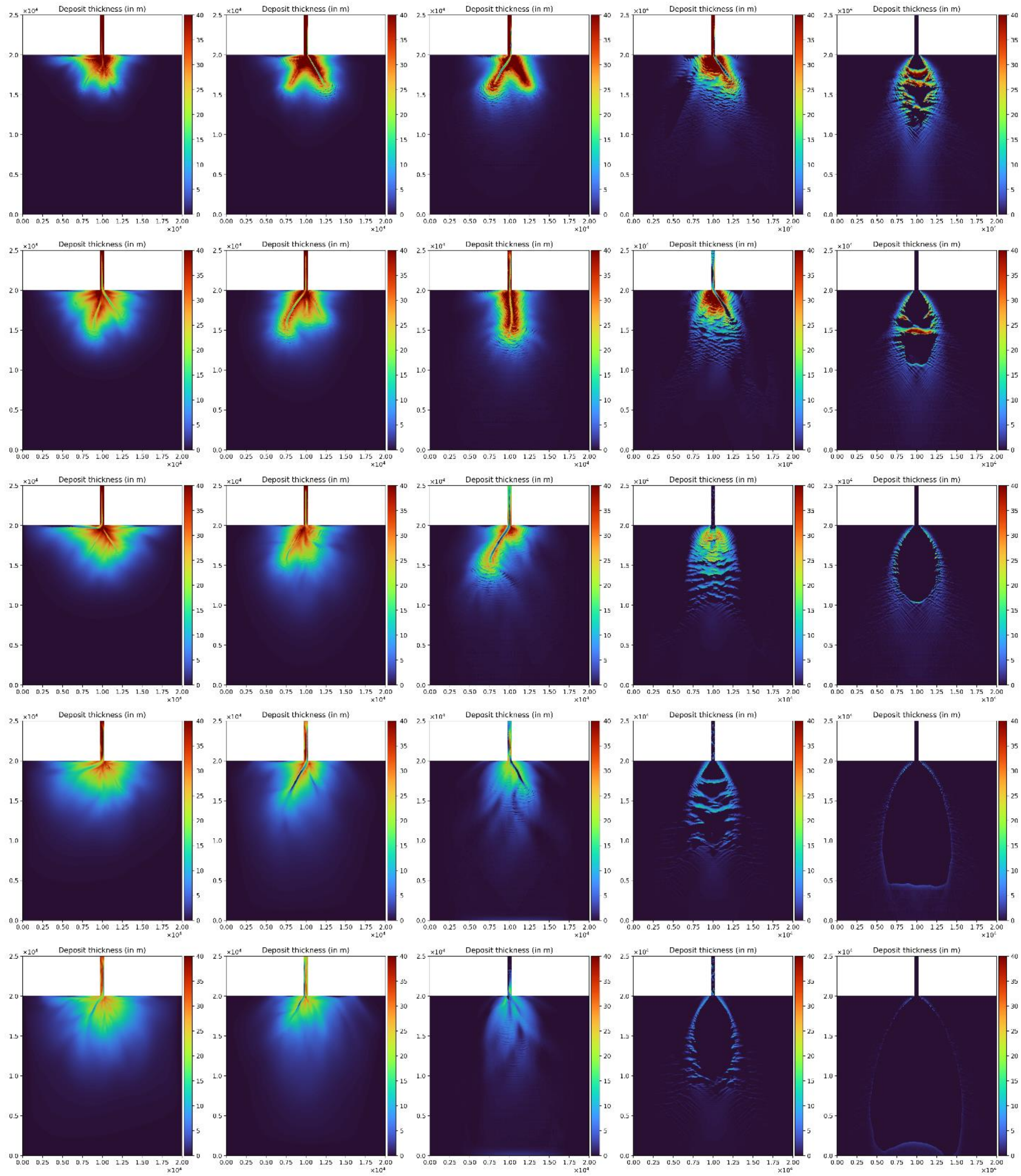

Supplementary Figure 10. Generation 4 deposit thickness maps of all models runs at the end of the simulation. Column represents increasing Fr_D from left to right and rows represents p increasing from bottom to top. Color bar is for deposit thickness in m. Similar case numbers as Supplementary Figure 7 and see Supplementary Table 1 for more details.

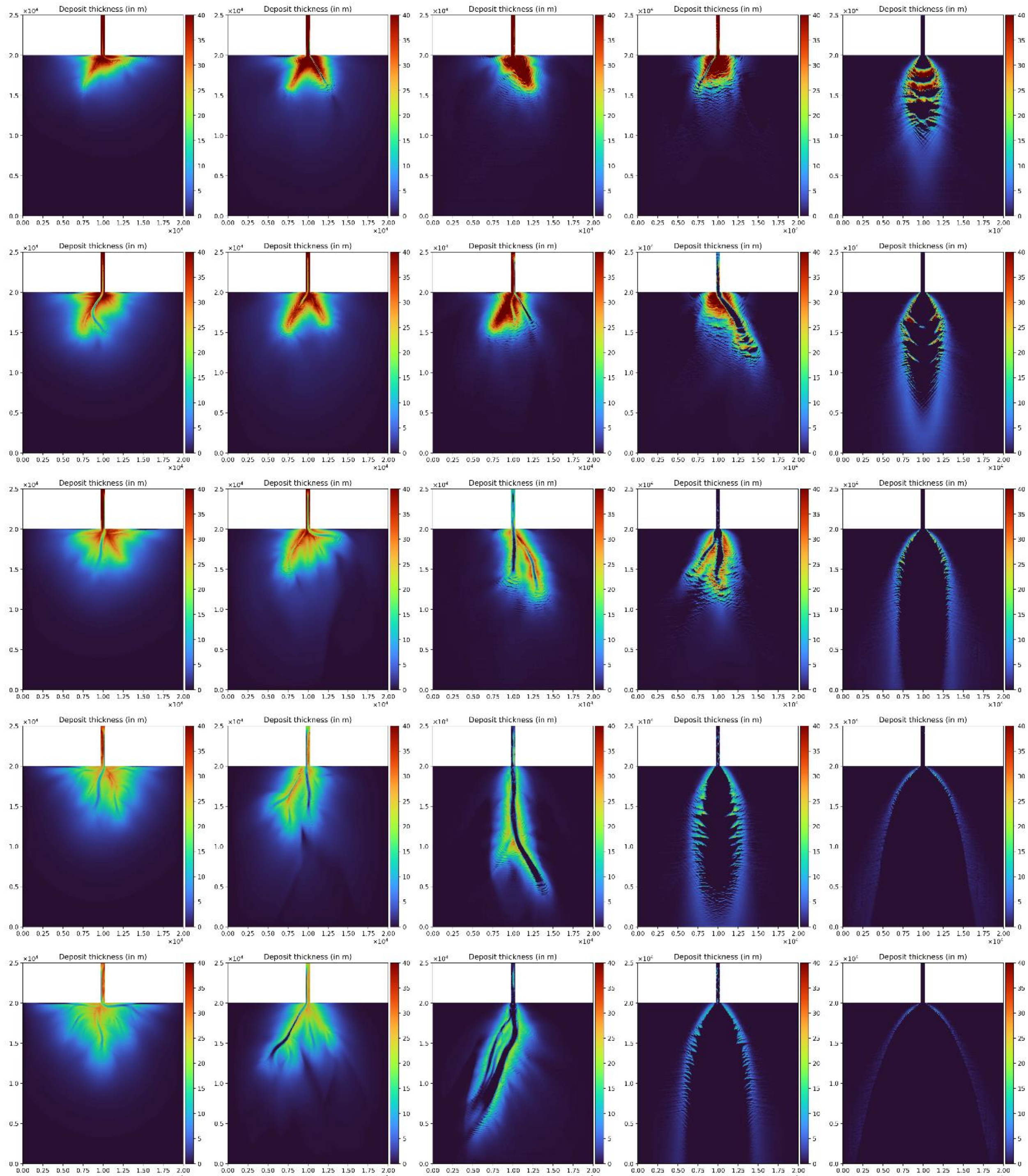

Supplementary Figure 11. Generation 5 deposit thickness maps of all models runs at the end of the simulation. Column represents increasing Fr_D from left to right and rows represents p increasing from bottom to top. Color bar is for deposit thickness in m. Similar case numbers as Supplementary Figure 7 and see Supplementary Table 1 for more details.

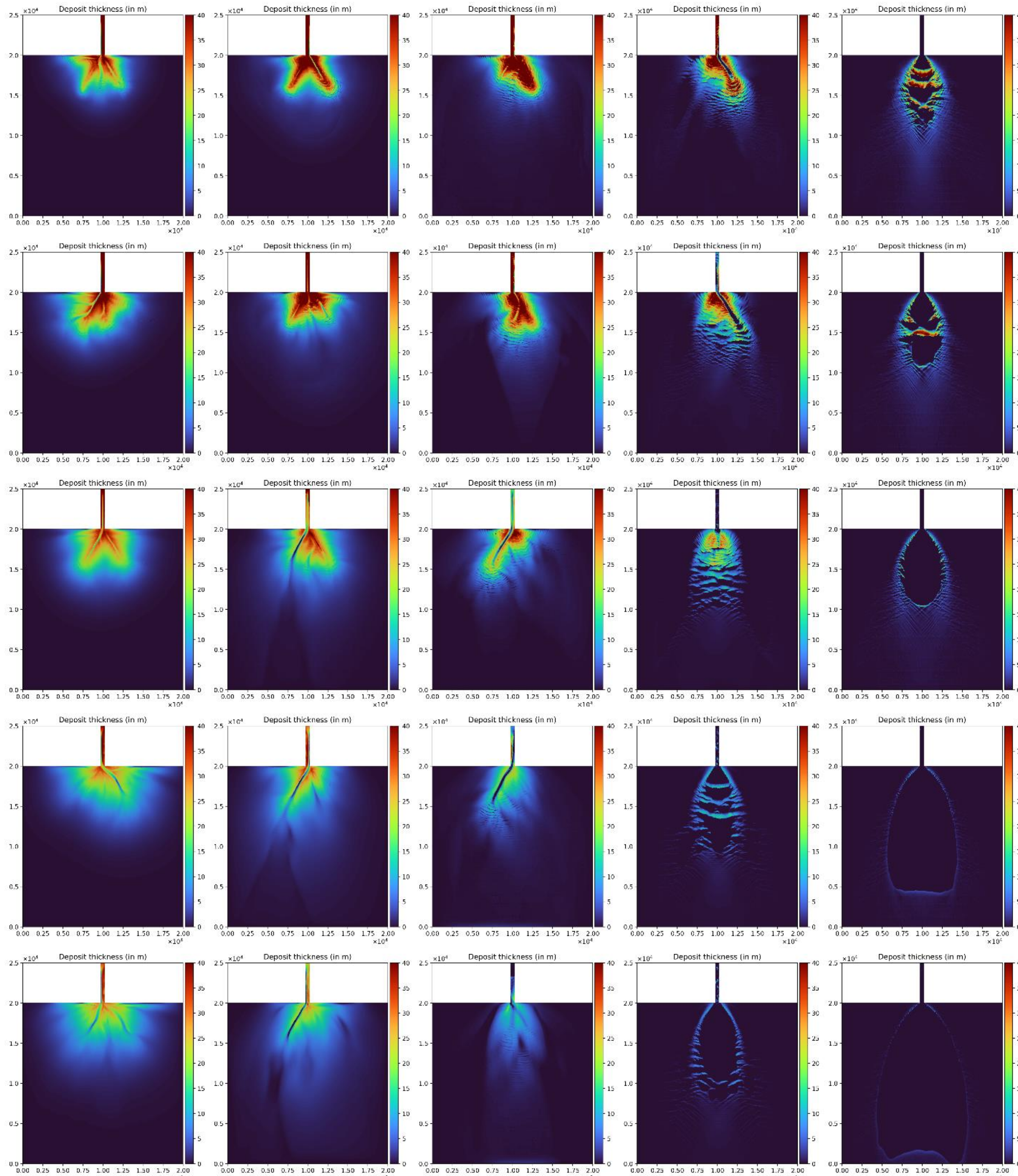

Supplementary Figure 12. Generation 6 deposit thickness maps of all models runs at the end of the simulation. Column represents increasing Fr_D from left to right and rows represents p increasing from bottom to top. Color bar is for deposit thickness in m. Similar case numbers as Supplementary Figure 7 and see Supplementary Table 1 for more details.